

**IntechOpen**

# Magnesium

The Wonder Element for Engineering/  
Biomedical Applications

*Edited by Manoj Gupta*





---

# Magnesium - The Wonder Element for Engineering/ Biomedical Applications

*Edited by Manoj Gupta*

Published in London, United Kingdom

---



## IntechOpen





*Supporting open minds since 2005*



Magnesium - The Wonder Element for Engineering/Biomedical Applications

<http://dx.doi.org/10.5772/intechopen.73398>

Edited by Manoj Gupta

#### Contributors

Jafar Albinmousa, Kavian Omar Cooke, Abdulaziz Alhazaa, Anas Attieh, Ryota Kondo, Takeshita T. Hiroyuki, Niranjan C A, Srinivas Satyanarayana, Ramachandra Madhavarao, Srinivasan Murugan, Nguyen Quy Bau, Manoj Gupta, Ramesh Kumar Subramanian, Arun Kumar Srirangan, Sreearavind M, Sravya Tekumalla

© The Editor(s) and the Author(s) 2020

The rights of the editor(s) and the author(s) have been asserted in accordance with the Copyright, Designs and Patents Act 1988. All rights to the book as a whole are reserved by INTECHOPEN LIMITED. The book as a whole (compilation) cannot be reproduced, distributed or used for commercial or non-commercial purposes without INTECHOPEN LIMITED's written permission. Enquiries concerning the use of the book should be directed to INTECHOPEN LIMITED rights and permissions department ([permissions@intechopen.com](mailto:permissions@intechopen.com)).

Violations are liable to prosecution under the governing Copyright Law.



Individual chapters of this publication are distributed under the terms of the Creative Commons Attribution 3.0 Unported License which permits commercial use, distribution and reproduction of the individual chapters, provided the original author(s) and source publication are appropriately acknowledged. If so indicated, certain images may not be included under the Creative Commons license. In such cases users will need to obtain permission from the license holder to reproduce the material. More details and guidelines concerning content reuse and adaptation can be found at <http://www.intechopen.com/copyright-policy.html>.

#### Notice

Statements and opinions expressed in the chapters are these of the individual contributors and not necessarily those of the editors or publisher. No responsibility is accepted for the accuracy of information contained in the published chapters. The publisher assumes no responsibility for any damage or injury to persons or property arising out of the use of any materials, instructions, methods or ideas contained in the book.

First published in London, United Kingdom, 2020 by IntechOpen

IntechOpen is the global imprint of INTECHOPEN LIMITED, registered in England and Wales, registration number: 11086078, 7th floor, 10 Lower Thames Street, London, EC3R 6AF, United Kingdom

Printed in Croatia

British Library Cataloguing-in-Publication Data

A catalogue record for this book is available from the British Library

Additional hard and PDF copies can be obtained from [orders@intechopen.com](mailto:orders@intechopen.com)

Magnesium - The Wonder Element for Engineering/Biomedical Applications

Edited by Manoj Gupta

p. cm.

Print ISBN 978-1-78923-841-9

Online ISBN 978-1-78923-842-6

eBook (PDF) ISBN 978-1-83880-615-6

# We are IntechOpen, the world's leading publisher of Open Access books Built by scientists, for scientists

4,600+

Open access books available

120,000+

International authors and editors

135M+

Downloads

151

Countries delivered to

Our authors are among the  
Top 1%

most cited scientists

12.2%

Contributors from top 500 universities



WEB OF SCIENCE™

Selection of our books indexed in the Book Citation Index  
in Web of Science™ Core Collection (BKCI)

Interested in publishing with us?  
Contact [book.department@intechopen.com](mailto:book.department@intechopen.com)

Numbers displayed above are based on latest data collected.  
For more information visit [www.intechopen.com](http://www.intechopen.com)







# Meet the editor



Dr Manoj Gupta was formerly the Head of Materials Division of the Mechanical Engineering Department and Director designate of the Materials Science and Engineering Initiative at NUS, Singapore. In August 2017, he was chosen for the Top 1% Scientist of the World position by The Universal Scientific Education and Research Network and achieved 2.5% among scientists as per ResearchGate. He has published over 545 peer-reviewed journal papers and owns two US patents and one trade secret. His current h-index is 63, RG index is > 47, and citations are greater than 15000. He has also co-authored six books, published by John Wiley, Springer, and MRF - USA. He is Editor-in-chief/ Editor of twelve international peer-reviewed journals. A multiple award winner, he actively collaborates with and visits Japan, France, Saudi Arabia, Qatar, China, USA and India as a visiting researcher, professor, and chair professor.



# Contents

<b>Preface</b>	<b>XIII</b>
<b>Chapter 1</b> Introductory Chapter: An Insight into Fascinating Potential of Magnesium <i>by Sravya Tekumalla and Manoj Gupta</i>	<b>1</b>
<b>Chapter 2</b> Synthesis of Magnesium Based Nano-composites <i>by Srinivasan Murugan, Quy Bau Nguyen and Manoj Gupta</i>	<b>11</b>
<b>Chapter 3</b> Severely Plastic Deformed Magnesium Based Alloys <i>by Ramesh Kumar Subramanian, Arun Kumar Srirangan and SreeArravind Mani</i>	<b>31</b>
<b>Chapter 4</b> Fatigue of Magnesium-Based Materials <i>by Jafar Albinmousa</i>	<b>45</b>
<b>Chapter 5</b> Abrasive Water Jet Cutting: A Risk-Free Technology for Machining Mg-Based Materials <i>by Niranjana Channagiri Anandathirachar, S. Srinivas and M. Ramachandra</i>	<b>61</b>
<b>Chapter 6</b> Dissimilar Welding and Joining of Magnesium Alloys: Principles and Application <i>by Kaviani O. Cooke, Abdulaziz Alhazaa and Anas M. Atieh</i>	<b>83</b>
<b>Chapter 7</b> Magnesium-Based Materials for Hydrogen Storage: Microstructural Properties <i>by Ryota Kondo and Takeshita T. Hiroyuki</i>	<b>103</b>



# Preface

Magnesium is a magical element that is the lightest among other elements in context of its structural applications and it is also one of the most abundant metallic elements available on Earth. It possesses nutritional characteristics and is hence important in many biological ways for plants, animals, and humans. Its light weight (~33% lighter than aluminum) makes it a suitable candidate for a wide spectrum of engineering and biomedical applications in the context of reducing fuel consumption, mitigating global warming, and enhancing human comfort through development of prosthetics with a similar density to that of bone. The abundance of magnesium in the Earth's crust and water bodies, coupled with its nutritional characteristics, also enables magnesium to provide a sustainable solution to humans for a very long time to come. In view of its non-toxic nature, the recycling of magnesium is also easily achievable and illegal dumping will not be a health hazard.

From an engineering perspective, the transportation sector (land, air, space, and water transport), defense sector, and electronic sector can be key beneficiaries of using magnesium-based materials. From a biomedical perspective, the most promising application is related to temporary implants. The use of magnesium-based materials as temporary implants assists in reducing patient trauma and medical costs through eliminating the need of revision surgery. From an industrial perspective, magnesium is an attractive option as it has a low melting point and easy machinability and these are instrumental in minimizing the cost of end components.

In view of the tremendous advantages associated with use of magnesium-based materials, this book was conceptualized to provide an insight into the fundamental characteristics of magnesium and the current directions pursued by researchers worldwide. Chapter 1, written by Dr. Tekumalla and Dr. Gupta, introduces the readers to magnesium-based materials and their applications. Chapter 2, written by Srinivasan Murugan, Manoj Gupta, and Nguyen Quy Bau et al., describes the synthesis of magnesium-based nanocomposites using different methodologies. The focus in this chapter is on nanocomposites due to their unique capability of exhibiting a superior combination of mechanical properties that is desired by engineers for developing high performance systems. The third chapter, written by Ramesh Kumar Subramanian, Sreeravind M., and Arun Kumar Srirangan et al., addresses the importance of severe plastic deformation in refining the microstructure and enhancing the mechanical response of magnesium-based materials. In the fourth chapter, by Dr. Jafar Albinmousa, the author describes the fatigue of magnesium-based materials including composites in a comprehensive manner. The fifth chapter, by Niranjan C A, Ramachandra Madhavarao, and Srinivas Satyanarayana et al., introduces the potential of risk-free abrasive water jet cutting technology as an alternative method for machining magnesium-based materials. The intricacies associated with water jet cutting are addressed by the authors in this chapter. The sixth chapter, by Kavian Cooke, Anas Attieh, and Abdulaziz Alhazaa et al., addresses the principles and applications of dissimilar welding and joining of magnesium alloys. This chapter highlights the importance of dissimilar welding as multi-material systems are commonly in place in both the biomedical and

engineering sectors. Finally, in the seventh chapter, by Dr. Kondo and Dr. Hiroyuki, the use of magnesium-based materials is illustrated for hydrogen storage with critical analysis related to microstructure.

Overall, the chapters included in this book address the latest trends in primary and secondary processing, properties characterization, machining, joining, and application of magnesium-based materials including nanocomposites. The information contained in this book will be of immense importance to graduate students and researchers from research-based institutions, industry, and academia.

**Manoj Gupta, PhD**  
Department of Mechanical Engineering,  
National University of Singapore,  
NUS, Singapore

# Introductory Chapter: An Insight into Fascinating Potential of Magnesium

*Sravya Tekumalla and Manoj Gupta*

## 1. Evolution of magnesium

The name, magnesium (Mg), was derived from an ancient city in Greece called “Magnesia” where magnesium carbonate was first discovered. It was first isolated in its elemental form by English chemist Sir Humphry Davy in 1808 [1]. In the earth’s crust, magnesium is the sixth most abundant element and occurs in over 60 different minerals with at least 20% of Mg within them. Most commercially important of these minerals include dolomite, magnesite, brucite, and carnallite. Principally, magnesium is extracted from its minerals using a thermal reduction process [2]. Magnesium is also the third most abundant metal ion in seawater. Despite magnesium being only 0.13% of seawater, seawater remains an almost inexhaustible source for its extraction. Magnesium is extracted from seawater or brine using the electrolytic process of magnesium chloride [2]. Of the two extraction processes, the thermal reduction process is known to yield a higher purity of 99.99%, while the electrolysis process can achieve purity limited to 99.8%. Until the 1990s, the USA and Canada dominated the production of magnesium; however, the industrial revolution in China in the late 1990s turned the tables for magnesium production due to its lower operational (energy and labor) costs. It is estimated that 85% of the global magnesium production is currently done by China, and most of the remainder is produced by Russia, Turkey, Spain, Austria, etc. [3].

## 2. Factsheet of magnesium

The salient characteristics including atomic and crystalline and chemical characteristics and physical, thermal, biological, and mechanical properties of magnesium are shown in **Figure 1**.

## 3. Past, current, and potential applications of magnesium

Among metallic materials, aluminum is currently the most widely used light-weight material with a density of 2.7 g/cc. Titanium (Ti) and steels are heavier and are used very strategically in the transportation sector. Being abundantly available with price only marginally higher than that of Al (**Table 1**), magnesium-based materials are the present emerging materials in multiple sectors after a gap of about 70 years when they were used initially in aerospace and automobile sectors. This is because magnesium offers multidimensional properties which can be harnessed in a

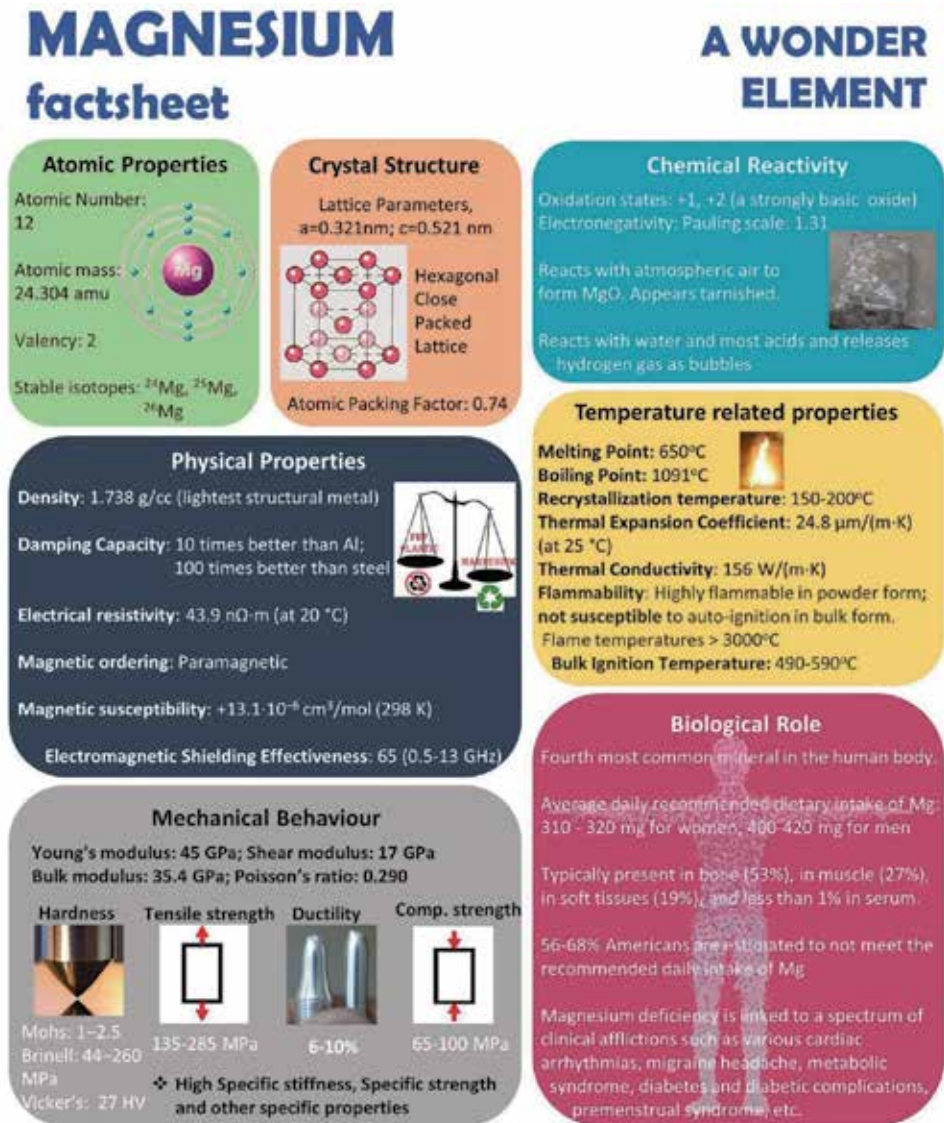


Figure 1. Factsheet of magnesium.

Metal	Density (g/cc)	Price/kg (US\$) (in 2016) [4]
Magnesium	1.738	4.71
Aluminum	2.7	2.13
Titanium	4.506	8
Steel	7.75-8.05	0.64

Table 1. Price of the most commonly used metals.

variety of applications. These applications of magnesium are primarily classified into three categories: (i) structural, (ii) nonstructural, and (iii) miscellaneous applications. They are discussed briefly in this chapter.



### 3.1 Structural applications

About 40% of magnesium produced globally is directly used in the form of its alloys in structural applications [5] in different sectors described below in text as well as shown in **Figure 2**.

#### 3.1.1 Automotive sector

The first automobile in the world (1885–1886) was made up of steel, a dense alloy, in most of its parts. With increasing efforts to improve fuel efficiency and energy efficiency as well as to reduce the cost of the vehicles, there was a shift from usage of steel to aluminum (owing to its lower density) that substantially reduced the weight of the automobiles. However, in recent years, driven by lower density of magnesium (33% lighter than Al), car manufacturers such as Porsche, Suzuki, and General Motors are increasingly using magnesium-based materials primarily due to their excellent specific mechanical and physical properties. Among several magnesium alloys, Mg-Al-based alloy series such as the AZ and AM alloys; Mg-rare earth-based alloys, i.e., WE43 and E21; and ZK alloys demonstrate good strength and ductility combination at room temperature along with good resistance to corrosion (salt spray) and superior castability [6]. Hence, they are predominantly being used in the automobile sector as sheets or even engine blocks and other automobile components such as in steering wheels, boot area, etc. Further, for robust and elevated temperature applications such as engine blocks, newly developed high-strength magnesium alloys and alloy nanocomposites can be used as they demonstrate good thermal and dimensional stabilities [7–11].

#### 3.1.2 Aerospace sector

Historically (in the 1950s), magnesium was a dominant material in the aviation industry as a structural material. In fact, an aircraft (XR56) with all-magnesium was

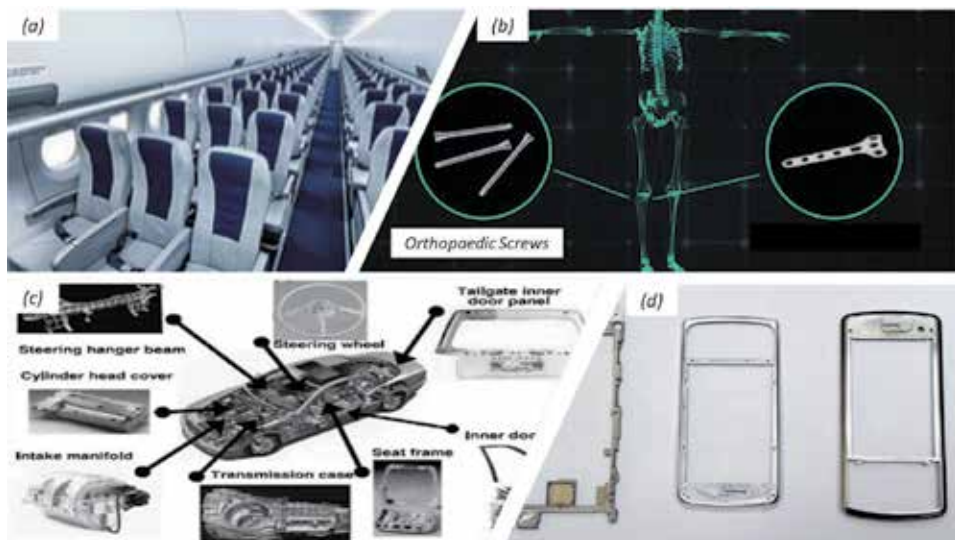


**Figure 2.** Potential applications of Mg in (a) aerospace sector in the form of passenger seats (image taken from [25]); (b) biomedical sector where biodegradable magnesium alloy products can be used as implants, assist in fracture fixation, etc. (image taken from [26]); (c) automobile applications (image extracted from [27]); and (d) electronic applications such as mobile handset panels and casings (image used from [28]).

built by Northrop in 1943 during the World War period, similar to the Lockheed F-80C in 1950 [12]. With the “traditional” challenges such as reactivity and perceived flammability, magnesium usage was limited. Ever since upliftment of the ban on magnesium by FAA [13], there is an ever-increasing demand for high-performance magnesium alloys for reducing weight in aircraft structures such as interior components, fuselage structures, gearboxes, aero engine frames, helicopter transmissions, covers and components, flight control systems, electronic housings, and aircraft wheels [14]. With advancement in the alloy design and material development, for the abovementioned as well as other applications in both commercial and military aircrafts, advanced higher-performance magnesium alloys and composites that are also ignition-resistant or ignition proof and corrosion-resistant suit the requirement of the aviation industries and can help in achieving sustainability and protecting the environment [8, 15–17].

### *3.1.3 Electronic sector*

In consumer electronic industries, due to the shortcomings of plastics that do not shield the electromagnetic radiations, have poor stiffness, and generate enormous scrap of electronic equipment, there is a need for nontoxic lightweight materials that can match the density of the commonly used plastics and perform better than that of plastics. These attributes are the reason that makes magnesium-based materials very lucrative as magnesium can be remelted, reused, and recycled. Its electromagnetic shielding capacity (65–66 in 0.5–13 GHz frequency range) is the same or even superior to that of aluminum alloys (59–65 in 0.5–13 GHz frequency range) [18–20]. Magnesium is currently one of the most sought-after materials for making the casings, frames, panels, and other parts in the electronic items such as mobile phones, laptops, cameras, etc. [21].

### *3.1.4 Biomedical sector*

Mg is the fourth most abundant ion in the human body and assists in several functions like aiding bone health and multiple metabolic processes in the body besides being antibacterial and attracts attention as an excellent biomaterial [22]. Since magnesium is both biocompatible and biodegradable, it is the best fit to be used in the body as a nonpermanent biodegradable implant as it (i) reduces patient trauma; (ii) requires no revision surgery; (iii) reduces doctor’s time; and (iv) reduces medical costs [23]. Further, it is also required by the body as it is instrumental for about 300 enzyme systems and assists in energy production and synthesis of nucleic acid in the body [24]. Further, there is good evidence for the use of supplemental Mg in various cardiac arrhythmias, preeclampsia/eclampsia, migraine headache, diabetes and related complications, metabolic syndrome, premenstrual syndrome, asthma, and hyperlipidemia [24], indicating the significance of magnesium in human bodies and biomedical sectors.

## **3.2 Nonstructural applications**

### *3.2.1 Alloying element to aluminum*

On par with its direct structural applications, magnesium is used primarily as an alloying element to Al (about 40% of magnesium produced globally is used for alloying with aluminum). Magnesium is alloyed with aluminum up to 30% catering to suit a range of applications including pyrotechnics [29]. Some applications of Al-Mg alloys are as sheets in automobile applications and shipping industry due to

their good mechanical properties, castability, and superior corrosion resistance, owing to the presence of elevated magnesium content [30].

### 3.2.2 Refining titanium

Magnesium acts as a reducing agent in the production of titanium, beryllium, zirconium, uranium, and hafnium. It is the second largest use of Mg in a nonstructural market. In applications related to organic chemistry, magnesium is also used in industrial synthesis such as the Grignard reaction. Particularly, Mg is important for production of Ti sponges [31].

### 3.2.3 Steel desulfurization

Sulfur (0.025–0.03% S) is damaging to steel and causes brittleness. Hence, desulfurization of steel is done by exploiting the high affinity exhibited by

Minor applications	Advantages of using magnesium and other remarks
Sacrificial anode [35]	High-resistivity environment that have high current output per unit weight and inherent negative potential are particularly suitable for magnesium anodes. Some applications include underground pipelines, domestic water heaters, storage tanks, and other similar environments, where the galvanic corrosion of steel can be prevented by employing magnesium anodes. With suppressing the corrosion, the safety and resource conservation can be increased as the number of leaks decrease drastically
Magnesium batteries [36, 37]	A range of Mg batteries are under development in recent years for various applications. One such application includes that of military applications where magnesium is used in reserve cell batteries and dry cells. Magnesium batteries have (i) long shelf life (up to 10 years), (ii) high cell voltage and wide voltage range, (iii) high power density capacity, and (iv) lightweight in their inactivated state
Hydrogen storage [38]	Hydrogen is a plentiful yet largely untapped potential energy source. Hydrogen fuel cell prototype engines are 3–4 times more efficient than internal combustion engines. 10 kg of Mg can store roughly 0.67 kg of hydrogen. Mg can absorb about 7.6 wt. % hydrogen, which makes it one of the largest capacities among metal hydride alloys. Recently reported air-stable magnesium nanocomposites assist in nanostructuring, resulting in rapid storage kinetics by eliminating the need for usage of expensive heavier metal catalysts
Flameless ration heater (FRH) [39]	FRH is an exothermic chemical heater activated by water, applied to heat the food (especially in meal, ready-to-eat (MREs)). Ration heat is generated in an oxidation–reduction reaction which involves the transfer of electrons. US military specifications for the heater require it to be capable of raising the temperature of an 8-ounce (226.8 g) entree by 100°F (38°C) in 12 minutes and that it has no visible flame. The ration heater typically contains finely powdered magnesium metal, alloyed with a small amount of iron, and table salt. A little amount of water is to be used to activate the reaction, and the reaction proceeds when the boiling point of water is quickly reached [40]
Alkaline water	Mg alkaline water has a pH of 8.5–10 (vs. pH of water = 7–7.4). Pure Mg, Mg-Zn alloy, and Mg-Ca alloy are potential materials used. Al is not to be used as Al is linked to Alzheimer's disease
Fire starter	Due to its high flammability in fine or powdered forms, it is an ideal choice in this application. The fire starter is composed of an Mg block and flint stone. Typical applications include military, leisure, and emergency [41]

**Table 2.**  
*Miscellaneous applications of magnesium-based materials.*

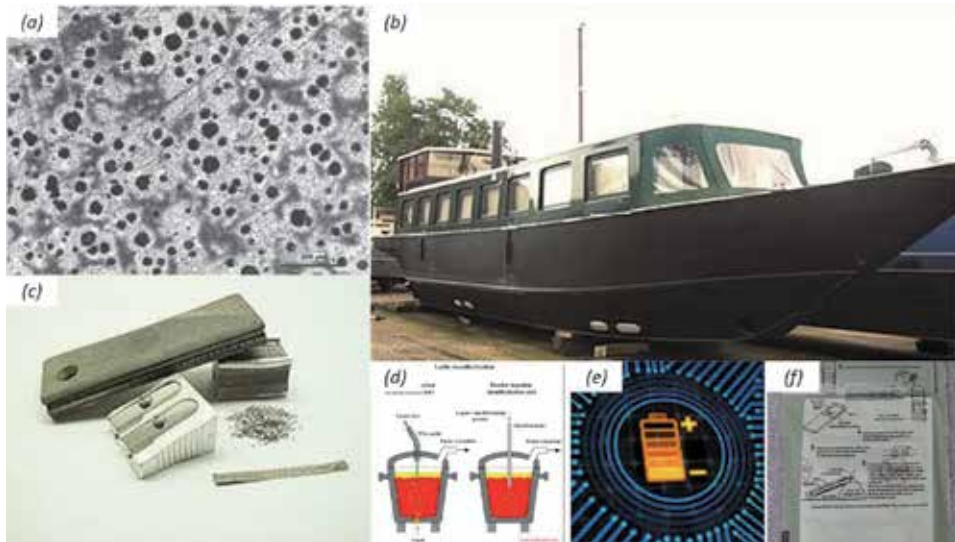


**Figure 3.** Miscellaneous applications of magnesium in (a) nodularizing iron (image taken from [42]); (b) anodes, a steel wide-beam canal barge showing a newly blacked hull is protected with the help of new magnesium anodes (image taken from [43]); (c) fire starter, shavings, sharpener, and ribbons (image taken from [44]); (d) desulfurization of steel (image reproduced from [45]); (e) new generation fast magnesium-ion solid-state electrolyte batteries (image taken from [46]); and (f) flameless ration heater (image taken from [47]).

magnesium to sulfur. It is the third largest use of Mg in a nonstructural market. Magnesium is added to molten iron or steel which helps in reacting with sulfur and reduces the sulfur in the steel [32].

### 3.2.4 Iron nodularization

For nodularizing cast iron, magnesium is used to produce spheroidal graphite cast iron or nodular cast iron. The addition of magnesium to cast material assists in the formation of nodules instead of flakes resulting in improved ductility. Typically, nodular cast iron is used in several components in automotive sector and pipes [33].

### 3.2.5 Photoengraving

Printing industry uses wrought (plates) of magnesium alloys for photoengraving. This is because Mg etches rapidly, hence creating a sharp impression. Further, it also creates less hazardous by-products as compared to alternative metals [34].

## 3.3 Miscellaneous applications

Table 2 and Figure 3 list minor applications where magnesium is currently/can be potentially employed.

## 4. Concluding remarks

In this introductory chapter, a snapshot on the diverse and multidimensional properties and capabilities of magnesium is introduced. In view of the environmental conservation and lightweighting, and to improve the fuel and cost

efficiency, magnesium is strongly emerging in weight-critical structural applications such as in the automobile, aerospace, space, and defense sectors. Further, as magnesium is light, recyclable, an excellent dampener, and an efficient electromagnetic shielder, it finds a remarkable place in the electronic industry. In addition, with its biodegradability and nontoxicity coupled with its low elastic modulus, almost matching that of the bone, it is a potential material as a nonpermanent implant in the human body. It is also an extremely important element used in several other applications such as alloying element to Al, refining of Ti, desulfurization of steel, fire starter, etc. Thus, magnesium is a potentially a very important eco-friendly metal that is opening multibillion dollar markets in many industrial sectors.

## Author details

Sravya Tekumalla<sup>1</sup> and Manoj Gupta<sup>2\*</sup>


<sup>1</sup> School of Mechanical and Aerospace Engineering, Nanyang Technological University, Singapore

<sup>2</sup> Department of Mechanical Engineering, National University of Singapore, Singapore

\*Address all correspondence to: [mpegm@nus.edu.sg](mailto:mpegm@nus.edu.sg)

## IntechOpen

---

© 2020 The Author(s). Licensee IntechOpen. This chapter is distributed under the terms of the Creative Commons Attribution License (<http://creativecommons.org/licenses/by/3.0>), which permits unrestricted use, distribution, and reproduction in any medium, provided the original work is properly cited. 

## References

- [1] Friedrich HE, Mordike BL, editors. *Magnesium Technology: Metallurgy, Design Data, Applications*. Berlin, Heidelberg: Springer Berlin Heidelberg; 2006. pp. 1-28
- [2] Wulandari W, Brooks GA, Rhamdhani MA, Monaghan BJ. *Magnesium: Current and Alternative Production Routes*, Chemeca 2010: Engineering at the Edge; 26–29 September 2010. South Australia: Hilton Adelaide; 2010. p. 347
- [3] Wada Y, Fujii S, Suzuki E, Maitani MM, Tsubaki S, Chonan S, et al. Smelting magnesium metal using a microwave Pidgeon method. *Scientific Reports*. 2017;7:46512
- [4] Kardys G. *Magnesium Car Parts: Cost Factors (Part 2)*. New York, USA: IEEE Globalspec; 2017
- [5] Kumar DS, Sasanka CT, Ravindra K, Suman K. Magnesium and its alloys in automotive applications—A review. *American Journal of Materials Science and Technology*. 2015;4:12-30
- [6] Kulekci MK. Magnesium and its alloys applications in automotive industry. *The International Journal of Advanced Manufacturing Technology*. 2008;39:851-865
- [7] Trang TTT, Zhang JH, Kim JH, Zargaran A, Hwang JH, Suh BC, et al. Designing a magnesium alloy with high strength and high formability. *Nature Communications*. 2018;9:2522
- [8] Tekumalla S, Nandigam Y, Bibhanshu N, Rajashekara S, Yang C, Suwas S, et al. A strong and deformable in-situ magnesium nanocomposite igniting above 1000 °C. *Scientific Reports*. 2018;8:7038
- [9] Chen Y, Tekumalla S, Guo YB, Gupta M. Introducing Mg-4Zn-3Gd-1Ca/ZnO nanocomposite with compressive strengths matching/exceeding that of mild steel. *Scientific Reports*. 2016;6:32395
- [10] Yang W, Tekumalla S, Gupta M. Cumulative effect of strength enhancer—Lanthanum and ductility enhancer—Cerium on mechanical response of magnesium. *Metals*. 2017;7:241
- [11] Tekumalla S, Shabadi R, Yang C, Seetharaman S, Gupta M. Strengthening due to the in-situ evolution of  $\beta_1'$  Mg-Zn rich phase in a ZnO nanoparticles introduced Mg-Y alloy. *Scripta Materialia*. 2017;133:29-32
- [12] Wendt A, Weiss K, Ben-Dov A, Bamberger M, Bronfin B. Magnesium castings in aeronautics applications—Special requirements. In: Mathaudhu SN, Luo AA, Neelameggham NR, Nyberg EA, Sillekens WH, editors. *Essential Readings in Magnesium Technology*. Cham: Springer International Publishing; 2016. pp. 65-69
- [13] Tekumalla S, Gupta M. An insight into ignition factors and mechanisms of magnesium based materials: A review. *Materials and Design*. 2017;113:84-98
- [14] Czerwinski F. Controlling the ignition and flammability of magnesium for aerospace applications. *Corrosion Science*. 2014;86:1-16
- [15] Chen Y, Tekumalla S, Guo YB, Shabadi R, Shim VPW, Gupta M. The dynamic compressive response of a high-strength magnesium alloy and its nanocomposite. *Materials Science and Engineering A*. 2017;702:65-72
- [16] Johaness M, Tekumalla S, Gupta M. Fe<sub>3</sub>O<sub>4</sub> nanoparticle-reinforced magnesium Nanocomposites processed via disintegrated melt deposition and

turning-induced deformation techniques. *Metals*. 2019;**9**:1225

[17] Tekumalla S, Gupta M, Min KH. Using CaO nanoparticles to improve mechanical and ignition response of magnesium. *Current Nanomaterials*. 2018;**3**:44-51

[18] Pandey R, Tekumalla S, Gupta M. Magnesium-iron micro-composite for enhanced shielding of electromagnetic pollution. *Composites Part B: Engineering*. 2019;**163**:150-157

[19] Pandey R, Tekumalla S, Gupta M. Enhanced (X-band) microwave shielding properties of pure magnesium by addition of diamagnetic titanium micro-particulates. *Journal of Alloys and Compounds*. 2019;**770**:473-482

[20] Pandey R, Tekumalla S, Gupta M. Effect of defects on electromagnetic interference shielding effectiveness of magnesium. *Journal of Materials Science: Materials in Electronics*. 2018; **29**:9728-9739

[21] Monteiro WA. The influence of alloy element on magnesium for electronic devices applications—A review. In: *Light Metal Alloys Applications*. Rijeka: IntechOpen; 2014

[22] Al Alawi AM, Majoni SW, Falhammar H. Magnesium and human health: Perspectives and research directions. *International Journal of Endocrinology*. 2018;**2018**: 9041694-9041694

[23] Gupta M. A snapshot of remarkable potential of mg-based materials as implants. *Material Science and Engineering International Journal*. 2018; **2**:30-33

[24] Schwalfenberg GK, Genuis SJ. The importance of magnesium in clinical healthcare. *Scientifica (Cairo)*. 2017; **2017**:4179326-4179326

[25] Airline seat, in Wikipedia

[26] Biodegradable Mg-Alloy Implant, in Eon

[27] Automotive Uses of Magnesium Alloys: Part One, in *Total Materia*; 2010

[28] Koh D. LG to slash CO2 emissions with eco-magnesium, in *cnet*; 2010

[29] Quijano D, Corcoran AL, Dreizin EL. Combustion of mechanically alloyed Aluminum-magnesium powders in steam. *Propellants, Explosives, Pyrotechnics*. 2015;**40**:749-754

[30] Król M, Tański T, Snopiński P, Tomiczek B. Structure and properties of aluminium–magnesium casting alloys after heat treatment. *Journal of Thermal Analysis and Calorimetry*. 2017;**127**: 299-308

[31] Platacis E, Kaldre I, Blumbergs E, Goldšteins L, Serga V. Titanium production by magnesium thermal reduction in the electroslag process. *Scientific Reports*. 2019;**9**:17566

[32] Schrama FNH, Beunder EM, Van den Berg B, Yang Y, Boom R. Sulphur removal in ironmaking and oxygen steelmaking. *Ironmaking & Steelmaking*. 2017;**44**:333-343

[33] Mohla PP. In situ furnace metal desulfurization/nodularization by high purity magnesium, in *Google Patents*; 1981

[34] Avedesian MM, Baker H. *ASM Specialty Handbook: Magnesium and Magnesium Alloys*. Ohio, USA: ASM International; 1999

[35] Juárez-Islas JA, Genesca J, Pérez R. Improving the efficiency of magnesium sacrificial anodes. *JOM*. 1993;**45**:42-44

[36] Aurbach D, Lu Z, Schechter A, Gofer Y, Gizbar H, Turgeman R, et al. Prototype systems for rechargeable magnesium batteries. *Nature*. 2000;**407**: 724-727

[37] Tian H, Gao T, Li X, Wang X, Luo C, Fan X, et al. High power rechargeable magnesium/iodine battery chemistry. *Nature Communications*. 2017;**8**:14083

[38] Jeon K-J, Moon HR, Ruminski AM, Jiang B, Kisielowski C, Bardhan R, et al. Air-stable magnesium nanocomposites provide rapid and high-capacity hydrogen storage without using heavy-metal catalysts. *Nature Materials*. 2011; **10**:286-290

[39] Lamensdorf M. Flameless Heater and Method of Making Same. US: Magnesium Elektron; 1995

[40] Brain M. How MREs Work, in *Howstuffworks*; 2003

[41] Wu Y, Yao C, Hu Y, Zhu X, Qing Y, Wu Q. Comparative performance of three magnesium compounds on thermal degradation behavior of red gum wood. *Materials (Basel)*. 2014;**7**: 637-652

[42] *D. iron*, in Wikipedia

[43] Galvanic anode, in Wikipedia

[44] Magnesium, in Wikipedia

[45] Kopeliovich D. SubsTech, Desulfurization of steel

[46] Magnesium batteries could be safer and more efficient than lithium, in *Engadget*

[47] Flameless ration heater, in Wikipedia



# Synthesis of Magnesium Based Nano-composites

*Srinivasan Murugan, Quy Bau Nguyen and Manoj Gupta*

## Abstract

Magnesium based nanocomposites are new lightweight and high-performance materials for potential applications in automotive, aerospace, space, electronics, sports and biomedical sectors primarily due to their lower density when compared to aluminum-based materials and steels. Synthesis of magnesium-based materials is relatively challenging and accordingly this chapter explicitly provides an insight into various techniques hitherto devised/adopted by various researcher for synthesizing magnesium based nano-composites (MMNCs). Overall processing of MMNCs often includes combination of primary and secondary processing. Primary processing fundamentally leads to the initial formulation and creation of MMNC ingots by solid, semi-solid or liquid state processing routes. This is followed by secondary processing that includes plastic deformation or severe plastic deformation to alleviate inhomogeneity, clustering of particles and fabrication defects to enhance the properties of the MMNCs. This chapter provides an insight into different fabrication methodologies, their benefits and limitations for MMNCs.

**Keywords:** magnesium, reinforcement, nano-composite, MMNC, synthesis

## 1. Introduction

Research on magnesium based-composites has seen sustainable growth in last four decades due to their light weight, higher strength to weight ratio, ductility, hardness, wear resistance and biodegradability [1, 2]. Magnesium based materials, in general, are currently targeted for applications in automotive, aerospace, electronics, sports and biomedical engineering. The driving force for intense research into magnesium-based nano-composites is to utilize them to mitigate global warming, energy consumption and land, air and water toxicity. The presence of reinforcement at nano-length scale leads to grain refinement leading to Hall-Petch strengthening and Orowan strengthening due to presence of nano-particles/fibers with diameter less than 100 nm [3].

The primary processing of MMNCs can be categorized in two groups i.e. ex situ and in situ routes [4]. In ex situ processing during fabrication of MMNCs the major issue is particle clustering. High surface energy navigates to poor wettability of particles/fibers with the matrix during liquid and semi-solid processing. These clustered particles lead to reinforcement distribution inhomogeneity in the matrix leading to inferior properties in as-cast state. Such non-uniform distribution can only be reduced through judicious secondary processing step.

The common liquid and semi-solid ex situ process are stir casting/melt stirring, ultrasound cavitation, disintegrated melt deposition (DMD) and Rheocasting. The solid-state ex situ syntheses are powder metallurgy (PM), severe plastic deformation (SPD) by accumulative roll bonding (ARB) and plastic deformation by friction stir processing. The in-situ processes eliminate the reinforcement clustering, since the reinforcements are distributed in the matrix by thermodynamic and chemical reaction during the process.

The MMNCs processed by ex situ route commonly exhibit microstructural defects such as dendrites, pores, and micro cracks. These require careful characterization followed by using a secondary processing technique that can target the property enhancement required by end application. The common secondary processes are thermal treatment, hot extrusion, hot rolling, equal channel angular pressing (ECAP) and cyclic extrusion and compression (CEC).

The prime objective of this chapter is to provide an overview of various processing methods used currently for synthesizing MMNCs, their benefits and limitations. Critical observations made by other researchers are also highlighted in this chapter.

## **2. Processing methods**

The processing methodology for fabricating magnesium based nano-composites (MMNCs) normally includes coupling of primary and secondary processing. In primary processing (solid, liquid or two phase), the matrix (master alloy) and the reinforcements are blended together by the application of thermal or mechanical energy to form a composite. During primary processing some undesirable effects are introduced in the composites such as porosity and non-uniform distribution of reinforcement voids. To minimize these defects, secondary processing is utilized to attain a relatively homogeneous microstructure and enhanced mechanical properties.

### **2.1 Primary processing**

Primary processing techniques are grouped into liquid state, semi-solid and solid state processing types. The liquid state processes are stir casting, ultrasonic cavitation (UST), disintegrated melt deposition (DMD), in-situ processing. Rheocasting is a semi-solid composite primary processing. The solid-state fabrication includes powder metallurgy (PM), accumulated roll bonding (ARB) and friction stir processing (FSP). These techniques are briefly introduced in following subsections.

#### *2.1.1 Stir casting*

Stir casting is one of the most common liquid-phase technique utilized for processing MMCs for almost last four decades. The schematic of stir casting setup is shown in the **Figure 1**.

For processing MMNCs, the Mg ingots are melted in a crucible made of graphite or steel at a temperature between 680 and 750 °C in an electric resistance or induction furnace. The liquid melt is mechanically stirred using a coated impeller. The coating is provided onto the impeller to avoid erosion by abrasion and chemical reaction. Predetermined amount of nano-reinforcement is introduced in molten metal along the side of the vortex. The reinforcements were distributed in the melt due to the difference in pressure from the inner to outer surface of the liquid

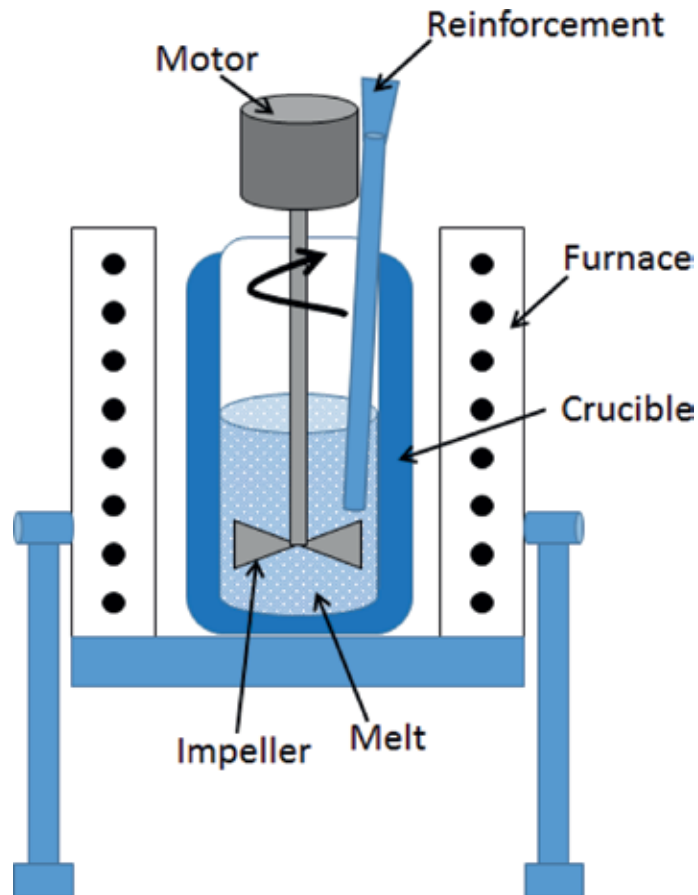


**Figure 1.**  
*Schematic of stir casting setup.*

vortex. The vortex is shielded using inert atmosphere to avoid oxidation /ignition. Alternatively, to overcome agglomeration/clustering, the powders of magnesium and the nano reinforcement are ball milled together prior to addition. The liquid slurry is stirred for ~10 min to homogenize the mixture. After homogenization, the liquid slurry is poured into a permanent mold. MMNCs reinforced with  $\text{Al}_2\text{O}_3$ , SiC and CNTs are commonly synthesized using stir casting technique [5–16].

The benefits of stir casting include: (a) ease of processing, (b) economical, and (c) scalability to ensure large volume production. Disadvantages of stir casting includes: (a) unavoidable agglomeration of reinforcement and (b) porosity.

### 2.1.2 Ultrasonic cavitation method

One of the main drawback of the stir casting technique is its inability to avoid agglomeration of nano-reinforcement due to their larger surface energy. This causes inferior mechanical properties of the end composites. Ultrasonic (UST) cavitation method is a relatively more effective technique to disperse the reinforcement into the matrix material in MMCs [17]. By introducing the ultrasonic waves with power and frequency range of as low as 1.5–4.0 kW and 17.5–20 kHz the agglomerates can be fragmented, and a uniform distribution of reinforcement can be realized in the liquid melt. This method has been adopted so far to produce MMNCs reinforcing with CNTs, AlN, SiC,  $\text{B}_4\text{C}$  and  $\text{Al}_2\text{O}_3$  [17–35]. The schematic of UST setup is shown in the **Figure 2**.

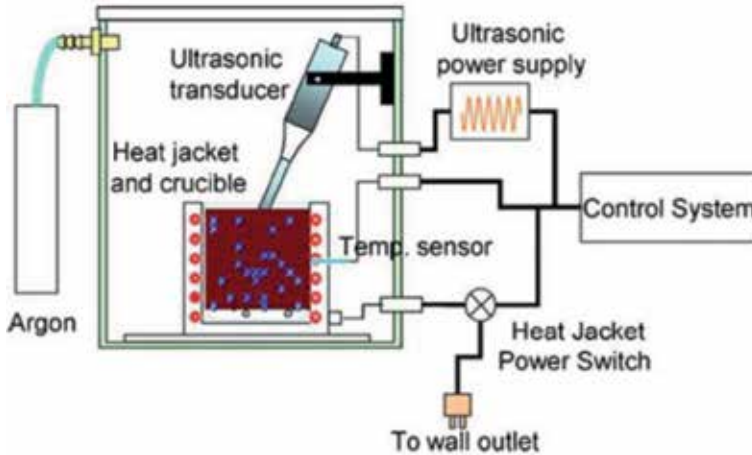


**Figure 2.**  
Schematic representation of UST [4].

In the UST process, the Mg alloy is placed in a graphite crucible and heated to the desired temperature using a resistance/induction furnace. Predetermined amount of reinforcement is then added depending on the size of the particles. During processing, Mg melt is protected using argon gas (flow rate of 20 lpm) to avoid oxidation. High-intensity ultrasound shock waves [16] are supplied to disperse nano-particles thoroughly in the melt at semi-solid temperature. The ultrasonic processing temperature is chosen so as to ensure better flowability of the slurry in the mold.

The selection of material for sonotrode plays a vital role in MMNCs melting due to the erosion of sonotrode surface during melting of liquid metal. For better sonification of MMNCs, niobium (Nb) and titanium (Ti) are recommended by the researchers. Ti-based sonotrodes are widely used for UST treatment due to lesser costs when compared to Nb-based sonotrodes. To note that Nb-based sonotrode exhibit less variation in the Young's modulus as the function of temperature while Ti-based sonotrodes are very stable in MMNCs melt as Ti is insoluble in Mg. Earlier findings have indicated that the high-intensity UST vibration needs an intensity of  $100 \text{ W/cm}^2$  [4]. For large scale volume production, the requirement of sonification is likely to be higher. The large-scale production of MMNCs require enormous power and frequencies. The key issue is reducing rate of sonification by decreasing the volume of the melt during UST. This can be achieved in two steps firstly, preparing the melt with reinforcement and secondly, passing the liquid melt into a sonotrode assisted UST chamber for fragmenting particle clusters. Further work is required in this area especially regarding scalability.

### 2.1.3 Disintegrated melt deposition method (DMD)

DMD technique is a hybrid technique that incorporates the concepts of casting, melt stirring and spray forming process [36–45]. In DMD, the processing steps involve:

- a. Heating matrix material and reinforcement in a graphite crucible (ceramic bonded clay graphite) to a desired superheat temperature. Mg and its alloys (in the form of chips or turnings) and reinforcement are placed in alternative layers.
- b. Stirring of reinforcement at  $\sim 450 \text{ rpm}$  for 5–10 min using a Zirtex 25 coated stainless-steel impeller realize uniform distribution.

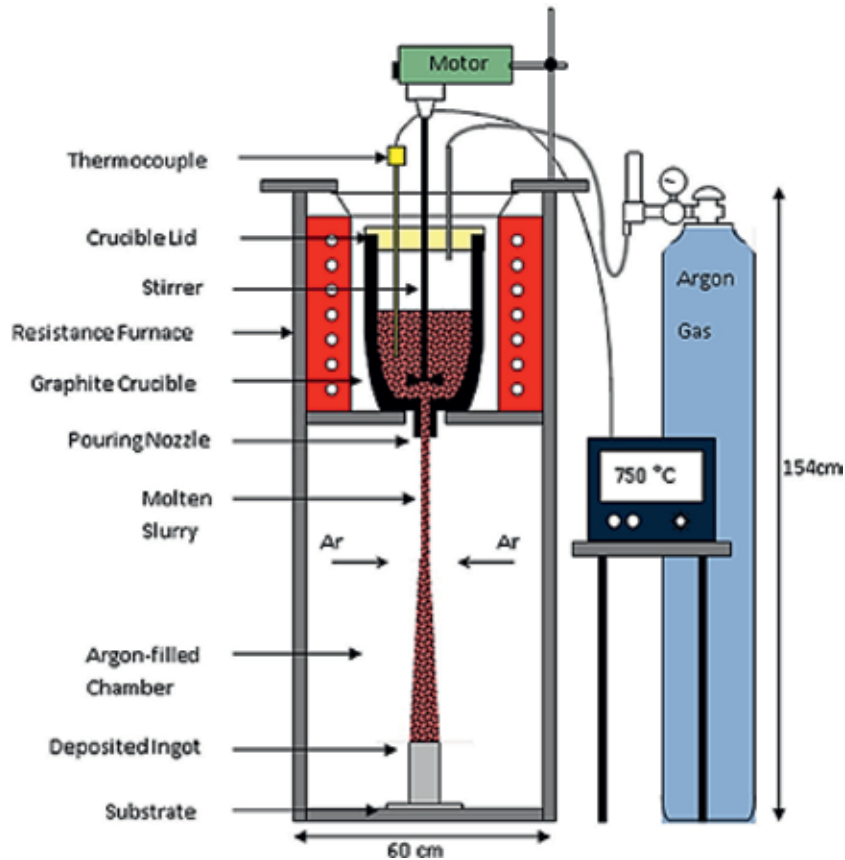


**Figure 3.**  
*Schematic drawing of DMD [35].*

- c. Bottom pouring of the slurry and disintegration of slurry through 10-mm annular diameter graphite nozzle.
- d. Disintegration of slurry using two argon gas jets.
- e. Deposition of disintegrated slurry into a steel mold to get 40-mm ingots.

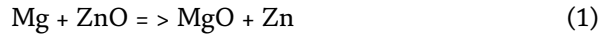
DMD processing is carried out under argon inert atmosphere to minimize oxidation. Experimental setup of DMD process is shown in **Figure 3**. The advantages of the method include:

- a. Bottom pouring of the liquid slurry to ensure almost 100% yield.
- b. Disintegration of molten slurry using low pressure gas jets to ensure improved particle distribution and microstructural homogeneity.
- c. Use of argon gas rather than SF<sub>6</sub> (greenhouse gas) to prevent oxidation.

#### 2.1.4 *In-situ casting processing*

In-situ casting of MMNCs is a very versatile and an economical process to synthesize MMNCs. The reinforcements are formed and controlled by metallurgical

reactions between principal alloy and the additives [46–50]. The type and number of additives are chosen based on final formulation of the matrix and volume fraction of the reinforcement. Reaction temperature is a key parameter in process design of in-situ MMNCs to ensure the desired matrix and the reinforcement phase. An example of creating in-situ Mg-Zn/MgO composites includes the use of Mg and ZnO as starting materials and heating them to a predetermined temperature to ensure the feasibility of the following two reactions (Eqs. (1) and (2)):



Chelliah et al. [46] synthesized magnesium-polymeric derived ceramic (PDC) silicon carbonitride (SiCNO) nano composite by liquid pyrolysis using stir casting technique. The liquid poly (urea-methyl-vinyl) silazane (PUVMS) was used to formulate magnesium nano-composite. In this method, magnesium was melted in a steel crucible using a resistance furnace at a temperature of 700 °C and shielded with Ar-5%SF<sub>6</sub> gas. The melt was stirred mechanically at 600 rpm to form vortex and the liquid PUVMS was injected to the melt. The melt was stirred for 15 min to ensure thorough pyrolysis. The liquid melt was bottom-poured into a rectangular metal mold preheated at 300 °C. Mg/nano- SiCNO composite was fabricated exhibiting uniform distribution of the reinforcement (**Figure 4**).

The benefits of in-situ MMNCs include: (a) uniform distribution of the reinforcement, (b) elimination of particle wettability issue, and (c) clean and strong matrix-particle interface. The disadvantages of in-situ techniques, in general, are scalability and the amount of reinforcements that can be created using the in-situ reactions.

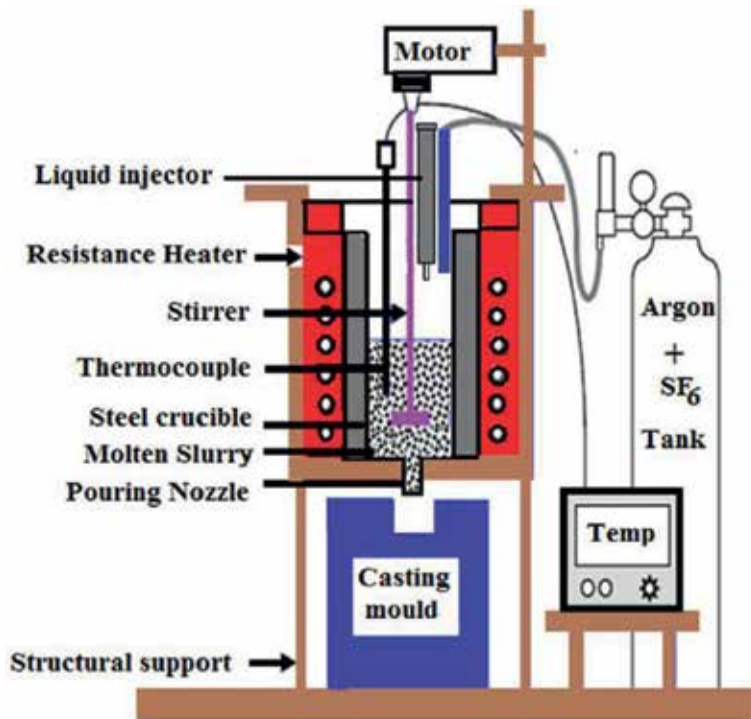


**Figure 4.** Experimental setup of liquid pyrolysis stir casting [45].

### 2.1.5 Rheocasting technique

Rheocasting is a semi-solid casting method where the matrix is processed in liquidus-solidus (L-S) zone. In this so called semi-solid zone, the reinforcement particles are added, and the resultant slurry is thoroughly stirred to ensure uniform distribution of the reinforcement. Following stirring, the semi-solid composite melt is tapped into a permanent mold. Often cleaning and degassing of the slurry is carried out to avoid oxidation and formation of inclusions.

A MMNC of Mg (AZ91E) with Al<sub>2</sub>O<sub>3</sub>n (50 nm) was synthesized using a semi-solid Rheocasting process [51]. The Mg ingots were placed in boron nitride coated mild steel crucible. The melt was formed in the metal crucible at 750 °C using electric resistant furnace. The slurry was degassed using argon to avoid oxidation. The reinforcement (Al<sub>2</sub>O<sub>3</sub>n) was then added to the slurry at semi-solid (L-S) temperature (~590 °C). The melt slurry was stirred using a mechanical stirrer. The MMNCs slurry was subsequently poured into a permanent mold for further characterization.

The benefits of this technique include: (a) spheroidal/equiaxed grains and no dendrites, (b) less shrinkage and porosity and (c) lower operating temperature.

### 2.1.6 Powder metallurgy

Powder metallurgy (PM) [52] is one of the most common solid-state synthesis method for magnesium based nano-composites [53–60]. The steps followed in PM are shown in **Figure 5**. In the first step metal alloy and ceramic particle in powder form are blended/mixed together to get homogenous mixture. The mixing parameters are decided based on the density difference between metal/alloy and reinforcement powder. The blended powders are subsequently compacted using a cold press or hot press or hot isostatic press. Finally, the green compacts are sintered by heating to a predetermined temperature to regain mechanical properties. Near-net-shaped components with simple geometries can be fabricated by PM technique.

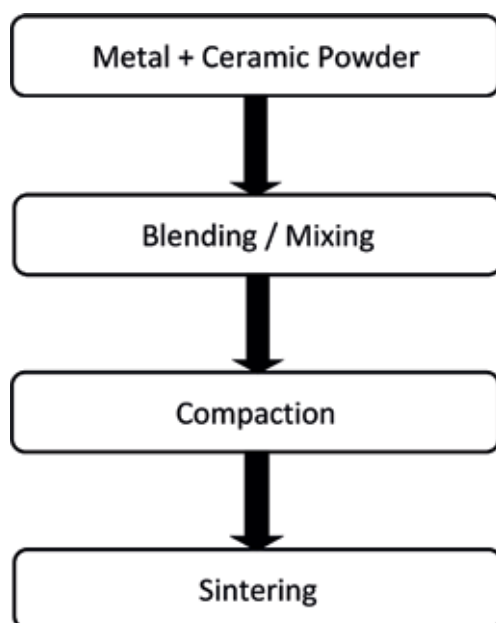


**Figure 5.**  
*Step in PM.*

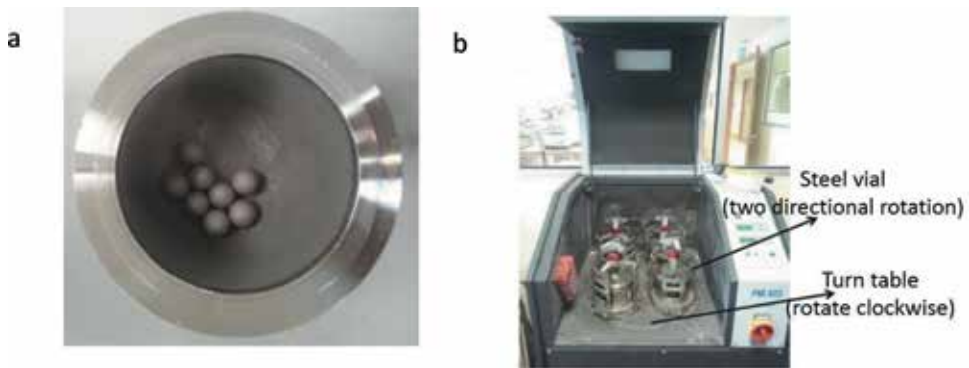


**Figure 6.**  
(a) Diagram shows the steel vial with steel balls and (b) planetary ball mill [2].

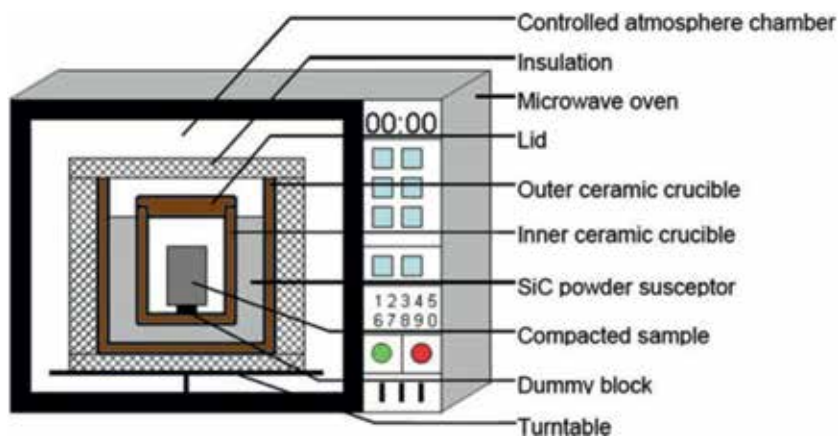


**Figure 7.**  
Hybrid microwave sintering setup [52].

Several magnesium-based alloys, conventional and nanocomposites (e.g. Mg/3wt%Al/0.1wt%GNP) have been synthesized using PM technique. Typical processing steps include blending or mechanical alloying the predetermined amounts of metal and ceramic powder with or without steel balls using a planetary ball mill at a speed of 200 rpm for 1 h. A typical planetary type ball mill setup is shown in **Figure 6**. The composite powders obtained from blending step are subsequently compacted using a 100 T hydraulic press to attain a billet of ~35 mm diameter and height of 40 mm. Compacted billets can be sintered using a conventional furnace or microwave based sintering. Heating time during microwave sintering is kept with 16 min. Conventional microwave 0.9 kW power and 2.45 GHz operating frequency can be used. The schematic diagram of microwave sintering set-up is shown in **Figure 7**.

### 2.1.7 Accumulative roll bonding

Accumulative roll bonding (ARB) is a solid-state severe plastic deformation technique used to produce layered composite stacked with either similar or dissimilar alloys sheet and reinforcements [61–64]. The final output of the ARB process depends on the process variables namely weight percent of the alloys and the reinforcement, number of rolling cycles and the temperature. The benefits of the process are grain refinement from fine to ultra-fine, fragmentation of reinforcement clusters and their subsequent uniform distribution. To realize best possible



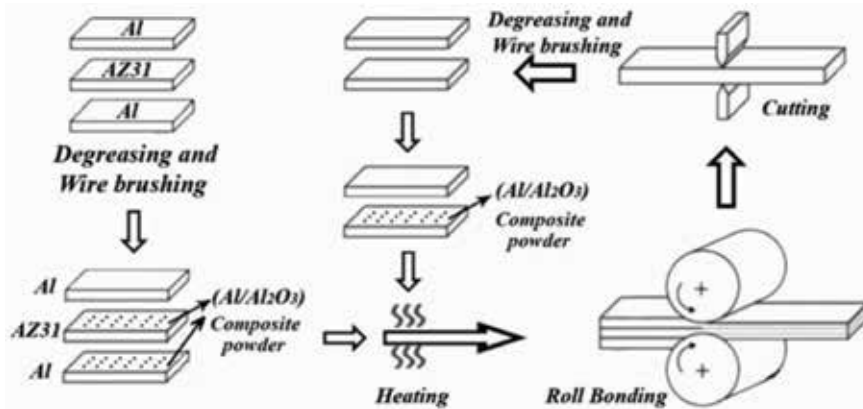


**Figure 8.**  
Steps in synthesizing nano-composites using ARB [61].

results, the sheets need to be pretreated by grinding and polishing for descaling oxides and to make friction free surface. Degassing process is also often used. The schematic setup of the ARB is shown in **Figure 8**.

Monolithic aluminum (Al) and AZ31 magnesium [61] strips of 1 and 0.5 mm thickness were cut to 150 × 50 mm rectangular strips. The strips were annealed at 400 °C for 2 h and furnace cooled near ambient temperature to soften the strips prior to rolling. The sheets were ground, polished, degassed and cleaned prior to rolling. In a steel vial Al and nano-alumina (<50 nm) powder were purged along with 0.5 and 1 mm in diameter steel balls. Milling of Al-alumina powder was conducted at 300 rpm and ball-to-powder ratio of 20:1 for six cycles, each of 45 min duration with a dwell time of 15 min to eliminate undesirable rise in temperature. The milled Al-alumina particles were uniformly spread between the strips for better wettability. The stacking was done as Al/AZ31/Al with reinforcement powder in between. The stack was fastened by copper wires to avoid slipping. The assembly was preheated in the temperature range of 300–350 °C for 15 min in an air furnace. 50% reduction was maintained at each rolling stage. Rolling was carried out for four times.

Accumulative roll bonding has yielded good combination of properties due to enhanced microstructural aspects and is investigated further for scaling up.

#### 2.1.8 Friction stir processing (FSP)

Friction stir processing is a solid-state plastic-deformation-based synthesis method (**Figure 9**). It can be used to build nano-composite layer/surface composite as well as bulk composites of limited thickness/dimensions. It often leads to uniform distribution of reinforcement and refined grain size [65–70]. The FSP process uses a shouldered rotating tool that pass over the matrix containing nano-ceramic particles. During the translational movement of tool, matrix get plastically deformed and reinforcement gets simultaneously incorporated in the matrix. The stirring action enables uniform distribution and refine grained structure of the fabricated composite.

The  $\alpha$ - $\text{Al}_2\text{O}_3$  nano-particle reinforced AZ31 composite [65] was fabricated using friction stir processing technique. The Mg rectangular plates of 600 × 100 × 10 mm were cut for preparing the composite. The ceramic particles were spread into a groove of width and depth 1.2 × 5 mm cut in the plates as shown in the **Figure 8**. Two types of shouldered tools were used to form the composite, one pin less shoulder and the other shoulder with a pin of 5 mm height

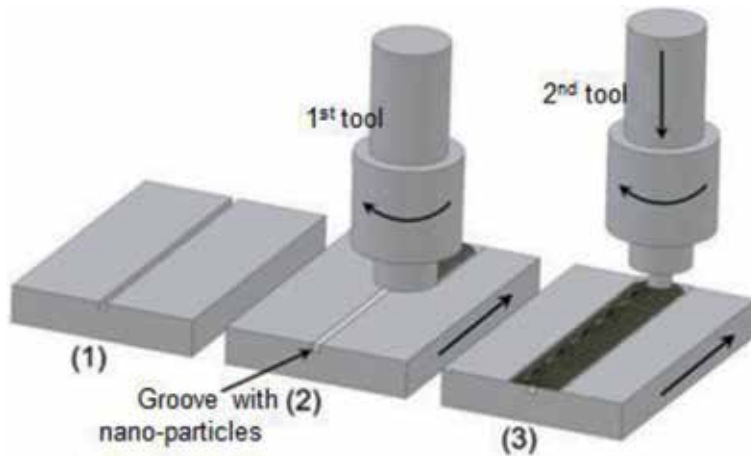


**Figure 9.** FSP fabrication stages from 1 to 3 for Mg nano-composite [67].

and diameter of 6 mm. The pin less tool was fed first to prevent the nano-phase getting distorted from the groove. The second tool with pin was then passed to complete the process. The tool rotation (800–1400 rpm) and the traverse speed (45 mm/min) were varied to obtain the desired strength and structure of the composite. Higher hardness was observed due to grain refinement at higher tool rotational speed.

## 2.2 Secondary processing methods

Secondary processing is essentially performed on primary processed composites to eliminate/minimize defects and microstructural irregularities to enhance mechanical properties such as strength, hardness etc. Secondary processing methods include bulk deformation process such as extrusion/rolling/friction stir processing and severe plastic deformation processing methods such as equal channel angular pressing (ECAP) and cyclic extrusion and compression (CEC).

### 2.2.1 Extrusion

The MMNC billet is stressed under high pressure ram inside a die which quantitatively reduces the irregularities like pores, cavity, voids and cracks formed earlier in primary processing methods. Normally carried above recrystallization temperature, the hot extrusion processes can be categorized into;

1. Forward or direct extrusion
2. Backward or indirect extrusion

The difference in the two method is the flow of billet direction. The billet extruded on the direction of the ram is direct extrusion while in the backward extrusion, the billet is extruded opposite to the direction of movement of ram. Typical forward extrusion process is shown in **Figure 10**. The key process parameters are extrusion ratio, temperature during extrusion and the speed of the ram. Extrusion ratio is the ratio between initial to the final cross section of the billet. The working temperature and environment should be optimally decided to eliminate oxidation during extrusion.

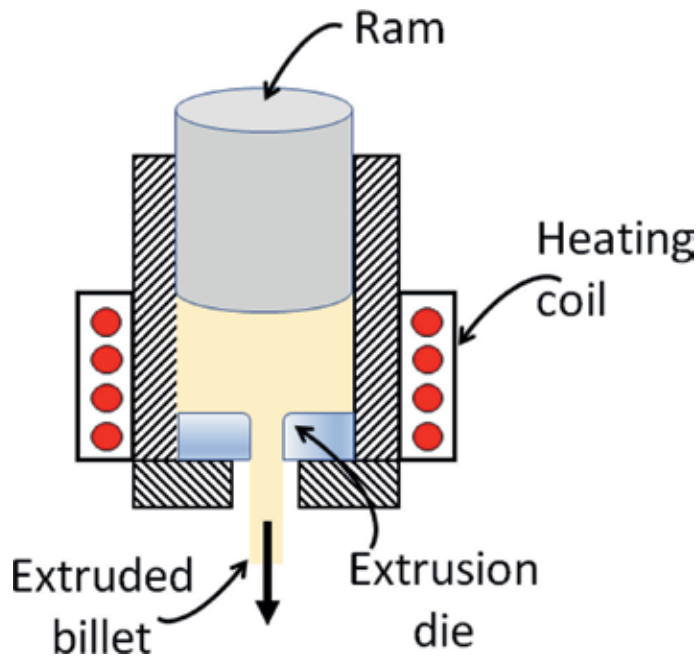


**Figure 10.**  
 Schematic representation of direct extrusion process.

### 2.2.2 Rolling

Rolling is a plastic deformation process in which the MMNCs are deformed by passing through set of high-pressure rolls. The MMNCs are deformed plastically by compressive stress and squeezing action between the rolls. The process enables the MMNCs to obtain fine grain microstructure and eliminates defects caused in the primary processing. The benefits include fine grain microstructure and enhanced mechanical properties of the material. The process parameters are percentage reduction, temperature and the number of passes to achieve the final thickness on the MMNCs. Rolling is also normally carried out a higher temperature to minimize the load required for plastic deformation.

### 2.2.3 Equal channel angular pressing (ECAP)

ECAP (**Figure 11**) is used to form ultrafine-grained (UFG) microstructure MMNCs. The MMNC billet is passed through two channelled die with identical cross section that intersect at an angle  $\Phi$  (channel intersection angle). During the process the billet undergoes severe plastic shear deformation (SPD) without altering the geometrical cross-section. The process is normally repeated for several passes in order to attain UFG structure. Different routes followed namely A, BA, BC and C as discussed elsewhere [71]. Previous researcher [71] reported that when  $\Phi$  is  $90^\circ$ , enhanced grain refinement is realized due to increase in the shear strain ( $\gamma$ ). The shear strain for the individual passes can be obtained by:

$$\gamma = 2 \cot\left(\frac{\Phi}{2}\right) \quad (3)$$

In an earlier research [16] conducted on Mg-9Al-1Si-1SiCn composite, ECAP was performed at a temperature of  $360^\circ\text{C}$ . Route BC was chosen with

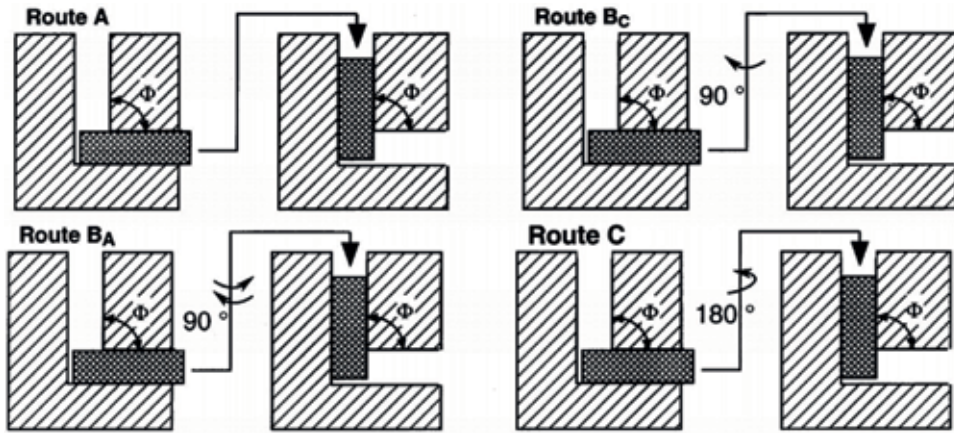


**Figure 11.**  
Schematic diagram of four ECAP routes [71].

ram speed of 2 mm/min. Homogenization heat treatment was carried prior to ECAP. Homogenized ECAP composite billet exhibited superior ductility and tensile strength.

#### 2.2.4 Cyclic extrusion and compression (CEC)

CEC is another type of SPD technique in which the MMNC ingot is passed through the annual die to attain a fine-grained microstructure shown in **Figure 12**. The fine-grained structure in the ingot is realized using optimal temperature and the number of reciprocating passes. A typical setup of the CEC is shown in the figure below.

AZ91D/SiCn nano-composite was fabricated with refined grain structure using CEC [72]. Fabrication using the CEC was performed by varying the operating temperature from 300 to 400 °C and up to eight passes were made. Superior hardness with refined grain structure were observed.

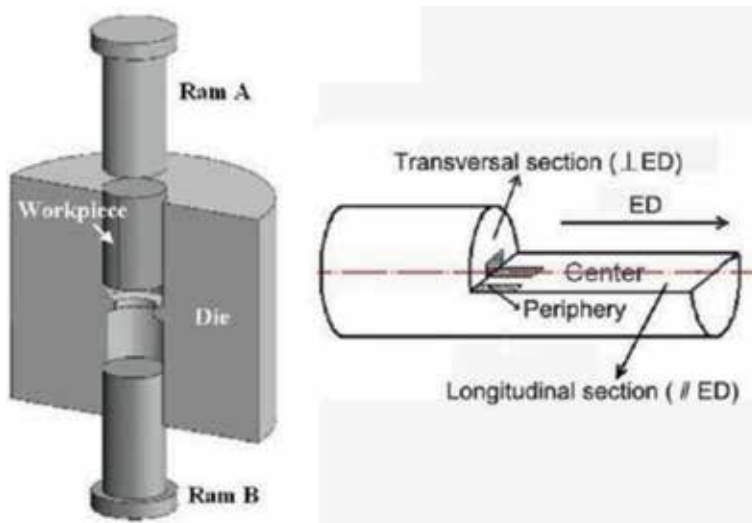


**Figure 12.**  
Schematic diagram of CEC setup [35].

### 3. Conclusion

Present chapter provides an insight into the magnesium nano-composites that are emerging as potential candidates in many weight-critical engineering applications ranging from aerospace, automotive to sport industries. Not only they are significantly lighter than aluminum and titanium, they can also be processed using both conventional and advanced processing methods. Stir casting is the most traditional high-volume production technique capable of generating a uniform dispersion of nano-particles in the magnesium matrix. An improvement using the ultrasonic cavitation as a mean to disperse the nano-reinforcement is already attempted with promising results. Furthermore, disintegrated melt deposition technique has proved to be the most effective one because of its capability to well disperse the nano-additives and refine the microstructure which results in excellent mechanical properties. DMD is also a scalable technique. A different approach to create magnesium based nano-composites employing the chemical reaction to form nano-intermetallics during the casting period is called as in-situ casting. A semi-solid casting technique called Rheocasting applied slurry characteristics to mix the nano-particles into the matrix. The magnesium nano-composites could also be processed using powder metallurgical methodology where the raw matrix material and reinforcements are pre-mixed in powder forms using ball milling followed by compaction and sintering. Other solid-state processing techniques such as accumulative roll bonding and friction stir processing have shown tremendous promise as well. This chapter also introduces conventional and advanced secondary processing techniques such as extrusion, rolling, equiaxed channel angular pressing, and cyclic extrusion and compression. The utilization of secondary processing techniques along with primary processing techniques can lead to enhanced microstructural properties that are key to improved mechanical performance and reliability.

#### Author details

Srinivasan Murugan<sup>1\*</sup>, Quy Bau Nguyen<sup>2</sup> and Manoj Gupta<sup>3</sup>


1 Dhofar University, Salalah, Oman

2 Charles Darwin University, Australia

3 National University of Singapore, Singapore

\*Address all correspondence to: [smurugan@du.edu.om](mailto:smurugan@du.edu.om)

#### IntechOpen

© 2019 The Author(s). Licensee IntechOpen. This chapter is distributed under the terms of the Creative Commons Attribution License (<http://creativecommons.org/licenses/by/3.0>), which permits unrestricted use, distribution, and reproduction in any medium, provided the original work is properly cited. 

## References

- [1] Zhang Z, Tremblay R, Dube D. Microstructure and mechanical properties of ZA104 (0.3-0.6 Ca) die-casting magnesium alloys. *Materials Science and Engineering A*. 2004;**385**:286-291. DOI: 10.1016/j.msea.2004.06.063
- [2] Gupta M, Meenashisundaram GK. *Insight into Designing Biocompatible Magnesium Alloys and Composites*. Singapore: Springer; 2015
- [3] Dieringa H, Hort N. Magnesium-based metal matrix nanocomposites—Processing and properties. In: *TMS Annual Meeting & Exhibition*. Cham: Springer; 2018. pp. 679-691. DOI: 10.1007/978-3-319-72526-0\_64
- [4] Ceschini L, Dahle A, Gupta M, Jarfors AE, Jayalakshmi S, Morri A, et al. *Aluminum and Magnesium Metal Matrix Nanocomposites*. Singapore: Springer; 2017
- [5] Habibnejad-Korayem M, Mahmudi R, Poole WJ. Enhanced properties of Mg-based nano-composites reinforced with Al<sub>2</sub>O<sub>3</sub> nano-particles. *Materials Science and Engineering A*. 2009;**519**:198-203. DOI: 10.1016/j.msea.2009.05.001
- [6] Huang SJ, Chen ZW. Grain refinement of AlNp/AZ91D magnesium metal-matrix composites. *Kovove Materialy Metallic Materials*. 2011;**49**:259-264. DOI: 10.4149/km 2011 4 259
- [7] Huang SJ, Lin PC, Aoh JN. Mechanical behavior enhancement of AM60/Al<sub>2</sub>O<sub>3</sub>p magnesium metal-matrix nanocomposites by ECAE. *Materials and Manufacturing Processes*. 2015;**30**:1272-1277. DOI: 10.1080/10426914.2014.880456
- [8] Huang SJ, Ho CH, Feldman Y, Tenne R. Advanced AZ31 Mg alloy composites reinforced by WS<sub>2</sub> nanotubes. *Journal of Alloys and Compounds*. 2016;**654**:15-22. DOI: 10.1016/j.jallcom.2015.09.066
- [9] Kumar S, Suman KN, Ravindra K, Poddar P, SB VS. Microstructure, mechanical response and fractography of AZ91E/Al<sub>2</sub>O<sub>3</sub> (p) nano composite fabricated by semi solid stir casting method. *Journal of Magnesium and Alloys*. 2017;**5**:48-55. DOI: 10.1016/j.jma.2016.11.006
- [10] Li Q, Rottmair CA, Singer RF. CNT reinforced light metal composites produced by melt stirring and by high pressure die casting. *Composites Science and Technology*. 2010;**70**:2242-2247. DOI: 10.1016/j.compscitech.2010.05.024
- [11] Liu W, Wang X, Hu X, Wu K, Zheng M. Effects of hot rolling on microstructure, macrotexture and mechanical properties of pre-extruded AZ31/SiC nanocomposite sheets. *Materials Science and Engineering A*. 2017;**683**:15-23. DOI: 10.1016/j.msea.2016.11.007
- [12] Matin A, Saniee FF, Abedi HR. Microstructure and mechanical properties of Mg/SiC and AZ80/SiC nano-composites fabricated through stir casting method. *Materials Science and Engineering A*. 2015;**625**:81-88. DOI: 10.1016/j.msea.2014.11.050
- [13] Radi Y, Mahmudi R. Effect of Al<sub>2</sub>O<sub>3</sub> nano-particles on the microstructural stability of AZ31 Mg alloy after equal channel angular pressing. *Materials Science and Engineering A*. 2010;**527**:2764-2771. DOI: 10.1016/j.msea.2010.01.029
- [14] Yuan QH, Fu DM, Zeng XS, Yong LI. Fabrication of carbon nanotube reinforced AZ91D composite with superior mechanical properties. *Transactions of Nonferrous Metals Society of China*. 2017;**27**:1716-1724. DOI: 10.1016/S1003-6326(17)60194-8

- [15] Zeng X, Zhou G, Xu Q, Xiong Y, Luo C, Wu J. A new technique for dispersion of carbon nanotube in a metal melt. *Materials Science and Engineering A*. 2010;**527**:5335-5340. DOI: 10.1016/j.msea.2010.05.005
- [16] Zhang S, Li M, Wang H, Cheng W, Lei W, Liu Y, et al. Microstructure and tensile properties of ECAPed Mg-9Al-1Si-1SiC composites: The influence of initial microstructures. *Materials*. 2018;**11**:136. DOI: 10.3390/ma11010136
- [17] Dieringa H. Processing of magnesium-based metal matrix nanocomposites by ultrasound-assisted particle dispersion: A review. *Meta*. 2018;**8**:431. DOI: 10.3390/met8060431
- [18] Bhingole PP, Chaudhari GP, Nath SK. Processing, microstructure and properties of ultrasonically processed in situ MgO–Al<sub>2</sub>O<sub>3</sub>–MgAl<sub>2</sub>O<sub>4</sub> dispersed magnesium alloy composites. *Composites Part A: Applied Science and Manufacturing*. 2014;**66**:209-217. DOI: 10.1016/j.compositesa.2014.08.001
- [19] De Cicco M, Konishi H, Cao G, Choi HS, Turng LS, Perepezko JH, et al. Strong, ductile magnesium-zinc nanocomposites. *Metallurgical and Materials Transactions A*. 2009;**40**:3038-3045. DOI: 10.1007/s11661-009-0013-0
- [20] Deng KK, Wu K, Wu YW, Nie KB, Zheng MY. Effect of submicron size SiC particulates on microstructure and mechanical properties of AZ91 magnesium matrix composites. *Journal of Alloys and Compounds*. 2010;**504**:542-547. DOI: 10.1016/j.jallcom.2010.05.159
- [21] Cao G, Choi H, Oportus J, Konishi H, Li X. Study on tensile properties and microstructure of cast AZ91D/AlN nanocomposites. *Materials Science and Engineering A*. 2008;**494**:127-131. DOI: 10.1016/j.msea.2008.04.070
- [22] Lan J, Yang Y, Li X. Microstructure and microhardness of SiC nanoparticles reinforced magnesium composites fabricated by ultrasonic method. *Materials Science and Engineering A*. 2004;**386**:284-290. DOI: 10.1016/j.msea.2004.07.024
- [23] Khandelwal A, Mani K, Srivastava N, Gupta R, Chaudhari GP. Mechanical behavior of AZ31/Al<sub>2</sub>O<sub>3</sub> magnesium alloy nanocomposites prepared using ultrasound assisted stir casting. *Composites Part B: Engineering*. 2017;**123**:64-73. DOI: 10.1016/j.compositesb.2017.05.007
- [24] Li CD, Wang XJ, Wu K, Liu WQ, Xiang SL, Ding C, et al. Distribution and integrity of carbon nanotubes in carbon nanotube/magnesium composites. *Journal of Alloys and Compounds*. 2014;**612**:330-336. DOI: 10.1016/j.jallcom.2014.05.153
- [25] Liu SY, Gao FP, Zhang QY, Xue ZH, Li WZ. Fabrication of carbon nanotubes reinforced AZ91D composites by ultrasonic processing. *Transactions of Nonferrous Metals Society of China*. 2010;**20**:1222-1227. DOI: 10.1016/S1003-6326(09)60282-X
- [26] Liu WQ, Hu XS, Wang XJ, Wu K, Zheng MY. Evolution of microstructure, texture and mechanical properties of SiC/AZ31 nanocomposite during hot rolling process. *Materials and Design*. 2016;**93**:194-202. DOI: 10.1016/j.matdes.2015.12.165
- [27] Nie KB, Wang XJ, Wu K, Xu L, Zheng MY, Hu XS. Processing, microstructure and mechanical properties of magnesium matrix nanocomposites fabricated by semisolid stirring assisted ultrasonic vibration. *Journal of Alloys and Compounds*. 2011;**509**:8664-8669. DOI: 10.1016/j.jallcom.2011.06.091
- [28] Shen J, Yin W, Wei Q, Li Y, Liu J, An L. Effect of ceramic nanoparticle

reinforcements on the quasistatic and dynamic mechanical properties of magnesium-based metal matrix composites. *Journal of Materials Research*. 2013;**28**:1835-1852. DOI: 10.1557/jmr.2013.16

[29] Shen MJ, Wang XJ, Ying T, Wu K, Song WJ. Characteristics and mechanical properties of magnesium matrix composites reinforced with micron/submicron/nano SiC particles. *Journal of Alloys and Compounds*. 2016;**686**:831-840

[30] Cao G, Konishi H, Li X. Mechanical properties and microstructure of SiC-reinforced Mg-(2, 4) Al-1Si nanocomposites fabricated by ultrasonic cavitation based solidification processing. *Materials Science and Engineering A*. 2008;**486**:357-362. DOI: 10.1016/j.msea.2007.09.054

[31] Dieringa H, Katsarou L, Buzolin R, Szakács G, Horstmann M, Wolff M, et al. Ultrasound assisted casting of an AM60 based metal matrix nanocomposite, its properties, and recyclability. *Meta*. 2017;**7**:388. DOI: 10.3390/met7100388

[32] Wang XJ, Wang NZ, Wang LY, Hu XS, Wu K, Wang YQ, et al. Processing, microstructure and mechanical properties of micro-SiC particles reinforced magnesium matrix composites fabricated by stir casting assisted by ultrasonic treatment processing. *Materials and Design*. 2014;**57**:638-645. DOI: 10.1016/j.matdes.2014.01.022

[33] Wang W, Wang H, Liu Y, Nie H, Cheng W. Effect of SiC nanoparticles addition on the microstructures and mechanical properties of ECAPed Mg9Al-1Si alloy. *Journal of Materials Research*. 2017;**32**:615-623. DOI: 10.1557/jmr.2016.514

[34] Zhang L, Wang Q, Liao W, Guo W, Li W, Jiang H, et al. Microstructure

and mechanical properties of the carbon nanotubes reinforced AZ91D magnesium matrix composites processed by cyclic extrusion and compression. *Materials Science and Engineering A*. 2017;**689**:427-434. DOI: 10.1016/j.msea.2017.02.076

[35] Zhang L, Wang Q, Liao W, Guo W, Ye B, Li W, et al. Effects of cyclic extrusion and compression on the microstructure and mechanical properties of AZ91D magnesium composites reinforced by SiC nanoparticles. *Materials Characterization*. 2017;**126**:17-27. DOI: 10.1016/j.matchar.2017.01.008

[36] Gupta M, Wong WL. Magnesium-based nanocomposites: Lightweight materials of the future. *Materials Characterization*. 2015;**105**:30-46. DOI: 10.1016/j.matchar.2015.04.015

[37] Meenashisundaram GK, Seetharaman S, Gupta M. Enhancing overall tensile and compressive response of pure Mg using nano-TiB<sub>2</sub> particulates. *Materials Characterization*. 2014;**94**:178-188. DOI: 10.1016/j.matchar.2014.05.021

[38] Paramsothy M, Chan J, Kwok R, Gupta M. The effective reinforcement of magnesium alloy ZK60A using Al<sub>2</sub>O<sub>3</sub> nanoparticles. *Journal of Nanoparticle Research*. 2011;**13**:4855. DOI: 10.1007/s11051-011-0464-2

[39] Tekumalla S, Bharadwaj S, Srivatsan TS, Gupta M. An engineered magnesium alloy nanocomposite: Mechanisms governing microstructural development and mechanical properties. In: *TMS Annual Meeting & Exhibition*. Cham: Springer; 2018. pp. 193-202. DOI: 10.1007/978-3-319-72853-7\_13

[40] Alam ME, Han S, Nguyen QB, Hamouda AM, Gupta M. Development of new magnesium based alloys and their nanocomposites. *Journal of Alloys and Compounds*. 2011;**509**:8522-8529. DOI: 10.1016/j.jallcom.2011.06.020



- [41] Nguyen QB, Gupta M. Enhancing compressive response of AZ31B using nano- $\text{Al}_2\text{O}_3$  and copper additions. *Journal of Alloys and Compounds*. 2010;**490**:382-387. DOI: 10.1016/j.jallcom.2009.09.188
- [42] Sankaranarayanan S, Nayak UP, Sabat RK, Suwas S, Almajid A, Gupta M. Nano-ZnO particle addition to monolithic magnesium for enhanced tensile and compressive response. *Journal of Alloys and Compounds*. 2014;**615**:211-219. DOI: 10.1016/j.jallcom.2014.06.163
- [43] Tekumalla S, Seetharaman S, Bau NQ, Wong WL, Goh CS, Shabadi R, et al. Influence of cerium on the deformation and corrosion of magnesium. *Journal of Engineering Materials and Technology*. 2016;**138**:031011. DOI: 10.1115/1.4033033
- [44] Nguyen QB, Sharon Nai ML, Nguyen AS, Seetharaman S, Wai Leong EW, Gupta M. Synthesis and properties of light weight magnesium-cenosphere composite. *Materials Science and Technology*. 2016;**32**:923-929. DOI: 10.1080/02670836.2015.1104017
- [45] Paramsothy M, Chan J, Kwok R, Gupta M. The overall effects of AlN nanoparticle addition to hybrid magnesium alloy AZ91/ZK60A. *Journal of Nanotechnology*. 2012;**2012**:1-8. DOI: 10.1155/2012/687306
- [46] Chelliah NM, Singh H, Raj R, Surappa MK. Processing, microstructural evolution and strength properties of in-situ magnesium matrix composites containing nano-sized polymer derived SiCNO particles. *Materials Science and Engineering A*. 2017;**685**:429-438. DOI: 10.1016/j.msea.2017.01.001
- [47] Lei T, Tang W, Cai SH, Feng FF, Li NF. On the corrosion behaviour of newly developed biodegradable Mg-based metal matrix composites produced by in situ reaction. *Corrosion Science*. 2012;**54**:270-277. DOI: 10.1016/j.corsci.2011.09.027
- [48] Muley SV, Singh SP, Sinha P, Bhingole PP, Chaudhari GP. Microstructural evolution in ultrasonically processed in situ AZ91 matrix composites and their mechanical and wear behavior. *Materials and Design*. 2014;**53**:475-481. DOI: 10.1016/j.matdes.2013.07.056
- [49] Sahoo BN, Panigrahi SK. Synthesis, characterization and mechanical properties of in-situ ( $\text{TiC-TiB}_2$ ) reinforced magnesium matrix composite. *Materials and Design*. 2016;**109**:300-313. DOI: 10.1016/j.matdes.2016.07.024
- [50] Sahoo BN, Panigrahi SK. A study on the combined effect of in-situ ( $\text{TiC-TiB}_2$ ) reinforcement and aging treatment on the yield asymmetry of magnesium matrix composite. *Journal of Alloys and Compounds*. 2018;**737**:575-589. DOI: 10.1016/j.jallcom.2017.12.027
- [51] Poddar P, Mukherjee S, Sahoo KL. The microstructure and mechanical properties of SiC reinforced magnesium based composites by rheocasting process. *Journal of Materials Engineering and Performance*. 2009;**18**:849. DOI: 10.1007/s11665-008-9334-1
- [52] Gupta M, Wong WL. Enhancing overall mechanical performance of metallic materials using two-directional microwave assisted rapid sintering. *Scripta Materialia*. 2005;**52**:479-483. DOI: 10.1016/j.scriptamat.2004.11.006
- [53] Hassan SF, Tun KS, Al-Aqeeli N, Gupta M. Effect of copper nanoparticle on the high-temperature tensile behavior of a Mg- $\text{Y}_2\text{O}_3$  nanocomposite. *Arabian Journal for Science and Engineering*. 2018;**43**:4803-4810. DOI: 10.1007/s13369-018-3134-1

- [54] Kumar P, Kujur M, Mallick A, Tun KS, Gupta M. Effect of graphene nanoplatelets on the mechanical properties of Mg/3wt% Al alloy-nanocomposite. In IOP Conference Series: Materials Science and Engineering 2018 (Vol. 346, No. 1, p. 012001). IOP Publishing. DOI: 10.1088/1757-899X/346/1/012001
- [55] Liu J, Suryanarayana C, Zhang M, Wang Y, Yang F, An L. Magnesium nanocomposites reinforced with a high volume fraction of SiC particulates. International Journal of Materials Research. 2017;**108**:848-856. DOI: 10.3139/146.111546
- [56] Rashad M, Pan F, Hu H, Asif M, Hussain S, She J. Enhanced tensile properties of magnesium composites reinforced with graphene nanoplatelets. Materials Science and Engineering A. 2015;**630**:36-44. DOI: 10.1016/j.msea.2015.02.002
- [57] Safari A, Mahmudi R. High temperature mechanical properties of an extruded Mg-TiO<sub>2</sub> nano-composite. Advanced Engineering Materials. 2015;**17**:1639-1644. DOI: 10.1002/adem.201500132
- [58] Wei TZ, Shamsuri SR, Yee CS, Rashid MW, Ahsan Q. Effect of sliding velocity on wear behavior of magnesium composite reinforced with SiC and MWCNT. Procedia Engineering. 2013;**68**:703-709. DOI: 10.1016/j.proeng.2013.12.242
- [59] Zhang T, Du S, Sun W, Zhang J, Niu L, Hua X. New practical method of homogeneous dispersion of multi-walled carbon nanotubes (MWCNTs) into Mg matrix composites. In IOP Conference Series: Materials Science and Engineering 2017 (Vol. 182, No. 1, p. 012028). IOP Publishing. DOI: 10.1088/1757-899X/182/1/012028
- [60] Tun KS, Wong WL, Nguyen QB, Gupta M. Tensile and compressive responses of ceramic and metallic nanoparticle reinforced Mg composites. Materials. 2013;**6**:1826-1839. DOI: 10.3390/ma6051826
- [61] Abbasi M, Sajjadi S. Manufacturing of Al-Al<sub>2</sub>O<sub>3</sub>-Mg multilayered nanocomposites by accumulative roll bonding process and study of its microstructure, tensile, and bending properties. Journal of Composite Materials. 2018;**52**:147-157. DOI: 10.1177/0021998317703693
- [62] Sabetghadam-Isfahani A, Zalaghi H, Hashempour S, Fattahi M, Amirkhanlou S, Fattahi Y. Fabrication and properties of ZrO<sub>2</sub>/AZ31 nanocomposite fillers of gas tungsten arc welding by accumulative roll bonding. Archives of Civil and Mechanical Engineering. 2016;**16**:397-402. DOI: 10.1016/j.acme.2016.02.005
- [63] Yoo SJ, Han SH, Kim WJ. Magnesium matrix composites fabricated by using accumulative roll bonding of magnesium sheets coated with carbon-nanotube-containing aluminum powders. Scripta Materialia. 2012;**67**:129-132. DOI: 10.1016/j.scriptamat.2012.03.040
- [64] Lv Z, Ren X, Wang W, Gao X, Li W. Microstructure and mechanical properties of Mg/2 wt.% SiCp nanocomposite fabricated by ARB process. Journal of Nanomaterials. 2016;**2016**:1-12. DOI: 10.1155/2016/6034790
- [65] Ahmadvani DM, Fedel M, Heydarzadeh Sohi A, Hanzaki Z, Deflorian F. Corrosion behavior of magnesium and magnesium-hydroxyapatite composite fabricated by friction stir processing in Dulbecco's phosphate buffered saline. Corrosion Science. 2016;**104**:319-329. DOI: 10.1016/j.corsci.2016.01.002
- [66] Asadi P, Givi MB, Abrinia K, Taherishargh M, Salekrostam R. Effects of SiC particle size and process parameters on the microstructure

and hardness of AZ91/SiC composite layer fabricated by FSP. *Journal of Materials Engineering and Performance*. 2011;**20**:1554-1562. DOI: 10.1007/s11665-011-9855-x

nanocomposites by cyclic extrusion compression. *Materials Science and Engineering A*. 2012;**556**:267-270. DOI: 10.1016/j.msea.2012.06.086

[67] Asadi P, Faraji G, Masoumi A, Givi MB. Experimental investigation of magnesium-base nanocomposite produced by friction stir processing: Effects of particle types and number of friction stir processing passes. *Metallurgical and Materials Transactions A*. 2011;**42**:2820-2832. DOI: 10.1007/s11661-011-0698-8

[68] Azizieh M, Kokabi AH, Abachi P. Effect of rotational speed and probe profile on microstructure and hardness of AZ31/Al<sub>2</sub>O<sub>3</sub> nanocomposites fabricated by friction stir processing. *Materials and Design*. 2011;**32**:2034-2041. DOI: 10.1016/j.matdes.2010.11.055

[69] Azizieh M, Larki AN, Tahmasebi M, Bavi M, Alizadeh E, Kim HS. Wear behavior of AZ31/Al<sub>2</sub>O<sub>3</sub> magnesium matrix surface nanocomposite fabricated via friction stir processing. *Journal of Materials Engineering and Performance*. 2018;**27**:2010-2017. DOI: 10.1007/s11665-018-3277-y

[70] Liang J, Li H, Qi L, Tian W, Li X, Chao X, et al. Fabrication and mechanical properties of CNTs/Mg composites prepared by combining friction stir processing and ultrasonic assisted extrusion. *Journal of Alloys and Compounds*. 2017;**728**:282-288. DOI: 10.1016/j.jallcom.2017.09.009

[71] Zhu YT, Lowe TC. Observations and issues on mechanisms of grain refinement during ECAP process. *Materials Science and Engineering A*. 2000;**291**:46-53. DOI: 10.1016/S0921-5093(00)00978-3

[72] Guo W, Wang Q, Ye B, Li X, Liu X, Zhou H. Microstructural refinement and homogenization of Mg-SiC



# Severely Plastic Deformed Magnesium Based Alloys

*Ramesh Kumar Subramanian, Arun Kumar Srirangan and SreeArravind Mani*

## Abstract

Magnesium can be replaced with materials which experience strain controlled fatigue in their respective applications. Still, there are infrequent predicaments with utilizing magnesium alloys, comprising lower strength, fatigue life, ductility, toughness, and creep resistant attributes correlate with aluminum alloys. Some recent studies have been affirming that through the severe plastic deformation process, particularly equal-channel angular pressing (ECAP) method promotes very significant ultra-grain refinement in bulk solids, which enhances the mechanical properties. ECAP with a 90° clockwise rotation around the billet axis between consecutive passes in route B<sub>C</sub> has improved the ductile characteristics with increased yield strength and rate of elongation which leads to a greater fatigue life because ultra-fine grain refinement can be able to resist the crack propagations. To attain the plasticity at higher temperature magnesium and its alloys are required to undergo extrusion operation before proceeding to the multiple pass ECAP at 200°C because the magnesium alloys exhibit a limited number of slip systems due to its hexagonal crystal structure.

**Keywords:** magnesium, severe plastic deformation, ECAP, ultra-fine grains, texture

## 1. Introduction

In today's engineering world, light-weight materials have gained much attention because of demand in low-cost production and increasing efficiency through weight reduction. Correspondingly, Magnesium is one of the materials which attributed in the lightweight material category after aluminum and its alloys. Magnesium and its alloys have some unique application in aerospace and other engineering sectors. But due to some characteristics regarding the manufacturing process such as complex in forming the components and other cold working processes [1]. Particularly in Biomedical application, magnesium has some restriction since Mg dissolves in the body fluid during the restorative process, so degradation of magnesium has to be controlled [2]. One is the low mechanical properties comparing with the bioinert titanium alloys, which makes their application limited in load-bearing implants. Another one is the fast degradation behavior, which involves the gas cavity and high alkaline microenvironment around the implants leading to a poor osteointegration. The mechanical processing of magnesium alloy at elevated temperature influences the grain distribution.

Normally a combination of fine grain structure and coarse grain structure are formed through the various forming operation of wrought materials, and homogeneous grain structures obtained by the cast formed materials [3]. During

cold working, the fine grain formed along with the boundaries in the magnesium wrought materials which through the dynamic recrystallization and the distribution is multi-modal [4]. Normally area of the cross section has been reduced through the total plastic deformation method at certain temperature range. Consequently, the methods mentioned above are not having enough capacity to form homogeneous grain refinement at the initial structure and make the grain structure distribution the multimodal phase [5].

For the last few years, the development of plastic deformation technology, which includes the equal channel angular pressing (ECAP) is emerging [6]. The limitation in the plastic deformation of magnesium alloys will neglect through the SPD technique, so severe plastic deformation of magnesium and its alloys initiate the probability for manufacturing the ultrafine grain materials along with the increased mechanical properties and additionally the superplastic capabilities also experienced by the formed material [7].

Towards the application, ECAP paved a path for refinement of grains in the lightweight materials, particularly in concern aluminum and magnesium alloys. In concern with f.c.c metals, misorientation in the low angles boundaries and alignment of the elongated subgrains in parallel to the primary slip will occur when the sample subjected to severe plastic deformation [8, 9]. Followed by the first pass, the upcoming passes designed to induce further refinement of grains and rearrangement consistent with the dislocation theory for low energy structure [10, 11] after the multiple passes in the ECAP, a set of equiaxial grains which in different angles. The structure changes have been accounted in many metals having f.c.c arrangement, which also constitutes aluminum [12]. On the contrary, by using the ECAP process, UFG can be obtained from the magnesium alloys, and grains get refined by the subsequent passes [13].

During the ECAP process of the magnesium and its alloys, grain refinement depends on the number of passes, channel angle, die angle, and the initial grain structure before to the ECAP. By varying the various parameters of the ECAP process, including the temperature, Mg will exhibit diverse morphology such as grain orientation, distribution, size in multimodal type after SPD [12, 13]. Many studies focused on analyzing the microstructure and the mechanical properties after ECAP processing.

As explained, the pattern specified for the grain refinement channels towards a usual perception of the several articles resembling in the research literature and lead to understanding the ability for the further structure of grain formed under the various condition during SPD of magnesium alloys. In magnesium alloys, grain refinement defined in a simple way [14]. This statement is crucial for highlighting, though, that exact grain refinement mechanism elaborated which authorizes various structure formations based on the experimental circumstances including those primary inferences towards maximum processing steps in SPD of magnesium alloys. Different methods regarding severe plastic deformation consistently engage in developing the process and regarding the nanostructure formation in the samples [15].

Under the certain experimental circumstance getting the ultrafine-grained structure along with predominating boundaries oriented in the high degree of angle and it will be varied according to materials. Furthermore, the nanostructure formation in the alloy during the ECAP process is stable in the entire uni, which required for providing durable characteristics for the metals [7, 13]. Followed by, ensuring the ECAP processed samples for mechanical damages or any penetrated cracks in the material. The other methods of SPD will not meet the requirements as above, such as drawing, hot extrusion, and rolling. Nanostructure formation in the samples is only possible with the mechanical deformations at relatively low temperature as well as optimal parameters for material processing [16].

## 2. An examination of reports of microstructures produced in Mg and magnesium alloys

To make a competent design, it is essential to analyze different grain structures of magnesium and its alloys, which processed through the ECAP [17]. An initial documented reports organized, and general review presented in **Table 1** for pure magnesium and magnesium alloys, which processed through ECAP.

The outcome in the given **Table 1** indicates the utilization of an ECAP die set up with the 90 internal channel angle, operating with and without back pressure, and the expected outcomes notified in the column number six of **Table 1**. From the table, A and B represent the heterogeneous and homogeneous grain structure,

Alloy	Initial grain size (μm)	Final grain size (μm)	Inter-mediate structure	Structure after multiple passes	Additional information	References
AZ31	48.3	2.5	A	B	—	[18]
AZ31	48.1	1.4	B	B	U = 100 L	[19]
AZ31	2.5	0.7	—	B	U = 110 L	[20]
AZ31	15–22	1	A	B	BP-ECAP (423 K)	[21]
AZ31	5–30	1.9	A	B	Pre-deformed by extrusion	[22]
AZ31	5–30	2.2	A	B	U = 110 L	[23]
AZ31	450	1–3	A	A		[24]
AZ31	20	1–2	—	B	Pre-deformed by hot-rolling	[25]
AZ31	10–20	3.0	A	B		[26]
AZ31	10	3.2	—	B	Pre-deformed by rolling	[27]
AZ31	7–20	2	A	B	Route A	[28]
AZ31	15–22	0.9	A	B	BP-ECAP	[29]
AZ31	28	8	A	—	One pass of BP-ECAP	[30]
AZ61	16	0.62	B	B	Pre-deformed by extrusion	[31]
AZ91		0.5	—	B	Pre-deformed by extrusion	[32]
AZ91	40	1.2	A	B	Route C	[33]
Mg (pure)	400	120	—	B	—	[34]
Mg (pure)	200	20	A	A	—	[35]
Mg (pure)	900	70	A	B	—	[36]
Mg–0.9% Al	100	17	—	B	—	[34]

**Table 1.** Comparison of experiments conducted on pure magnesium and a range of magnesium alloy.

respectively. BP indicates the back pressure, and U is for the channel angle within the die. Then ECAP routes defined by route A indicate that ECAP processed without any specimen rotation in-between the two passes, B<sub>A</sub> indicates the specimen rotation of 90° in the alternative direction in-between the passes and C denotes the rotation of 180° in-between the passes.

From **Table 1**, we can observe that materials represented in the first column, the grain sizes of the material before and after ECAP provided in the following columns. Then followed by that intermediate stage in the ECAP process is given in the fourth column and the fifth column provided with the additional information regarding the total number of passes. Finally, the references provided in the last column. Additionally, the structure of the grain after processing with the ECAP have given in the notation of Bi-m and Trim to indicate the grain distribution, whether it is tri-modal or Bimodal correspondingly.

From the interference of **Table 1** observation of the distribution of the heterogeneous grain size has done after many passes, particularly while the grain size is large at the initial stage. Certainly, grains were heterogeneous at the initial stage in which the size of the grain ranges from the minimum 45.5 μm for magnesium alloy ZK60 to a higher grain size range of 640 μm magnesium alloy AZ31. From the observation made from the existing investigation, with the minimum number of ECAP passes, the homogeneous grain arrays can obtain with the average grain size of ~40 μm. The high-temperature ECAP processed help to form the homogenization: for instance, the grain size with bi-modal configuration with homogeneity attained with six ECAP passes at the temperature of 423 K in the magnesium AZ31 alloy. In Magnesium-Zn alloy bi-modal distribution is obtained in grain size in which initially the fine and coarse grains have found.

From **Table 1**, there were two significant limitations found; one is the results illustrated that by considering the process limitations, the initial structure might exhibit the homogenous distribution, tri-modal or bi-modal grain size distribution. And another observed one is when the grain size is larger, or it formed in coarse then the bi-modal distribution in the grain size is preferred. These were the two important consideration which made based on the grain structure.

### **3. A model for grain refinement in Mg and magnesium alloys processed by ECAP**

From **Figure 1**, which shows the patterned design model which created based on the grain structure formation of ECAP processed of magnesium alloys. The design raised based on the assumption of grain size and distribution on the initial stage and mechanism which proposed earlier regarding the grain structure.

The various grain structure at the initial stage, which is before the ECAP is shown in **Figure 1a, d, g, and j**. In which  $d_c$ , the critical grain size integrates with the concept which effectively reduced the size, which initiates the nucleation with proper homogenization during the processing of the materials. The structure of the grain and its refinement process is given below.

Particularly, the initial structure of the coarse grain at the initial stage with the size,  $d$  and the grain size,  $d$ , is larger than  $d_c$  ( $d \gg d_c$ ), which is the critical grain size which shown in **Figure 1a, d, and g**. From **Figure 1j**,  $d < d_c$ , which means the initial grain structure is granular than the critical size. In certain, the grains which attained homogenous nucleation in which entire grain structure is non-basal slips. Furthermore a complete has been yet to be considered to improve the standard of the processing parameters, and it is important to expect that it will rely on kind of alloy and temperature for processing of ECAP and present investigations show that back pressure also a dependent factor for the grain structure.



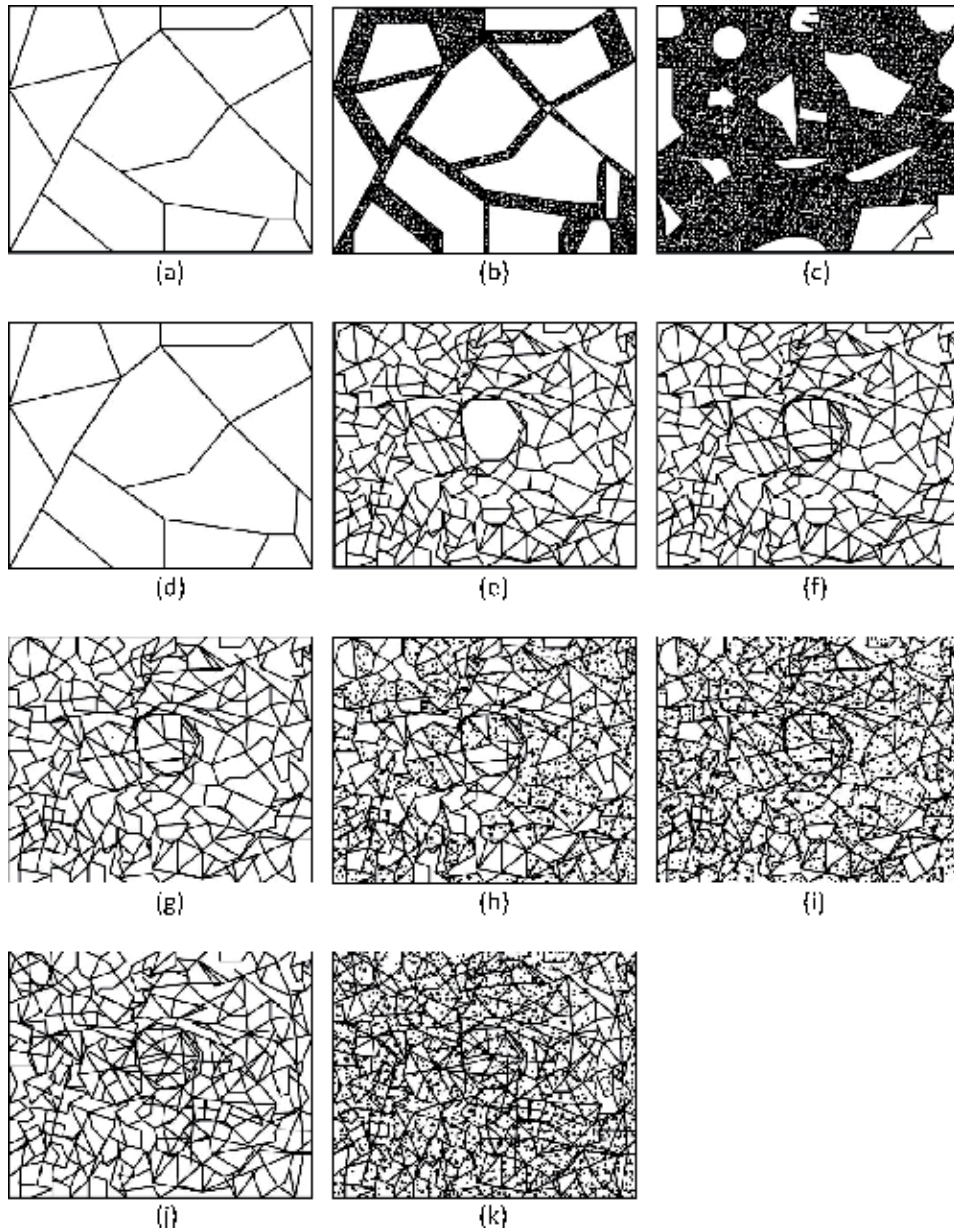


**Figure 1.** Patterned design on the refinement of grain of the ECAP processed Mg alloys. (a), (d), (g), (j) are the initial grain structure whose grain size can be termed as  $d \gg dc$ ,  $d > dc$ ,  $d \approx dc$  and  $dc$  respectively. (b), (e) and (h) are the intermediate structure at the shear zone during the ECAP. (c), (f), (i) and (k) are the final structure after the pass [8].

From the second column of **Figure 1**, which illustrates the grain structure formed after one pass. Followed by that third column indicated the grain structure formed after more than one number of passes. Where the structure of the initial size of the grain is comparably larger than critical diameter  $dc$ , as shown in the first column of **Figure 1**, the grain structure develops in the initial pass, such as the bimodal or multimodal distribution of the grain as shown in the second column of **Figure 1**. Subsequently, the region occupied by the extended cores of the grains at the initial stage and by the grains which newly formed after refinement have significantly relied on the initial size of the grains which observed during the analysis of

**Figure 1.** For a better explanation, differentiation among the cores of the initial grains which are usually larger which exist even after one pass of ECAP, the core regions mentioned above illustrated in the second column and the third column of **Figure 1**, in particular recently refined grains which indicated in the dotted region.

In **Figure 1**, the first row illustrates the condition of the grain structure at initial stage which is particularly coarse, because of that even after the one pass of ECAP the initial grains last and hold an extended region which shown in **Figure 1b** and the same grains may get unrefined until multiple passes which are shown in **Figure 1c**. From **Figure 1b**, it can be observed that twinning takes place across the larger grains, so it leads to refinement of grain accompanying with the twinning features. The condition where the critical size of the grain is very smaller than the initial grain size which made bi-modal or multi-modal grain distribution possible which continues even after the multiple passes of ECAP which shown in **Figure 1c**.

In defining the features of the newly developed grains, it is important to explain whether the grain size distribution is multimodal or homogeneous. The  $d_c$  grain size variations observed from the first two rows in **Figure 1** were the result of variation in the processing parameters particularly the temperature through the initial structure is similar which illustrated in **Figure 1a** and **d**. The fractional volume of the newly developed grains after one pass is small when compared to the initial structure because it is too coarse which observed from the first row of **Figure 1** and this will be the cause for the formation of bimodal and multimodal distribution among the grain size after the multi passes of ECAP. Subsequently, the same initial structure subjected to the one pass of ECAP with different processing conditions such as lower strain rate and elevated temperature which resulted in the formation of new grains and occupy the extended region which illustrated in **Figure 1e** and also after multiple passes of ECAP the sample exhibits uniform grain structure as illustrated in **Figure 1f**.

After a single pass of ECAP, the grain size distribution becomes bimodal or multimodal by forming reasonably fine structures grains. But the existing grains or grain which not affected by the pass occupied lesser fraction area that the newly formed ones which illustrated in **Figure 1g**. **Figure 1i** shows, by multiple ECAP, passes, the grains get refined and resulted in the homogeneous distribution.

By having the initial grain size as smaller than the critical grain diameter as shown in **Figure 1j**, the homogeneous array distribution achieved through the single pass of ECAP as illustrated in **Figure 1i** and subsequently after many passes homogeneity remains the same.

From the mode, it concluded that bi- and multi-modal grain size distributions which formed through the ECAP were transitional and the distribution of the grains gets altered as ECAP passes the increase.

Spitale et al. processed ECAP in minimal temperature, which is about 250°C with the channel angle of 90° and with 45° of the radius of curvature. The plunger speed for the process is 0.1 mm/s. They observed the evolution of grain structure at different location of the deformation zone. **Figure 2** shows the appearance of the structure entering the deformation zone [37].

The initial structure of the grain exists with the witness of twinning action. Grain boundaries observed with the serration like features. Grains with fine size within the range of 20  $\mu\text{m}$  have witnessed within the region of grain boundaries and twins, which is developed from the initial grain structure, as shown in **Figure 3**. Apart from the certain limits from the grain boundaries and twins, fine grains were not witnessed with then fine grains.

From **Figure 4**, it witnessed that a large area occupied by the fine grains. The fine grains average size is around  $\sim 15 \mu\text{m}$ , which observed from the deformation zone. The fine grain distribution followed the necklace pattern which exists around the area of unrefined grain ( $>100 \mu\text{m}$ ).

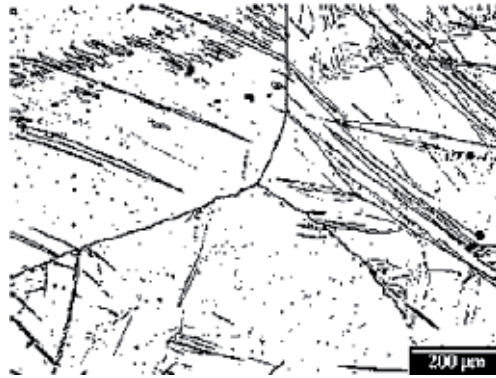


**Figure 2.**  
*The grain structure in the region of deformation [37].*



**Figure 3.**  
*Structure of the grain inside the region of deformation [37].*

#### 4. Improved processing routes for ECAP with magnesium alloys

The processing routes influenced the final structure of the grain, failure of billet, and shear localization effect through the grain structure size distribution and refinement mechanism of the magnesium and its alloys. The formation of the shear bands is due to the concentration of the thin layer which belongs to the newly formed grains along with the existing grain boundaries. This shear concentration occurs in a layer due to the nearby regions shear, and it develops damage pile; thus, the failure in the billet takes place. The rise in the initial grain coarse volume leads to the rise in the shear amount, which is in the shear band. The possibilities of the localization of the shear are higher, which is shown in the first row of **Figure 1** successively the growth shown in below rows. This decision is in Correspond with the failure of the coarse grain structure in the magnesium and its alloys.

To rectify the issues in the ECAP process of the magnesium and its alloys, some measures have been improvised and designed such as the processing route along with temperature, die angle and the back pressure range and its usage. To bring down the tenor for shear localization the grain cores along with the boundary extents have to reduce. Thus a primary step of extrusion is made to refine the microstructure which can change the initial grain structure as illustrated as **Figure 1** an into refined grain structure like **Figure 1g** or **j**. As shown in the second row of **Figure 1a**, the grain refinement sequence of the newly formed grains can alter through the rise in the processing temperature. This alteration in the ECAP process

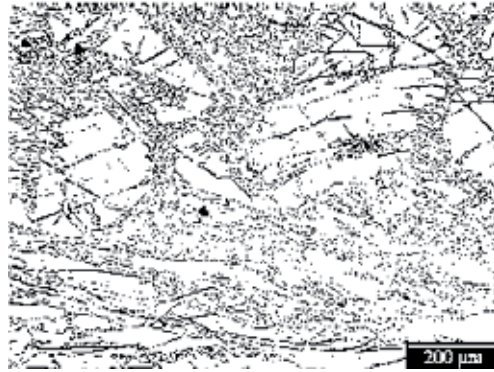


**Figure 4.**  
*Grain structure at the end of the deformation zone [37].*

can provide a huge volume of formed grains and reduced tensor for localization of shear [14, 24–27, 29]. The accumulation of the damage and the shear bands strain have reduced through the increase in the die angle during the ECAP process. The billet cracking which normally caused by the damage accumulation and the additional grain refinement can achieve by using the back-pressure during the ECAP process of the magnesium alloys.

An alternate method is by subjecting the magnesium alloys to the multiple ECAP as initial pass in the elevated temperature, and the sequent passes in lower temperature can help to achieve a fine-grain structure with the homogeneous distribution. This process resembles the technique which follows the extrusion process before the ECAP [31].

The customizing of the grain size distribution in the magnesium alloys is associated with the grain structure refinement mechanism of the alloys, which processed through the ECAP process. By changing the ECAP process, it is desirable to alter or control the grain structure and its fine or coarse refinement structure. To increase the certain mechanical properties of the material such as ductility and strength concept of manipulating the material grain boundary and grain refinement was introduced many years ago in the basis of the grain boundary engineering, the same concept have been followed and approached in the process of ECAP. The recent investigations showed that through the ECAP process, the alteration of the grains structure and its distribution achieved in the selected materials. This merit region in the process mentioned above is, for instance, developing a grain distribution in the bimodal configuration in nanostructured Cu, a combination of enhanced ductility and sufficient strength showed up during the tensile testing at ambient temperature which presented in research work. To obtain the sufficient strength and altered elongated grains to increase the stability during the tensile deformation, ECAP method paves the way for these through the forming ultrafine grains and altering the grain size distribution. Among the Grain size distribution, the bimodal configuration considered as the efficient thing for rising the ductility characteristics during the cyclic loading and deformation which assure mechanical properties can improve through the grain size engineering [23–27].

## **5. Effect of texture**

The influence of texture is not straightly integrated with any developed model for the refinement of the grain structure. Unless the developed modal is expected to be effective for ECAP processing route and initial texture. This typical thing

supposed due to the forming mechanism of the grain structure along with the grain boundaries has witnessed in the magnesium and its alloys which are having the distinctive initial structures while processing in the various temperature range where ECAP is typically carried out [17]. With the uniform procedure, a recent research work analyzed the texture of magnesium AZ31 which processed through the rolling process and ECAP process and they concluded that texture did not influence the size of the grain which formed after the process meanwhile texture influences the chance of formation of new grains and deformation amount which needed to achieve the deformation.

With the recent proposed modal of ECAP, the progression in the structure of the grain refinement mechanism is witnessed [29]. The bimodal distribution of grain structure observed due to the fine grain refinement and grain nucleate around the boundaries of the grain and twins in the presence of area which does not get affected by the process. A research work [8] provides a technique in which grain which subjected to the recrystallization is nucleate throughout the existing grains in the materials and progress until the structure reaches the homogenous structure equiaxial. The variation among the grain structure refinement modal relies upon the region of nucleation, which tends to form the new grain and feasibility of forming the heterogeneous distribution of grains. Some research delivered that heterogeneous grain size distribution in the magnesium and its alloys.

Because of the coarse grains at the initial stage, the predicted criteria from the developed grain refinement model is getting disapproved with the homogeneous distribution of grain sizes. Possibly grain growth and altered grain structure had observed in the material after subjecting it to the complete ECAP process. In the different stages of the grain refinement, fine grains get nucleated throughout the existing grains and in the region of twin boundaries which happened as expected by the grain structure refinement modal which leads to the distribution of grain size in a heterogeneous manner. The temperature for the intermediate process is likely to prevent the growth of grain and influenced the grain structure to form the bimodal distribution, which witnessed after the ECAP process.

## 6. Effect of mechanical behavior

The maximum tensile strength is recorded through the compressive tests and in various ways as possible for the material which subjected for three passes of ECAP process which given in **Figure 5**. The data of the received material included for better understanding [30]. It witnessed that the ECAP processed specimen shows elevated flow stress in multiple directions when compared with processed ones.

The material which undergone the ECAP process display an improved yield and maximum yield stress along with improved behavior in the work hardening towards the different compression direction. Significantly the ECAP processed material which tested along the direction of the Y-axis which is perpendicular to the die channel of the ECAP setup shows a concave up like feature with the strain range of 0.02–0.05. Another major witness is that processed sample demonstrates a constant hardening strain range from 0.01 to 0.03 towards the direction of Z-axis and in the direction of X axis it shows 0.01–0.06 in which the hardening rate is slightly get decreased from the initial stage. The processed material showed up a rise in hardening rate in the range of 0.015–0.3045 in the direction of Y-axis.

From the above results, it is clear that ECAP processing ensures the mechanical anisotropy behavior of the commercially pure Magnesium. The appearance of twinning action in the material during the compression test leads to the anisotropy. The incident of increased hardening rate is clearly because of the twinning action

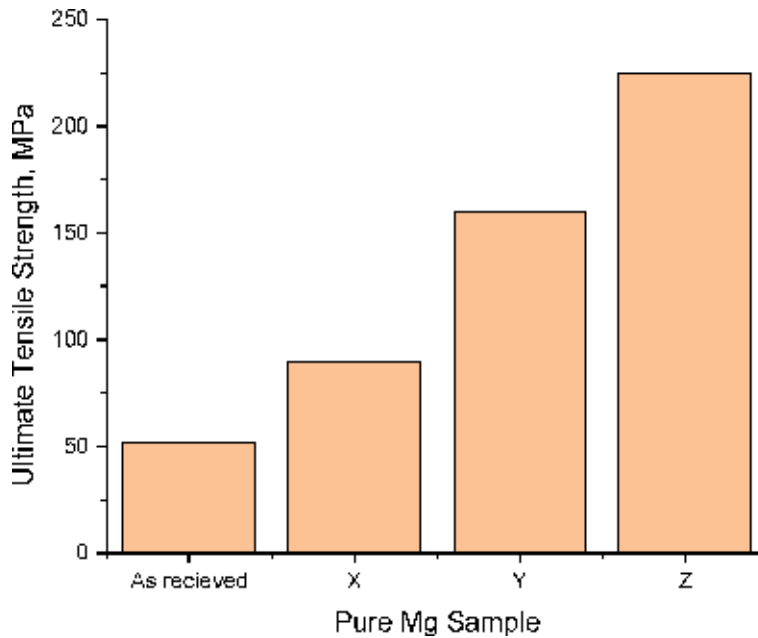


**Figure 5.** Ultimate tensile strength obtained for the CP-Mg before and after ECAP processing [30].

which occurred in the direction of Y-axis. Furthermore, the same twinning action indicated in the ECAP processed AZ31 alloy during the compressive test along the direction of the y-axis, which ensured through the microscopic examination. Along with that observation notable amount of twins were witnessed in the magnesium alloy after subjecting it to the strain of only 0.04 (in approx.) in the compressive test along the direction of Y-axis. The twins obtained after a certain level of strain in the corresponding direction was notably lower. Finally, the outcomes represent that after ECAP processing of commercially pure magnesium, the material shows an improved anisotropic behavior and notably twinning action also takes place while the material compressed in the direction of the Y-axis which is perpendicular to the die channel angle. The tensile characteristics of the rolled magnesium are in the good range and lowered elongation when compared to the ECAP processed commercially pure magnesium. These factors indicate that ECAP processing slightly reduces the yield stress and improves the ductile characteristics of the material. And also fine grain refinement was witnessed through the microstructural study of the ECAP processed Magnesium. Thus, the decreased yield stress after the rolling process, along with ECAP contribute to the texture effect of the magnesium.

## 7. Summary

Magnesium has plenty of tones and choice when equaled to the other metals or nonmetals which have utilized under the category of lightweight materials in automotive, aerospace and biomedical application. Certain advancements are transpiring in magnesium development, and that will engage a fine pathway to the prospect. Among the Severe Plastic deformation (SPD), one of its type Equal Channel Angular Pressing (ECAP) emerged as the technique which can be able to extend the magnesium alloys to the vast application. Among the science group, there is mindfulness about to witness the transcendent application of magnesium and its alloys. Furthermore, enough research and the experimental establishment is

needed for the unique evolution of deformation behavior of the magnesium alloys to achieve aspired microstructures which influence the mechanical properties plus fine shapes for avoiding post processes and further greater transformations of the phase which compromise to permit improvement of magnesium alloys. This very low density concerning magnesium and its alloy collectively among attractive characteristics such as castability is traversing to extended transportation business. The progressed application can begin from an expanded design along with many perceptions of the basic features of magnesium behavior and also the rise of cost-affordable magnesium alloys.

## Acknowledgements


This work was supported by “Research and Modernization fund, SASTRA University” grant number R&M/0035/SoME-008/2015-16. The authors thank SASTRA Deemed University for their financial assistance.

## Author details

Ramesh Kumar Subramanian\*, Arun Kumar Srirangan and SreeAravind Mani  
School of Mechanical Engineering, SASTRA Deemed to be University, Thanjavur,  
Tamil Nadu, India

\*Address all correspondence to: [rameshkumar@mech.sastra.edu](mailto:rameshkumar@mech.sastra.edu)

## IntechOpen

© 2019 The Author(s). Licensee IntechOpen. This chapter is distributed under the terms of the Creative Commons Attribution License (<http://creativecommons.org/licenses/by/3.0>), which permits unrestricted use, distribution, and reproduction in any medium, provided the original work is properly cited. 

## References

- [1] Monteiro WA, Buso SJ, Da LV. Application of magnesium alloys in transport. In: *New Features on Magnesium Alloys*. Rijeka, Croatia: InTech. pp. 1-15. DOI: 10.5772/48273
- [2] Sezer N, Evis Z, Kayhan SM, et al. Review of magnesium-based biomaterials and their applications. *Journal of Magnesium and Alloys*. 2018;**6**:23-43. DOI: 10.1016/j.jma.2018.02.003
- [3] Luo AA. Magnesium casting technology for structural applications. *Journal of Magnesium and Alloys*. 2013;**1**:2-22. DOI: 10.1016/J.JMA.2013.02.002
- [4] Kaibyshev R. Dynamic recrystallization in magnesium alloys. In: *Advances in Wrought Magnesium Alloys*. Oxford, UK: Woodhead Publishing; 2012. pp. 186-225. DOI: 10.1533/9780857093844.1.186
- [5] Mendis CL, Hono K. Understanding precipitation processes in magnesium alloys. In: *Fundamentals of Magnesium Alloy Metallurgy*. Oxford, UK: Elsevier; 2013. pp. 125-151. DOI: 10.1533/9780857097293.125
- [6] Valiev RZ, Langdon TG. Principles of equal-channel angular pressing as a processing tool for grain refinement. *Progress in Materials Science*. 2006;**51**:881-981. DOI: 10.1016/J.PMATSCI.2006.02.003
- [7] Zhou P, Wang H, Nie H, et al. Effect of ECAP temperature on precipitation and strengthening mechanisms of Mg-9Al-1Si alloys. *Journal of Materials Research*. 2018;**33**:1822-1829. DOI: 10.1557/jmr.2018.137
- [8] Langdon TG. The principles of grain refinement in equal-channel angular pressing. *Materials Science and Engineering: A*. 2007;**462**:3-11. DOI: 10.1016/J.MSEA.2006.02.473
- [9] Xu C, Furukawa M, Horita Z, et al. The evolution of homogeneity and grain refinement during equal-channel angular pressing: A model for grain refinement in ECAP. *Materials Science and Engineering: A*. 2005;**398**:66-76. DOI: 10.1016/J.MSEA.2005.03.083
- [10] Kuhlmann-Wilsdorf D. Theory of plastic deformation: Properties of low energy dislocation structures. *Materials Science and Engineering: A*. 1989;**113**:1-41. DOI: 10.1016/0921-5093(89)90290-6
- [11] Kuhlmann-Wilsdorf D. High-strain dislocation patterning, texture formation and shear banding of wavy glide materials in the LEDS theory. *Scripta Materialia*. 1997;**36**:173-181. DOI: 10.1016/S1359-6462(96)00347-8
- [12] Kawasaki M, Horita Z, Langdon TG. Microstructural evolution in high purity aluminum processed by ECAP. *Materials Science and Engineering: A*. 2009;**524**:143-150. DOI: 10.1016/J.MSEA.2009.06.032
- [13] Stráská J, Janeček M, Čížek J, et al. Microstructure stability of ultra-fine grained magnesium alloy AZ31 processed by extrusion and equal-channel angular pressing (EX-ECAP). *Materials Characterization*. 2014;**94**:69-79. DOI: 10.1016/J.MATCHAR.2014.05.013
- [14] Figueiredo RB, Langdon TG. Principles of grain refinement in magnesium alloys processed by equal-channel angular pressing. *Journal of Materials Science*. 2009;**44**:4758-4762. DOI: 10.1007/s10853-009-3725-z
- [15] Figueiredo RB, Aguilar MTP, Cetlin PR, et al. Processing magnesium alloys by severe plastic deformation. In: *IOP Conference Series: Materials Science and Engineering*. England: IOP Publishing; 2014. p. 012171. DOI: 10.1088/1757-899X/63/1/012171



- [16] Mostaed E, Vedani M, Hashempour M, et al. Influence of ECAP process on mechanical and corrosion properties of pure Mg and ZK60 magnesium alloy for biodegradable stent applications. *Biomater*. 2014;**4**:e28283. DOI: 10.4161/biom.28283
- [17] Figueiredo RB, Langdon TG. Grain refinement and mechanical behavior of a magnesium alloy processed by ECAP. *Journal of Materials Science*. 2010;**45**:4827-4836. DOI: 10.1007/s10853-010-4589-y
- [18] Kim HK, Kim WJ. Microstructural instability and strength of an AZ31 Mg alloy after severe plastic deformation. *Materials Science and Engineering: A*. 2004;**385**:300-308. DOI: 10.1016/J.MSEA.2004.06.055
- [19] Su CW, Lu L, Lai MO. A model for the grain refinement mechanism in equal channel angular pressing of Mg alloy from microstructural studies. *Materials Science and Engineering: A*. 2006;**434**:227-236. DOI: 10.1016/J.MSEA.2006.06.103
- [20] Lin HK, Huang JC, Langdon TG. Relationship between texture and low temperature superplasticity in an extruded AZ31 Mg alloy processed by ECAP. *Materials Science and Engineering: A*. 2005;**402**:250-257. DOI: 10.1016/J.MSEA.2005.04.018
- [21] Xia K, Wang JT, Wu X, et al. Equal channel angular pressing of magnesium alloy AZ31. *Materials Science and Engineering: A*. 2005;**410-411**:324-327. DOI: 10.1016/j.msea.2005.08.123
- [22] Jin L, Lin D, Mao D, et al. Microstructure evolution of AZ31 Mg alloy during equal channel angular extrusion. *Materials Science and Engineering: A*. 2006;**423**:247-252. DOI: 10.1016/J.MSEA.2006.02.045
- [23] Figueiredo RB, Langdon TG. Principles of grain refinement and superplastic flow in magnesium alloys processed by ECAP. *Materials Science and Engineering: A*. 2009;**501**:105-114. DOI: 10.1016/J.MSEA.2008.09.058
- [24] Janeček M, Popov M, Krieger MG, et al. Mechanical properties and microstructure of a Mg alloy AZ31 prepared by equal-channel angular pressing. *Materials Science and Engineering: A*. 2007;**462**:116-120. DOI: 10.1016/J.MSEA.2006.01.174
- [25] Zúberová Z, Estrin Y, Lamark TT, et al. Effect of equal channel angular pressing on the deformation behaviour of magnesium alloy AZ31 under uniaxial compression. *Journal of Materials Processing Technology*. 2007;**184**:294-299. DOI: 10.1016/J.JMATPROTEC.2006.11.098
- [26] Estrin Y, Yi SB, Brokmeier H-G, et al. Microstructure, texture and mechanical properties of the magnesium alloy AZ31 processed by ECAP. *International Journal of Materials Research*. 2008;**99**:50-55. DOI: 10.3139/146.101611
- [27] Lapovok R, Estrin Y, Popov MV, et al. Enhanced superplasticity in a magnesium alloy processed by equal-channel angular pressing with a back-pressure. *Advanced Engineering Materials*. 2008;**10**:429-433. DOI: 10.1002/adem.200700363
- [28] Ding SX, Chang CP, Kao PW. Effects of processing parameters on the grain refinement of magnesium alloy by equal-channel angular extrusion. *Metallurgical and Materials Transactions A: Physical Metallurgy and Materials Science*. 2009;**40**:415-425. DOI: 10.1007/s11661-008-9747-3
- [29] Xu C, Xia K, Langdon TG. Processing of a magnesium alloy by equal-channel angular pressing using a back-pressure. *Materials Science and Engineering: A*. 2009;**527**:205-211. DOI: 10.1016/J.MSEA.2009.07.063

- [30] Kang F, Liu JQ, Wang JT, et al. The effect of hydrostatic pressure on the activation of non-basal slip in a magnesium alloy. *Scripta Materialia*. 2009;**61**:844-847. DOI: 10.1016/J.SCRIPMAT.2009.07.011
- [31] Miyahara Y, Horita Z, Langdon TG. Exceptional superplasticity in an AZ61 magnesium alloy processed by extrusion and ECAP. *Materials Science and Engineering: A*. 2006;**420**:240-244. DOI: 10.1016/J.MSEA.2006.01.043
- [32] Mabuchi M, Ameyama K, Iwasaki H, et al. Low temperature superplasticity of AZ91 magnesium alloy with non-equilibrium grain boundaries. *Acta Materialia*. 1999;**47**:2047-2057. DOI: 10.1016/S1359-6454(99)00094-4
- [33] Máthis K, Gubicza J, Nam NH. Microstructure and mechanical behavior of AZ91 Mg alloy processed by equal channel angular pressing. *Journal of Alloys and Compounds*. 2005;**394**:194-199. DOI: 10.1016/J.JALLCOM.2004.10.050
- [34] Yamashita A, Horita Z, Langdon TG. Improving the mechanical properties of magnesium and a magnesium alloy through severe plastic deformation. *Materials Science and Engineering: A*. 2001;**300**:142-147. DOI: 10.1016/S0921-5093(00)01660-9
- [35] Suwas S, Gottstein G, Kumar R. Evolution of crystallographic texture during equal channel angular extrusion (ECAE) and its effects on secondary processing of magnesium. *Materials Science and Engineering: A*. 2007;**471**: 1-14. DOI: 10.1016/J.MSEA.2007.05.030
- [36] Gan WM, MYz Z, Chang H, et al. Microstructure and tensile property of the ECAPed pure magnesium. *Journal of Alloys and Compounds*. 2009;**470**:256-262. DOI: 10.1016/J.JALLCOM.2008.02.030
- [37] Spitale F, Poggiali J, Figueiredo RB, et al. Grain refinement of commercial purity magnesium processed by ECAP (equal channel angular pressing). *Materials Research*. 2012;**15**:312-316. DOI: 10.1590/S1516-14392012005000022

# Fatigue of Magnesium-Based Materials

*Jafar Albinmousa*

## Abstract

Magnesium alloys and metal matrix composites (MMCs) are attractive materials for biomedical application. Magnesium has a module of elasticity that is close to that of human bones and it is biocompatible with the human body. Human body fluids make a corrosive environment to magnesium. In addition, different body parts are subjected to cyclic loading reaching a magnitude of about 80 MPa and an estimated total of 106 cycles per year. Therefore, understanding the fatigue behavior of magnesium alloys and magnesium metal matrix composites (MMCs) is an essential aspect especially when they are used as load bearing components. Magnesium has a hexagonal closed-packed (HCP) lattice structure with a  $c/a$  ratio of 1.623, and it does not have enough independent slip systems to sustain large plastic deformation. Therefore, magnesium deforms plastically by two different mechanisms: slipping and twinning. Twinning-detwinning deformation is manifested in the cyclic stress-strain response of wrought magnesium alloys when loaded along the working direction. A significant stress asymmetry is usually observed resulting in the development of high mean stress. Research on magnesium and its alloys is rapidly increasing. This chapter presents different aspects of fatigue, in general, and on magnesium in particular, including experimental method, damage models and fatigue life equation.

**Keywords:** fatigue, cyclic behavior, life estimation, Mg alloys, magnesium metal matrix composites

## 1. Introduction

Magnesium has a hexagonal closed-packed (HCP) lattice structure with a  $c/a$  ratio of 1.623. According to von Mises [1], the ductility of the material, which depends on its ability to withstand general homogeneous strain that involves changes in the shape of the crystal, is possible when five independent slip systems are activated. This condition is not met in HCP metals such as magnesium, therefore, deform plastically by two mechanisms: slip and twinning. Slip and twin planes for HCP metals are illustrated in **Figures 1** and **2**. Among these systems, the basal slip (0001) and the  $(10\bar{1}2)$  tension twin are easiest to be activated due to their low critical resolved shear stresses (CRSS).

The American Society of Testing and Materials (ASTM) [3] defines fatigue as “the process of progressive localized permanent structural change occurring in a material subjected to conditions that produce fluctuating stresses and strains at some point or points and that may culminate in cracks or complete fracture after a

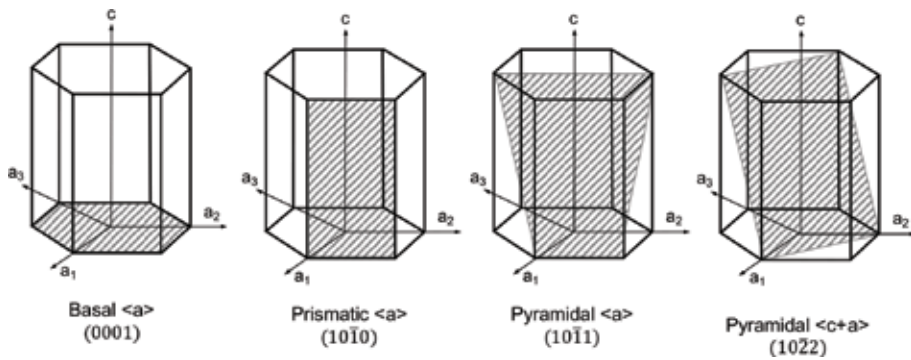


**Figure 1.**  
Slip planes in HCP metals [2].

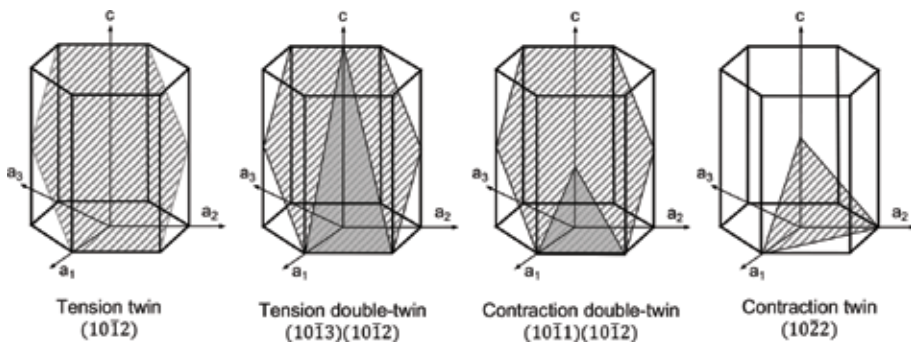


**Figure 2.**  
Twin planes in HCP metals [2].

sufficient number of fluctuations”. Fatigue failure can occur even if the generated stress is below the yield limit. Therefore, in a macro-scale viewpoint fatigue failure is similar to brittle fracture where no signs of severe plastic deformation such as necking are observed.

Cyclic loading is very common. It can occur because of operational conditions such as increase and decrease of loads or due to the motion of loaded parts. Cyclic loads can be classified into constant and random loads. Constant load can be represented by an amplitude and a mean. A cycle in a constant amplitude loading is clearly defined. However, the definition of a cycle in random loading case is not as clear as in constant amplitude loading. Therefore, a count method is required to quantify the number of cycles in random loading situation. Applied cyclic loading can either be uniaxial or multiaxial. In a constant multiaxial cyclic loading, amplitudes, means, phases and frequencies of the applied loads can be different. Of course, multiaxial loading can involve random loads.

The classifications explained before were merely based on mechanical loads such as forces, moments and torques. However, fatigue damage might result from the application of cyclic thermal loads. In addition, fatigue damage process can get complex due to interactions between applied cyclic loads, mechanical or thermal, and other damaging phenomena such as creep. Effect of environmental attacks, residual stress, coating, surface finish, geometrical irregularities have significant impact on fatigue damage process and fatigue life.

There are two approaches to study fatigue of materials: initiation and propagation of cracks. Fatigue initiation approach is concerned about relation between the applied cyclic loads and the initiation of small cracks that generally do not exceed

1 mm in size. On the other hand, fatigue propagation approach is concerned about the relation between the applied cyclic loads and the growth of an existing crack to a size that causes catastrophic failure.

The initiation approach, which is commonly referred to as *fatigue*, is classified based on the damaging variable. There are three methods to analyzing fatigue: stress-, strain- and energy-based. If a damage model, stress-, strain- or energy-based, is calculated on specific planes the used method is further classified as *critical plane* method. Stress-based methods use stresses, normal and/or shear, to quantify fatigue damage. Similarly, strain-based method use strains, normal and/or shear, to quantify fatigue damage. Lastly, energy-based methods use strain energy density to quantify fatigue damage.

All fatigue models require monotonic and/or cyclic properties of materials. Strain and energy-based cyclic properties can be obtained by performing series of tests under strain-controlled loading condition. On the other hand, stress-based cyclic tests properties can be obtained by performing series of tests under stress-controlled loading condition. The well-known stress-life and strain-life curves can be obtained from these tests.

## 2. Characterization of fatigue behavior

A common classification in fatigue initiation analysis is based on fatigue life [4]. The term “low cycle fatigue, LCF” refers to fatigue failure that occurs between  $10^3$  and  $10^5$  cycles. On the other hand, the term “high cycle fatigue, HCF” refers to fatigue failure that occurs between  $10^5$  and  $10^7$  cycles. The last class is called “very high cycle fatigue, VHCF” that refers to fatigue failure that occurs after  $10^7$  cycles. Because it is easier to control the stress at low load levels than strain, HCF and VHCF tests are usually performed under stress-controlled condition. However, strain-controlled tests can be performed with wide strain levels that cover lives less than  $10^3$  and up to  $10^7$  cycles. Because strain-controlled tests are usually performed at high strain levels and significant plasticity resulting in low number of cycles to failure, heating of the sample due to internal friction becomes a concern. Therefore, tests that are expected to last for few hundred or thousand cycles shall be performed with frequencies that shall not exceed few Hertz, if not less 1 Hz. Yet, a common practice in strain-controlled testing is to switch the control mode to stress when a test exceeds  $10^4$  cycles. This allows for increasing the frequency to reduce the time required to finish the test. On the contrary, HCF and VHCF tests are usually performed with frequencies higher than 20 Hz.

### 2.1 High cycle fatigue

The high cycle fatigue behavior of materials can be characterized for a mode of stress, i.e., normal or shear, by performing stress-controlled experiments. ASTM standard for conducting force controlled constant amplitude axial fatigue tests of metallic materials [5] can be followed in tests performed using cyclic axial machine. Similarly, the standard by International Organization for Standardization [6] can be followed in tests performed using four-point rotating bending machine. Unlike cyclic axial or rotating bending tests that are usually performed on solid specimens, cyclic torsion test is usually performed on tubular specimen because shear stress across tubular specimens that satisfy thin-walled tube condition can be assumed constant. Of course, a machine with dynamic torsional load cell is required to perform cyclic torsional experiment. There is no particular standard for performing

cyclic torsional tests, however, the ASTM standard for strain-controlled axial-torsional fatigue testing with thin-walled tubular specimens [7] can be used.

The stress-life ( $S - N$ ) curve, which is also known as the Wöhler curve, is usually used to represent the relation between applied stress amplitude,  $\sigma_a$  or  $\tau_a$  and fatigue life  $N_f$  in a log-log scale. A typical  $S - N$  curve shows a linear curve in the finite life region as shown in **Figure 3**.

Understanding that a linear curve in a log-log scale indicates that the relation between the stress amplitude and fatigue life is of a power-type, Basquin [8] was the first to model this curve as

$$\sigma_a = \sigma'_f (2N_f)^b \quad (1)$$

where  $\sigma'_f$  is the axial fatigue strength coefficient and  $b$  is the axial fatigue strength exponent.

Some materials such as steel and magnesium alloys show a distinct plateau commonly called the “fatigue limit”. This limit is usually observed between  $10^6$  and  $10^7$  cycles. Tests that exceed  $10^7$  cycles are usually stopped and are called run-out. This limit used to be called the “endurance limit” that is a stress amplitude below which no failure will occur. However, it has been shown if the testing is continued specimens eventually fail. Therefore, it is recently accepted that endurance limit

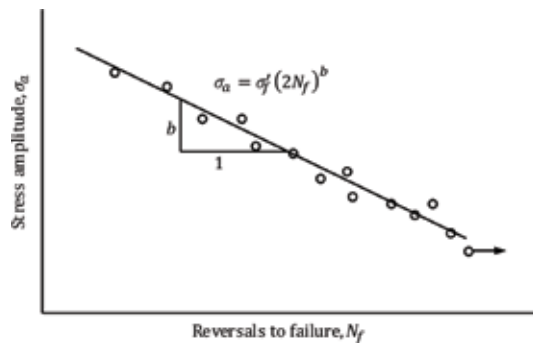


**Figure 3.**  
A typical stress life curve.

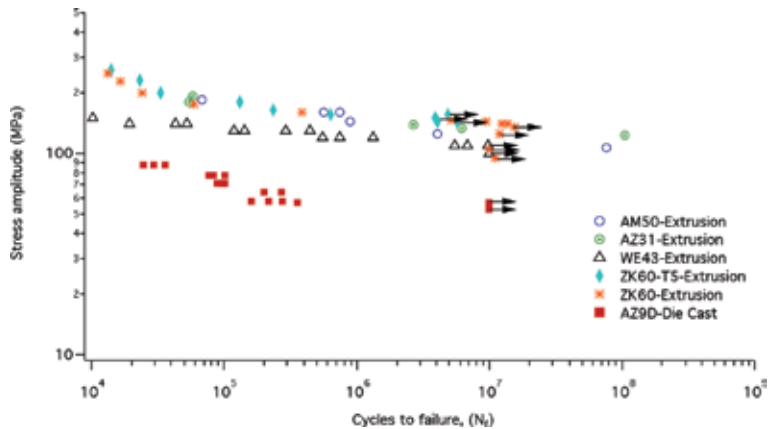


**Figure 4.**  
Stress life curve for different Mg-alloys [9–13].

does not exist. Run-out tests are usually marked with an arrow symbol. Stress-life curves for six different magnesium alloys are presented in **Figure 4**. This figure clearly shows the difference between die-cast and extruded alloys with the former having less fatigue strength due to the existence of pores and cavity resulting from the casting process.

## 2.2 Low cycle fatigue

Similar to the HCF, the low cycle fatigue (LCF) behavior of materials can be characterized for a mode of strain, i.e., normal or shear, by performing strain-controlled experiments. ASTM standard for conducting strain controlled fatigue tests of materials [14] can be followed in tests performed using cyclic axial machine. While controlling the strain, using strain measurement device such as an extensometer, the load signal is also acquired. This allows calculating both the stress and strain that can be represented for a given cycle by a hysteresis loop as shown in **Figure 5**.

Wrought alloys that are produced by extrusion, rolling or forging processes develop strong texture. This texture is characterized by alignment of the basal plane with the working direction with the c-axis perpendicular to it. The two plastic deformation mechanisms, slipping or twinning, can be activated depending on the loading orientation with respect to the basal plane. An extension along the c-axis activates the tension twins and a subsequent contraction causes detwinning of the lattice. During cyclic loading, twinning occurs in the compression reversal leading to low stress yielding. Detwinning starts as the load is reversed, i.e., during the tension reversal. However, as the tension load increases the hard pyramidal slip is activated in order to accommodate additional strain. This change from detwinning to slip is reflected on the cyclic hysteresis as an inflection point and a concave upward hardening behavior. A representative cyclic hysteresis loop for different magnesium extrusion loaded along the extrusion direction is shown in **Figure 6**.

The strain-life ( $\epsilon - N$ ) curve is usually used to represent the relation between applied strain amplitude,  $\epsilon$  and fatigue life  $N_f$  in a log-log scale. Strain life curves for AZ31B, AZ61A and ZK60 magnesium extrusions are presented in **Figure 7**.

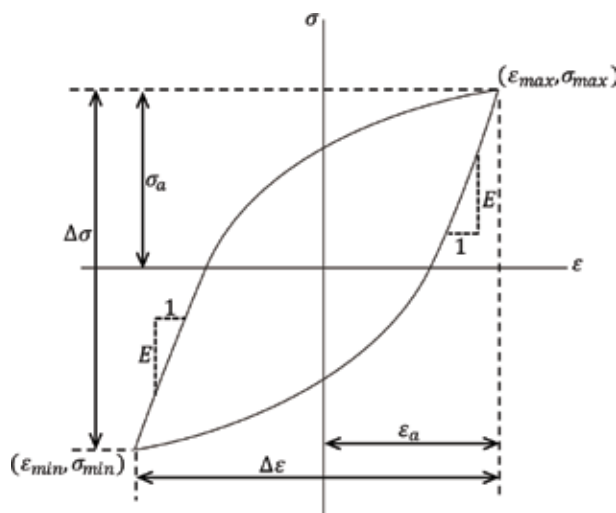


**Figure 5.**  
A typical cyclic hysteresis loop [2].

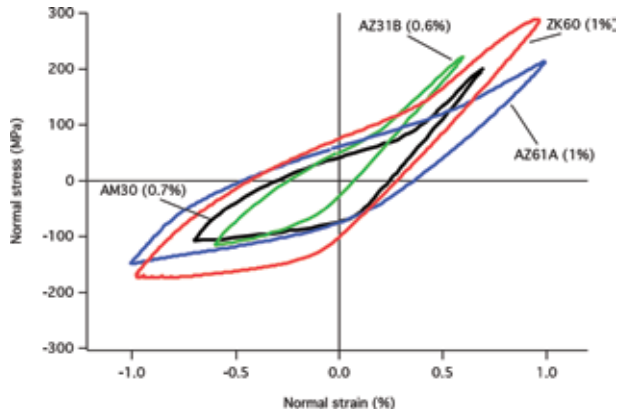


**Figure 6.** Cyclic hysteresis loops of AZ31B, AZ61A, AM30 and ZK60 magnesium extrusions [15–18].

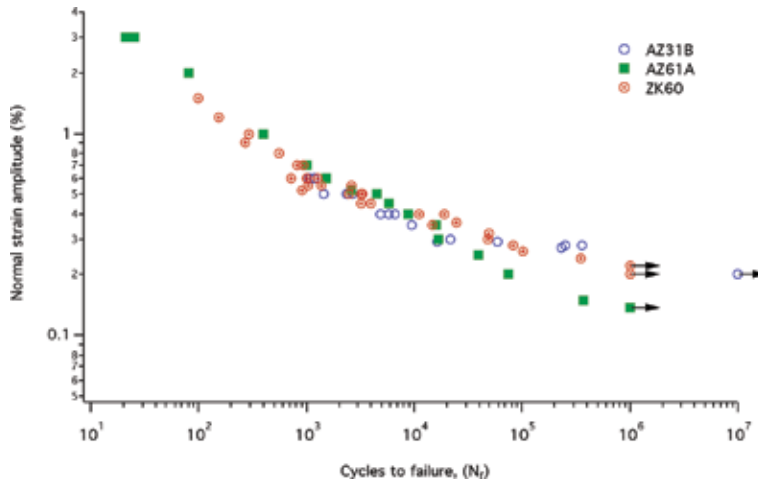


**Figure 7.** Strain life curves for AZ31B, AZ61A and ZK60 magnesium extrusions [17–19].

This region is represented by the Coffin-Manson [20, 21] equation as

$$\epsilon_a = \frac{\sigma'_f}{E} (2N_f)^b + \epsilon'_f (2N_f)^c \quad (2)$$

where  $\sigma'_f$  and  $b$  are defined in Eq. (1) and  $\epsilon'_f$  and  $c$  are the axial fatigue ductility coefficient and the axial fatigue ductility exponent, respectively.

Ellyin, Golos and Xia [22] energy model is considered as the basis for the application of strain energy in correlating multiaxial fatigue damage. The model considers the plastic and the positive elastic strain energy densities as the damaging variables as shown in **Figure 8**.

The plastic strain energy density is the area enclosed by the cyclic hysteresis loop which is calculated as [23]:

$$\Delta W^p = \int_{cycle} \sigma d\epsilon \quad (3)$$



While the positive elastic strain energy density is calculated as

$$\Delta W_e^+ = \frac{\sigma_{max}^2}{2E} \quad (4)$$

The total strain energy density is often calculated as the sum of torsional of the plastic and positive elastic energies

$$\Delta W_t = \Delta W_e^+ + \Delta W_p \quad (5)$$

The inclusion of the positive elastic strain energy density is a method for considering the mean stress effect in energy method.

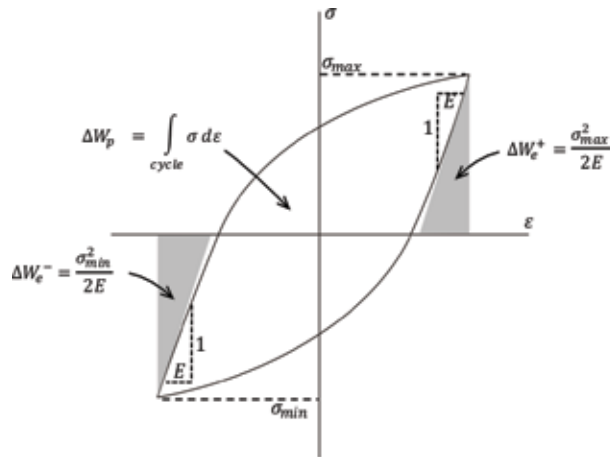


**Figure 8.**  
 Energy components in cyclic hysteresis loop [2].

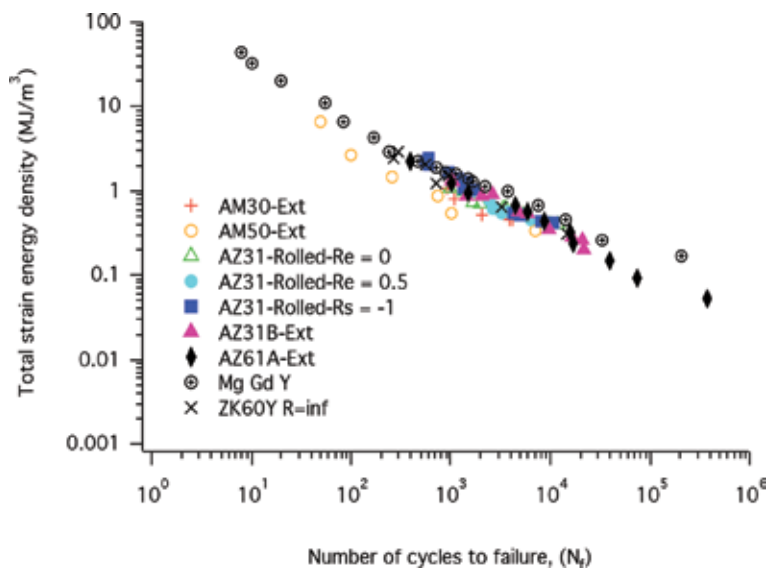


**Figure 9.**  
 Energy life curves of Mg [17–19, 24–27].

Property	AZ31B extrusion	AZ61A extrusion	AM30 extrusion
$\sigma'_f$	723.5	586.1	410.4
$b$	-0.159	-0.153	-0.130
$\epsilon'_f$	0.252	1.823	1.480
$c$	-0.718	-0.832	-0.791
$E'_e$	20.29	7.01	2.995
$B$	-0.440	-0.373	-0.281
$E'_f$	510.74	924.14	1710.69
$C$	-1.052	-1.001	-0.975

**Table 1.** Strain and energy fatigue properties of different Mg extruded alloys [16, 18, 28].

The fatigue life is estimated using

$$\Delta W_t = \alpha N_f^\beta \quad (6)$$

**Figure 9** shows the correlation between the total strain energy density and fatigue life for several magnesium alloys tested at different loading conditions. This figure clearly shows the ability of the energy method to collapse all data in a single and narrow scatter band.

Strain- and energy-based fatigue properties for AZ31B, AZ61A and AM30 magnesium extrusions are listed in **Table 1**.

### 2.3 Mean stress effect

Mean stress has a significant effect on fatigue behavior of materials. It is generally observed that tensile mean stresses are detrimental and compressive mean stresses are beneficial. As explained earlier, the positive elastic strain energy density is used to account for the mean stress effect in energy methods. There are different models for stress-based methods that account for mean stress effect [29]:

The Modified Goodman:

$$\frac{\sigma_a}{\sigma_f} + \frac{\sigma_m}{\sigma_u} = 1 \quad (7)$$

Gerber:

$$\frac{\sigma_a}{\sigma_f} + \left(\frac{\sigma_m}{\sigma_u}\right)^2 = 1 \quad (8)$$

Morrow:

$$\frac{\sigma_a}{\sigma_f} + \left(\frac{\sigma_m}{\sigma'_f}\right)^2 = 1 \quad (9)$$

where  $\sigma_f$  is the fatigue limit.

Morrow's can be used for strain-based method as:

$$\frac{\Delta \epsilon}{2} = \epsilon_a = \frac{\sigma'_f - \sigma_m}{E} (2N_f)^b + \epsilon'_f (2N_f)^c \quad (10)$$

Another equation suggested by Smith, Watson and Topper [30], commonly known as “SWT parameter”, is as follows:

$$\sigma_{max}\epsilon_a E = (\sigma'_f)^2 (2N_f)^{2b} + \sigma'_f \epsilon'_f E (2N_f)^{c+b} \quad (11)$$

## 2.4 Environmental effects

Environmental effects such as corrosion or temperature have significant effect on fatigue life. The interactions between these effects and fatigue behavior are complex, therefore, quantitative models for estimating fatigue life may not always be possible. Magnesium is highly reactive and considered as one of the most electrochemically active metals. From structural view point, the reactivity of magnesium, and its alloys, in electrolytic or aqueous environments, is disadvantageous because it degrades their mechanical strength. In the contrary, this high reactivity of magnesium and its alloys make them a potential biodegradable materials.

The pH level of body fluid ranges from 1 to 9 in different tissues. It is also estimated that different parts of the body are subjected to different level of stresses. For example, bones are subjected to a stress of about 4 MPa during regular daily activities. On the other hand, tendons and ligaments experience peak stresses that range from 40 to 80 MPa. Hip joints usually subjected to 3 times the body weight which can increase to 10 times during jumping. These stresses are repetitive and fluctuating reaching to  $1 \times 10^6$  cycles in a year [31, 32].

The poor corrosion resistance of many magnesium alloys is due to internal galvanic corrosion caused by second phases or impurities and the instability of the hydroxide film [33]. The most common method to assess the influence of corrosion on fatigue behavior is to perform stress-controlled testing at different environmental conditions. Strain-controlled testing is not common because it requires electronic strain measurement device that may not be possible to mount on the sample while being exposed to corrosive substances. Comparisons between stress-life curves for different biomedical magnesium alloys tested at different simulated body fluids “SBF” are shown in **Figures 10** and **11**. These figures show that the fatigue life of AZ91D at a given stress amplitude is significantly influenced by the condition of the corrosive environment.

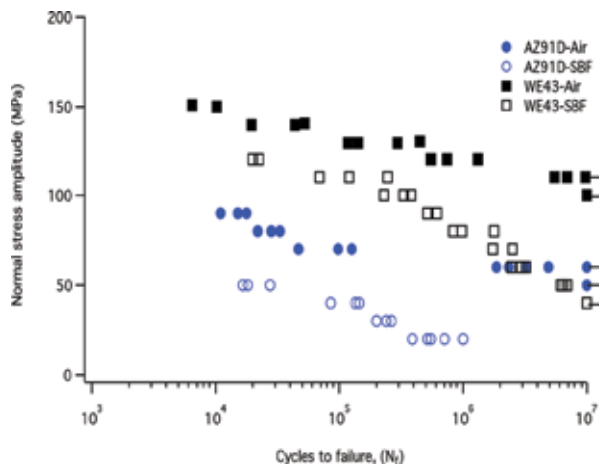


**Figure 10.** Comparison between the stress life curves for biomedical AZ91D and WE43 tested in air and simulated body fluid “SBF” [33].

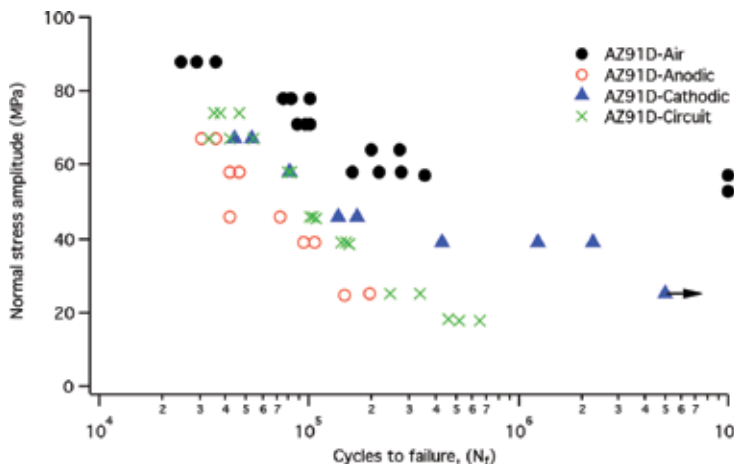


**Figure 11.** Comparison between the stress life curves for biodegradable AZ91D tested in air and different simulated body fluids “SBF” [11].

### 3. Metal matrix composites

Metal-matrix composites (MMCs) are a class of materials that are usually made by reinforcing conventional metallic matrix using high-performance second phase constituents. Metal-matrix composites MMCs can be tailored to improve different properties such as strength, stiffness, thermal conductivity, and corrosion, wear, creep resistance. In general, metal-matrix composites (MMCs) can be produced by stir casting, squeeze casting and powder metallurgy.

Magnesium matrix composites can be fabricated by using different reinforcements to obtain different characteristics. For example, Mg<sub>2</sub>Si/Mg composites have a mechanical strength that is comparable to that of industrial magnesium cast alloys (AZ63) but with a damping capacity that is 100 times higher [34]. Carbon nanotubes (CNTs) can be used as reinforcements with magnesium [35] or its alloys

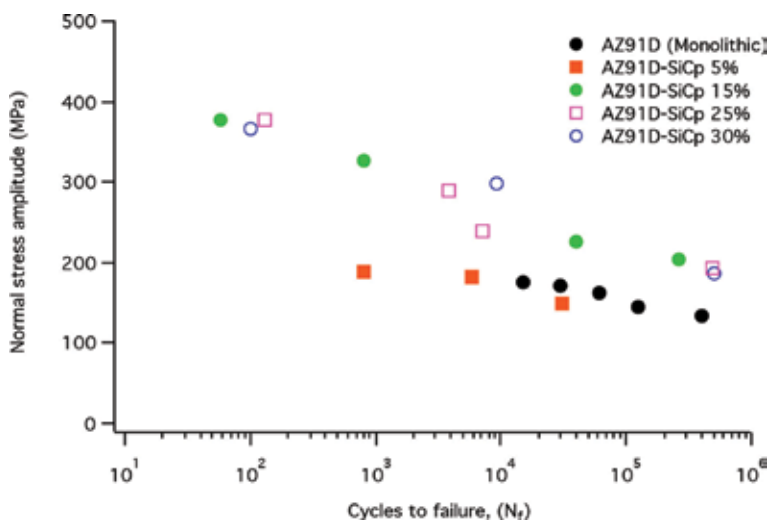


**Figure 12.** The effect of different volume fractions of SiCp on the stress-life curve of AZ91D magnesium metal matrix composite [41, 42].

such as AZ31, AZ91, ZK60 and AZ61 to improved their ultimate tensile strength, yield strength and modulus of elasticity composite [36]. Different reinforcements such as aluminum oxide particulate  $Al_2O_3$  [37], nickel particles [38] or nano-size  $Y_2O_3$  particles [39] have been tested with magnesium and its alloys and found to yield different results.

Fatigue behavior of magnesium AZ91 can be improved by adding ceramic reinforcements [40]. In addition, the elastic modulus, yield strength and ultimate tensile strength of AZ91 can be increased using SiCp particles as discontinuous reinforcements. **Figures 12** and **13** show the effects of two different reinforcements

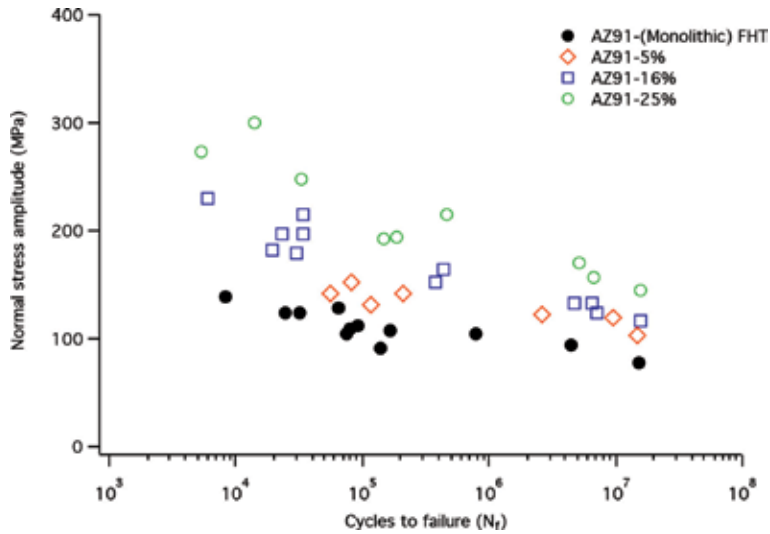


**Figure 13.** The effect of different volume fractions of Saffil alumina fibers on the stress-life curve of AZ91D magnesium metal matrix composite [40].

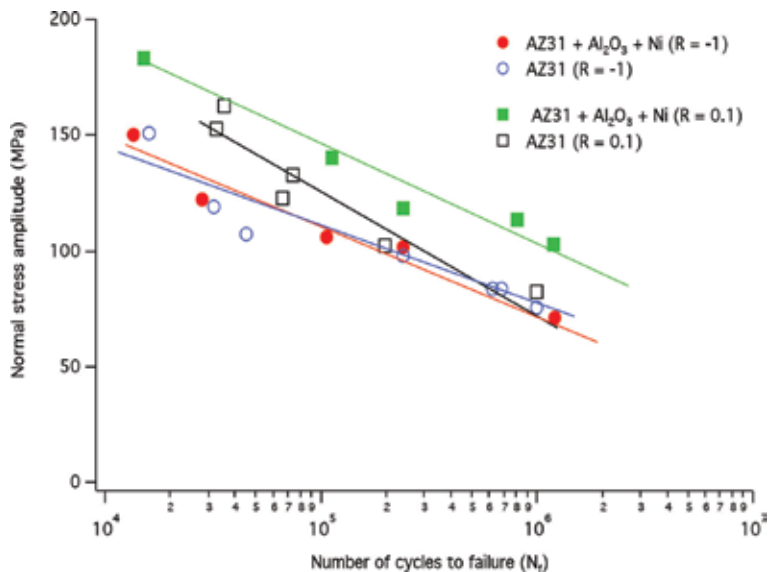


**Figure 14.** Comparison of stress-strain curves of the dual particle reinforced magnesium alloy ( $AZ_{31} + Al_2O_3 + Ni$ ) with the unreinforced matrix alloy ( $AZ_{31}$ ) cyclically deformed at room temperature ( $T = 25^\circ C$ ) at  $R = 0.1$  and  $-1.0$  [38].

on the stress-life curve of magnesium AZ91D. These figures show that fatigue life at a given stress amplitude can be increased by adding proper volume fraction of the reinforcements.

In addition, fatigue life of AZ31 can be improved by using nano-particulates of aluminum oxide and micron size nickel particles reinforcements as shown in **Figure 14**.

#### **4. Summary**

Magnesium is a promising material for biomedical applications. Because body parts such as hip joints, bones and knees are subjected to cyclic loading fatigue is an essential tool for designing implants and replacement components for these parts. Accurate determination of the stress and strain states is critical for a successful fatigue design process. Magnesium has a hexagonal close packed crystal structure resulting in a complex stress-strain behaviors. It has been explained that the involvement of slipping, twinning and detwinning deformation mechanisms causes the unusual cyclic hysteresis loop of wrought magnesium alloys. Therefore, suitable cyclic plasticity model is required for estimating the cyclic stress-strain state. Different fatigue damage models such as stress-, strain- and energy-based parameters can be used to correlate the fatigue damage with life. Although biodegradability is an attractive characteristic of biomedical materials, the high reactivity of magnesium in electrolytic or aqueous environments calls for further developments. The properties of magnesium and its alloys can be improved by reinforcing them using selected reinforcements.

#### **Author details**

Jafar Albinmoussa

Mechanical Engineering Department, KFUPM, Dhahran, Saudi Arabia

\*Address all correspondence to: binmoussa@kfupm.edu.sa

#### **IntechOpen**

---

© 2020 The Author(s). Licensee IntechOpen. This chapter is distributed under the terms of the Creative Commons Attribution License (<http://creativecommons.org/licenses/by/3.0>), which permits unrestricted use, distribution, and reproduction in any medium, provided the original work is properly cited. 

## References

- [1] von Mises R. Mechanik der plastischen Formänderung von Kristallen. ZAMM-Journal of Applied Mathematics and Mechanics/Zeitschrift für Angewandte Mathematik und Mechanik. 1928;**8**(3):161-185
- [2] Albinmousa J. Multiaxial fatigue characterization and modeling of AZ31B magnesium extrusion [PhD thesis]. Waterloo, Ontario in Canada: University of Waterloo; 2012
- [3] ASTM E1823-13, Standard Terminology Relating to Fatigue and Fracture Testing. 2013
- [4] Pyttel B, Schwerdt D, Berger C. Very high cycle fatigue—Is there a fatigue limit? International Journal of Fatigue. 2011;**33**(1):49-58
- [5] ASTM E466-15, Standard Practice for Conducting Force Controlled Constant Amplitude Axial Fatigue Tests of Metallic Materials. West Conshohocken, PA, USA; 2015
- [6] International Organization for Standardization ISO 1143: 2010 (E). Metallic Materials—Rotating Bar Bending Fatigue Testing. Geneva, Switzerland; 2010
- [7] ASTM E2207-15, Standard Practice for Strain-Controlled Axial-Torsional Fatigue Testing with Thin-Walled Tubular Specimens. West Conshohocken, PA, USA; 2015
- [8] Basquin OH. The exponential law of endurance tests. American Society for Testing and Materials Proceedings. 1910;**10**(Part 11):625
- [9] Liu WC et al. High cycle fatigue behavior of as-extruded ZK60 magnesium alloy. Journal of Materials Science. 2009;**44**(11):2916-2924
- [10] Liu W et al. Effect of shot peening on surface characteristics and fatigue properties of T5-treated ZK60 alloy. Materials Transactions. 2009;**50**(4): 791-798
- [11] Sajjad J, Singh Raman RK, Davies CHJ. Corrosion fatigue of a magnesium alloy in modified simulated body fluid. Engineering Fracture Mechanics. 2015;**137**:2-11
- [12] Ya U et al. Corrosion fatigue of extruded magnesium alloys. Materials Science and Engineering: A. 2003;**360** (1-2):132-139
- [13] Gu XN et al. Corrosion fatigue behaviors of two biomedical Mg alloys—AZ91D and WE43—in simulated body fluid. Acta Biomaterialia. 2010;**6**(12): 4605-4613
- [14] ASTM E606/E606M-12, Standard Test Method for Strain-Controlled Fatigue Testing. West Conshohocken, PA, USA; 2012
- [15] Albinmousa J, Jahed H, Lambert S. Cyclic axial and cyclic torsional behaviour of extruded AZ31B magnesium alloy. International Journal of Fatigue. 2011;**33**(11): 1403-1416
- [16] Roostaei AA, Jahed H. Role of loading direction on cyclic behaviour characteristics of AM30 extrusion and its fatigue damage modelling. Materials Science and Engineering: A. 2016;**670**: 26-40
- [17] Yu Q et al. An experimental study on cyclic deformation and fatigue of extruded ZK60 magnesium alloy. International Journal of Fatigue. 2012; **36**(1):47-58
- [18] Yu Q et al. Multiaxial fatigue of extruded AZ61A magnesium alloy. International Journal of Fatigue. 2011; **33**(3):437-447

- [19] Albinmousa J, Jahed H. Multiaxial effects on LCF behaviour and fatigue failure of AZ31B magnesium extrusion. *International Journal of Fatigue*. 2014; **67**:103-116
- [20] Tavernelli JF, Coffin LF. Experimental support for generalized equation predicting low cycle fatigue. *Transactions of the American Society of Mechanical Engineers, Journal of Basic Engineering*. 1962;**84**(4):533
- [21] Manson SS. Discussion on JF. Tavernelli and LF. Coffin experimental support for generalized equation predicting low cycle fatigue. *Transactions of the American Society of Mechanical Engineers, Journal of Basic Engineering*. 1962;**84**(4):537
- [22] Ellyin F, Golos K, Xia Z. In-phase and out-of-phase multiaxial fatigue. *Journal of Engineering Materials and Technology*. 1991;**113**(1):112-118
- [23] Jahed H et al. An energy-based fatigue life assessment model for various metallic materials under proportional and non-proportional loading conditions. *International Journal of Fatigue*. 2007;**29**(4):647-655
- [24] Mousa JAB. Multiaxial fatigue characterization and modeling of AZ31B magnesium extrusion. 2012
- [25] Park SH et al. Low-cycle fatigue characteristics of rolled Mg-3Al-1Zn alloy. *International Journal of Fatigue*. 2010;**32**(11):1835-1842
- [26] Chen L et al. Low-cycle fatigue behavior of an As-extruded AM50 magnesium alloy. *Metallurgical and Materials Transactions A*. 2007;**38**: 2235-2241
- [27] Yang F et al. Enhanced very high cycle fatigue performance of extruded Mg-12Gd-3Y-0.5Zr magnesium alloy. *Materials Science and Engineering: A*. 2011;**528**(6):2231-2238
- [28] Iftikhar SH, Albinmousa J. A method for assessing critical plane-based multiaxial fatigue damage models. *Fatigue & Fracture of Engineering Materials & Structures*. 2018;**41**(1): 235-245
- [29] Stephens RI et al. *Metal Fatigue in Engineering*. USA: John Wiley & Sons; 2000
- [30] Smith KN, Watson P, Topper TH. A stress-strain function for the fatigue of metals. *Journal of Materials*. 1970;**5**: 767-778
- [31] Ramakrishna S et al. Biomedical applications of polymer-composite materials: A review. *Composites Science and Technology*. 2001;**61**(9):1189-1224
- [32] Black J. *Biological Performance of Materials: Fundamentals of Biocompatibility*. USA: CRC Press; 2005
- [33] Song GL, Atrens A. Corrosion mechanisms of magnesium alloys. *Advanced Engineering Materials*. 1999;**1**(1):11-33
- [34] Schaller R. Metal matrix composites, a smart choice for high damping materials. *Journal of Alloys and Compounds*. 2003;**355**(1-2):131-135
- [35] Goh CS et al. Ductility improvement and fatigue studies in Mg-CNT nanocomposites. *Composites Science and Technology*. 2008;**68**(6):1432-1439
- [36] Li CD et al. Distribution and integrity of carbon nanotubes in carbon nanotube/magnesium composites. *Journal of Alloys and Compounds*. 2014; **612**:330-336
- [37] Srivatsan TS et al. The role of aluminum oxide particulate reinforcements on cyclic fatigue and final fracture behavior of a novel magnesium alloy. *Materials Science and Engineering: A*. 2012;**532**:196-211



- [38] Srivatsan TS et al. Influence of nickel particle reinforcement on cyclic fatigue and final fracture behavior of a magnesium alloy composite. *Metals*. 2012;2(2):143-169
- [39] Goh CS et al. The cyclic deformation behavior of Mg-Y2O3 nanocomposites. *Journal of Composite Materials*. 2008; 42(19):2039-2050
- [40] Llorca N, Bloyce A, Yue TM. Fatigue behaviour of short alumina fibre reinforced AZ91 magnesium alloy metal matrix composite. *Materials Science and Engineering: A*. 1991;135:247-252
- [41] Vaidya AR, Lewandowski JJ. Effects of SiCp size and volume fraction on the high cycle fatigue behavior of AZ91D magnesium alloy composites. *Materials Science and Engineering: A*. 1996;220 (1-2):85-92
- [42] Hassan HA, Lewandowski JJ. Effects of particulate volume fraction on cyclic stress response and fatigue life of AZ91D magnesium alloy metal matrix composites. *Materials Science and Engineering: A*. 2014;600:188-194



# Abrasive Water Jet Cutting: A Risk-Free Technology for Machining Mg-Based Materials

*Niranjan Channagiri Anandatirthachar, S. Srinivas  
and M. Ramachandra*

## Abstract

Mg-based materials are considered to be the most machinable of all materials due to their good machinability. Though conventional machining of Mg-based materials is a topic that has been widely discussed, they are associated with ignition issues. Ignition risk in conventional machining of Mg-based materials thus cannot be denied and should be avoided. Literature has witnessed ignition risk when machining temperature reaches above 450°C during turning and milling processes, and some cases are reported with fire hazard. In order to obtain the safest machining atmosphere, abrasive water jet machining, a most desired machining technology for machining Mg-based materials, is discussed in the present chapter. The text covers ignition risk in conventional machining of Mg-based materials, an overview of non-traditional methods for machining Mg-based materials, advantages of abrasive water jet machining over other methods, abrasive water jet linear cutting of Mg alloys and composites, and drilling of Mg alloys. Experimental investigations are carried out to know the effect of abrasive water jet process parameters on machining Mg alloys and Mg nanocomposites. Surface topography of cut surfaces is analyzed. Suitability of abrasive water jet in drilling Mg alloys is justified by comparing results with holes drilled by conventional drilling and jig boring.

**Keywords:** ignition risk, Mg, machining, AWJ cutting, AWJ drilling, topography

## 1. Introduction

During the past decades, significant research has been carried out on the development of novel magnesium-based materials as traditional alloys and composites using different techniques such as casting, powder metallurgy, disintegrated melt deposition etc.; several secondary processing techniques have also been used to enhance the physical and mechanical properties of Mg-based materials, namely, heat treatment, equal channel angular pressing (ECAP), forging, rolling, hot extrusion, etc. Mg-based materials have turned out to be a choice for industries to replace structural materials like cast iron, steel, copper, etc. In particular, automobile industries have become potential market for Mg-based materials. Increase in demand for Mg-based materials for lightweight automotive components witnessed significant growth during recent years. Global forecast report has estimated Mg alloys market to reach 1.30 billion in 2018 and is projected to reach USD 2.37 billion

by 2023 at a compound annual growth rate (CAGR) of 12.7% during forecast period [1]. Extended applications in 3Cs (consumer electronics, computers, and cell phones) have enhanced the demand and growth of Mg-based materials in global markets. With this increase in demand, researchers and engineers are continuously focusing on machining aspects of Mg-based materials to expand the industrial applications through advanced machining technologies.

## **2. Ignition risk in conventional machining of Mg-based materials**

Even though Mg-based materials are considered to be the easiest materials to machine due to their low cutting forces, well-formed chips, and good surface finish, they are highly inflammable. The risk of ignition rises when process temperature crosses 450°C, which is close to the melting temperature of Mg [2, 3]. In spite of advantages such as 50% lesser cutting forces compared to aluminum in turning operations and cutting tools retaining sharp edges for a long period, Mg possess high affinity to oxygen at higher temperatures (>450°C). Mg is also reactive in nitrogen and carbon dioxide atmosphere even in the absence of oxygen. Ignition temperature of Mg can be controlled by adding alloying elements such as calcium and beryllium and rare earth metals such as cerium, lanthanum, or yttrium but cannot be avoided [4–6]. Ignition of chips occurs during high-speed machining especially during finishing operations, i.e., chips in the form of powder (<500 µm) tend to explode. These powders not only create safety hazard but can also damage the machine tool components [7].

Weinert et al. [2] highlighted the importance of removing the chips from the workspace of the machine tool during machining. It was reported that the hot chips generated during machining contains up to 90% of the heat generated at the cutting zone, which can significantly affect the workpiece and machine components by transferring the heat. Thermal expansion of both machine tool and workpiece thus required to be identified. The risk of fire and potential damages to the workpiece as well as the machine tool can be significantly controlled by fast and reliable removal of the chips. Controlling the temperature during machining is therefore crucial in preventing the ignition. Ning Zhao et al. [8] reported three types of ignition that occurs during face milling of AM50A magnesium alloy which includes sparks, flares, and continuous flares. Among three types of ignitions, it was reported that flares and continuous flares are dangerous for safe production. Therefore in order to reduce the temperature of chips and powder-type dust generated during machining, many researchers have used cutting fluids during machining process [9–13]. The use of cutting fluids also resulted in reaction with magnesium which forms hydrogen, a highly explosive and flammable gas. For this reactivity issue, mineral-based oils are recommended during machining of Mg-based materials by selecting appropriate process variables. However, it is necessary to take proper care at higher cutting speeds to prevent flank buildup (FBU) on tools while using mineral-based oils because formation of flank BUE and burrs creates another problem in machining Mg-based materials due to high thermal expansion coefficient, and this may further lead to decreased accuracy of machined surfaces. The presence of FBU increases cutting forces and affects surface quality [14].

On the other hand, conventional machining of Mg-MMC is also challenging. In addition to ignition risk, the presence of harder ceramic particles in MMC causes serious abrasion of the tool, which shortens the tool life, and increasing volume fraction of ceramic particles leads to increased cutting forces [15, 16]. This in turn, increases the manufacturing cost. Tonshoff et al. [7] investigated tool wear in turning Mg-MMC containing SiC particle reinforcement (MELRAM 072TS) using

polycrystalline diamond (PCD) tool and PCD, TiN-coated tools. The tin-coated tool was destroyed immediately due to the impact of SiC particles. Chipping off the layer was observed in PCD tool. Furthermore, molten material was observed on edges of all tool materials. This adhesive effect between work and tool material not only creates a negative influence on machining forces but also leads to creating poor surface quality.

Xiangyu Teng et al. [17] studied micro machinability of Mg-MMC containing titanium (Ti) and titanium diboride (TiB<sub>2</sub>) nanoparticles. AlTiN-coated tungsten carbide micro-end mills were used to machine Mg-MMNC. Machined surface was characterized by surface morphology and surface roughness. Investigations revealed cutting tool was affected by chip adhesion. This chip adhesion found more in machining Mg-MMC containing nano-sized Ti particles compared to Mg-MMC containing TiB<sub>2</sub> nanoparticles. Further it was reported that cutting forces while machining Mg/Ti MMC found nearly two times compared to Mg/TiB<sub>2</sub> nanocomposites. Increase in cutting forces increased the roughness of surfaces and also induced burrs on slot edges of cutting tool. The surface of cutting tool was also affected by coating peeling off while machining Mg/TiB<sub>2</sub> nanocomposites.

Therefore machining Mg-MMC with conventional methods is also associated with several problems such as increased cutting forces, surface roughness, and chip adhesion to tool material. It is really challenging to achieve a surface quality and accuracy MMC through conventional machining. Apart from these difficulties, conventional machining system for Mg-based material requires provision of storing chips in closed containers or the use of chip removal systems, protecting the machines using protection systems against explosions, adequate availability of class D fire extinguishers in the machine area, storage of dry sand in containers, and safeguarding the operators and installation of alarm systems in order to create the safest workplace [2, 18]. Indirectly these actions result in higher processing costs. Cost-effective processing of Mg-based materials is therefore an essential criterion to expand the application areas.

### **3. Overview of nontraditional machining of Mg-based materials**

Conventional machining demonstrated significant importance in machining Mg-based materials when compared to NTM over the years, despite serious problems such as ignition risk, tool wear, shorter tool life, and surface finish. Researchers are required to pay more attention to NTM processes to overcome difficulties of conventional machining. Literatures have witnessed the successful implementation of NTM processes in cutting a wide range of materials for different applications. Despite few limitations, nowadays NTM processes are having greater potential than conventional machining. However better understanding is required on the suitability of NTM before being applied in practical fields.

During the past decades, numerous research efforts have been placed on NTM machining of different types of materials including MMCs. However, very limited studies are reported on machining of Mg-based materials and Mg-MMC through NTM techniques. Advantages and limitations of few NTM processes such as laser beam machining (LBM), laser-assisted machining (LAM), electric discharge machining (EDM), and AWJM are discussed in the present section.

Nowadays EDM is extending its application areas by cutting a wide range of metals and MMC. EDM uses high thermal energy to remove the material by electric spark erosion. EDM regardless of the hardness of materials has typical advantages in cutting intricate and complex shapes. EDM eliminates mechanical stresses, vibration, and chatter during machining since there is no direct contact between

tool and work material. EDM is especially used in the production of die, mold, automotive, surgical, and aerospace components. EDM is most suitable for machining of geometries with high aspect ratio and microstructures. EDM can drill a hole of size 0.1 mm [19]. Ponappa et al. reported with high aspect ratio holes of  $\phi$  0.5 mm with 12 mm height drilled by EDM in Mg/Al<sub>2</sub>O<sub>3</sub> nanocomposites. However, recast layer was observed at some portion of the cut zone due to a series of spark generation and generation of high temperatures between the tool and work [20]. Generation of high temperature during the process can alter the target material properties. The presence of reinforcement particles makes machining of MMC slower by creating difficulties due to the breakage of conductivity caused by non-conductive and high melting points of reinforcement particles. Breaking of wires in WEDM during the process is one of the major problems. Due to high temperature caused between tool and work interface, wire electrode breaks usually in the top edge of the machined surface. Another major limitation of EDM falls in its incapability in cutting non-conductive materials.

LBM uses thermal energy to remove the material using a laser beam by melting and vaporizing. Unlike EDM, LBM is not only limited to conductive materials; it can be applied for a wide range of materials [21]. The major advantage of LBM lies in its capability to produce geometrically complex shapes and miniature holes. LBM have the capability to make slot as low as 0.25 mm width. Generally, machining operations in LBM includes drilling and grooving. Mechanically induced material damage, cutting forces machine vibration, and tool wear are absent in LBM [22]. Machining speed and material removal rate can be increased in LAM. However, an increase in machining speed resulting in a rough surface that splits out into striations is caused by the unsteady motion of molten layer or repeated blockage of plasma. LAM is having its own limitations when machining Mg-based materials, the reflectivity of Mg can result in inadequate heating which limits the cutting capability, and also small chips produced during machining tend to ignite when in contact with the laser beam. Therefore, LBM of thermally sensitive Mg-based materials is risky. Melting of reinforcement material and chemical reactions were reported in LBM of MMC which also affects the microstructure.

AWJM technology is one of the leading and fastest growing NTM technologies for cutting a wide range of materials such as metals, stone, tiles, plastics, FRP, composites, food, ceramics, rubber, etc. In AWJ cutting the impact of solid particles at high velocity along with water at high pressure removes the target material by means of erosion [23]. AWJ uses cold water during the process that eliminates slag deformation and dross waste that is generally found in plasma and laser cutting processes. Additionally, both garnet (abrasive) and water used in the cutting process can be recycled [24]. The AWJM process is therefore environmentally friendly when compared to other cutting processes. The process is also clean and does not involve chips, chemical reactivity, and air pollution. Water jet eliminates dust by carrying away the eroded material and does not generate fumes which are generally present in other NTM processes [25]. In recent years AWJM has received tremendous attention especially in machining difficult to machine and thermally sensitive materials [26, 27]. Due to its versatility, ease of operations and extended capabilities, AWJM has become the hot choice among different machine tools for manufacturing industries. Application areas include automotive, aerospace, construction, medical industries, etc.

Unlike other NTM processes (EDM, LBM/LAM) AWJM does not include higher processing temperatures, and most importantly there is no HAZ [28]. Therefore machined surfaces are neither affected by remelting nor by recrystallization. Thus AWJ cutting technology offers risk-free machining of Mg-based materials by eliminating HAZ. The only drawback of AWJM is lesser efficiency in creating high-quality surfaces which can be expected from the other two methods. Bimla Mardi

et al. [29] investigated the surface integrity of Mg-based nanocomposites generated by AWJ. Feasibility of AWJ in machining Mg-based nanocomposites was reported. Experimental results were analyzed and compared under varied traverse speeds. It was concluded that lower traverse speeds give better surface finish and higher traverse speed results in the poor surface finish. Furthermore, it was concluded that for machining Mg-based MMC, AWJ machining is the most promising method with good surface finish and minimum subsurface damage.

Due to omnidirectional cutting capabilities of AWJM at higher feed rates, it is considered to be the fastest machining option for MMCs [30]. Based on available literature, it can be concluded that even though LAM/LBM and EDM can be efficiently used to machine Mg-based materials, the risk of ignition cannot be avoided. Therefore AWJM is the most suitable and risk-free machining technology for Mg-based materials. Below are some of the distinct advantages of AWJ machining over other methods:

- No heat affected zone.
- Lower setup time.
- No microstructural and microhardness changes occur in the machined surfaces [31].
- No thermal distortion, high machining versatility, and high flexibility [32].
- Simple programming methods.
- High productivity.
- Higher feed rates can be achieved especially in MMC.
- Elimination of dust.

#### **4. AWJ machining operations and process parameters**

AWJ technology is being utilized by many modern industries such as automotive, aerospace, chemical processing, environmental engineering, construction engineering, medical, etc., for performing different operations such as industrial cleaning, surface preparation, paint, enamel and coating stripping, manufacturing operations, etc. Since this chapter is mainly focused on machining aspects, only linear cutting, drilling, turning, and milling machining operations are discussed. AWJM involves a number of process parameters to achieve qualitative and quantitative results. Geometry and quality of the machined surfaces depend mainly on the appropriate selection process parameters. **Table 1** shows detailed AWJ process parameters for different machining operations.

In the present chapter, in order to identify the machining capability of Mg-based materials, experimental investigations on AWJ linear cutting and AWJ drilling operations were carried out. The effect of input parameters on the depth of penetration and surface integrity of AZ91 alloy and nanocomposites was analyzed. AWJ drilling of AZ91 Mg alloy was carried out and compared with conventional and jig boring processes. Overview of AWJ is turning, and AWJ milling operations were discussed. Further research possibilities in AWJ machining Mg-based materials are also highlighted.

AWJ parameters	Machining parameters			
	Linear cutting	Drilling	Milling	Turning
Water pressure	SOD	Angle	TR	Rotational speed
Jet diameter	AOI	SOD	Lateral	Direction of rotation
Abrasive particle size	TS	Dwell time	increment	rotation
Abrasive material	Material	Material	Number of	Angle
Abrasive flow rate	thickness	thickness	passes	Traverse rate
Abrasive condition	Number of		Number of	Initial diameter
Mixing tube length	passes		sweeps	Final diameter
Mixing tube diameter				DOC
Output variables (dependent)				
	DOP	Diameter	VMR	Turned diameter
	Width of cut	Drilling time	Depth control	Surface finish
	Surface finish	Hole shape		Machining time

**Table 1.**  
AWJM process parameters for different operations [33].

### 4.1 AWJ linear cutting

Being most important in industrial applications, depth of penetration and surface quality decides the efficiency, process capability, and performance of AWJ. During past decades theoretical and experimental investigations were made to determine the cutting performance of ductile materials such as aluminum and its alloys, mild steel, stainless steel, copper, brass, etc., with AWJ machining technology [34–36]. However, limited studies are available on AWJ machining of Mg-based materials. Therefore in the present section, experimental investigations were carried out to know the penetration capability and surface quality of AZ91 Mg alloy and nanocomposites by AWJ linear cutting. OMAX 1515 state-of-the-art AWJ machine equipped with 30 Hp direct drive pump to create water pressure ranging 100 MPa to 345 MPa shown in **Figure 1** was used to carry out experiments. The machine also supported with gravity feed-type abrasive hopper and pneumatically controlled three axis movements with traverse speed capacity of 1 mm/min to 8000 mm/min.

AZ91 Mg alloy and nanocomposites with volume percentage of 1, 1.5, and 2% Al<sub>2</sub>O<sub>3</sub> nanoparticles (<50 nm) produced by stir casting were used to conduct experiments. Elemental composition of AZ91 is shown in **Table 2** (obtained by EDS) analysis. **Figure 2** shows EDS spectrum of AZ91-nanocomposites containing 1% Al<sub>2</sub>O<sub>3</sub>.



**Figure 1.**  
State-of-the-art AWJM technology.



Al	Zn	Mn	Si	Cu	Fe	Be	Magnesium
9.41	1.42	0.25	0.03	0.003	0.015	0.001	Rest

**Table 2.**  
*Elemental composition of AZ91 Mg alloy.*

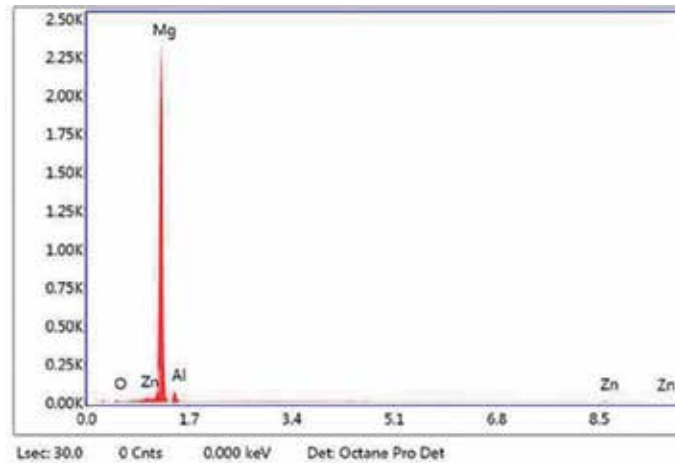


**Figure 2.**  
*EDS spectrum of AZ91/1% Al<sub>2</sub>O<sub>3</sub> nanocomposites.*

#### 4.1.1 Experimental conditions

In the present study, influence of only major dynamic parameters such as water pressure, traverse speed, and abrasive mass flow rate on the depth of penetration and surface integrity is considered. Topography and microstructural features of cut surfaces were examined using SEM technique. All the linear cutting experiments were carried out using standard 80 mesh garnet particles. L18 orthogonal array was used to conduct cutting experiments. Specimen was prepared into trapezoidal shape to make through cuts. This method of making trapezoidal shape is popular among different methods to determine the DOP. Profile projector was used to obtain exact depth of cuts since this method gives accurate values compared to other methods [37]. **Table 3** shows detailed experimental conditions.

#### 4.1.2 Results and discussion

##### 4.1.2.1 Effect of input parameters on the depth of penetration

The effect of control factors such as water pressure, traverse speed, and mass flow rate on the depth of penetration was analyzed by considering mean values of depth of penetration. **Figure 3** shows the effect of input parameters on the depth of penetration in AZ91 magnesium alloy and nanocomposites. It can be observed that depth of penetration increases with an increase in water pressure, due to the increase in kinetic energy of water and abrasive particles with an increase in water pressure. In contrast, more energy of the particles as well as water was able to remove more material. It is also observed that, when compared to AZ91 Mg alloy, penetration ability of Mg nanocomposites decreases with increase in vol. % of Al<sub>2</sub>O<sub>3</sub>, since MMCs offer resistance to the jet penetration due to the presence of harder nanoceramic particles.

Dynamic parameters				
Water pressure ( $P_w$ )	Unit	Level 1	Level 2	Level 3
	MPa	100	200	300
Traverse speed ( $t_s$ )	mm/min	150	300	400
Mass flow rate ( $m_f$ )	g/min	309	425	611
Constant parameters				
Abrasive mesh size		80		
Orifice (jewel) diameter	mm	0.35 and material is sapphire		
Focusing nozzle diameter	mm	0.76 and material is tungsten carbide		
Angle of target		90°		
Standoff distance	mm	1.5		

**Table 3.**  
Detailed machining conditions selected for cutting experiments.

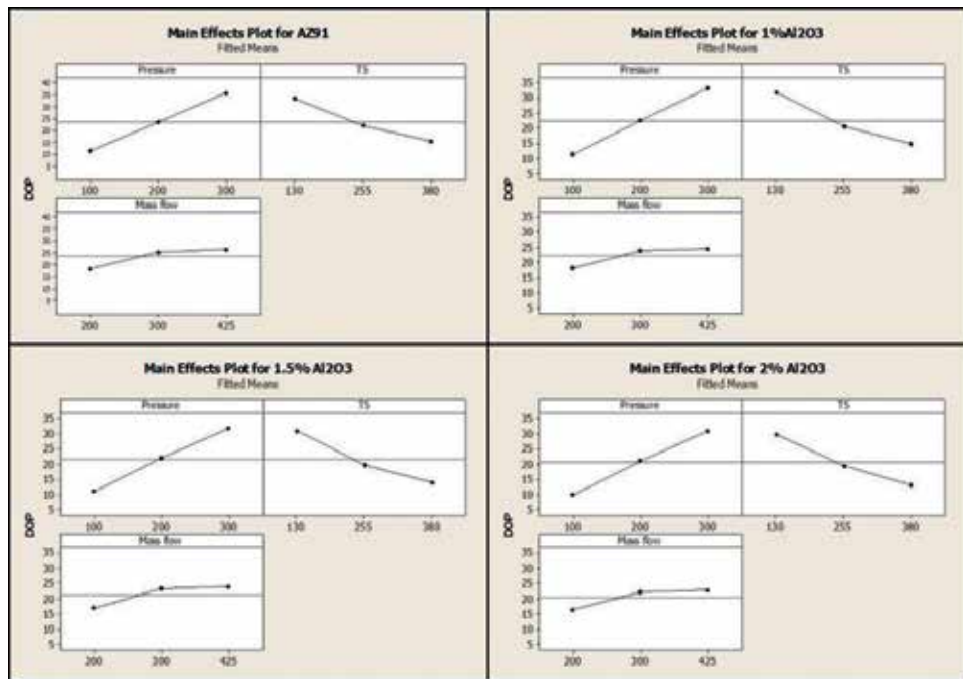


**Figure 3.**  
Effect of input parameters on depth of penetration.

Relationship between traverse speed and depth of penetration indicates that increasing the traverse speed lowers the impact of numbers of abrasive particles and results in decreasing the depth of penetration. The influence of traverse speed on the depth of penetration, therefore, lies on the exposure time of abrasive water jet. The lesser the exposure time, the more the depth of penetration. The effect of mass flow rate on the depth of penetration indicating an increase in abrasive mass flow increases the depth of penetration due to the participation of large number of abrasive particles in cutting. This trend remains stable till the value of mass flow rate reaches to a critical level. After that depth of penetration decreases since the higher abrasive flow rates sometimes block the nozzle and at higher abrasive mass

flow rates. Due to some damping mechanisms such as generation of water-solid films and abrasive particles, collision in mixing chamber significantly reduces the specific energy of abrasive particles [38]. It is evident from the previous studies that the velocity of abrasive particles decreases with an increase in abrasive mass flow rate [39–41]. This reduces the depth of penetration.

#### 4.1.3 Topography of cut surfaces

Literatures have witnessed solid particle impact in the material removal process by abrasive water jets by erosion [42]. In ductile materials, material removal process is divided into two zones such as micro cutting zone observed at the top surface and deformation zone, which occurs at the bottom surface [43]. Similar observations were noted down in surfaces of MMC [44]. In the micro cutting region, material removal takes place by sharp-edged and angular abrasive particles at low cutting depths. Impact of the abrasive particles at shallow angles promotes micro cutting, termed as “cutting wear.” At larger cutting depths, the impact angle of abrasive particles becomes more obtuse and causes “deformation wear.” Plowing is responsible for material removal in the bottom region due to spherical abrasive particles [45]. Deformation wear zone is affected by surface waviness caused due to instabilities of the water jet. Loss of jet energy reduces the capacity of material removal creating waviness and thus dividing cutting and deformation wear zones as shown in **Figure 4**.

#### 4.1.4 Integrity of the cut surfaces

A surface characteristic of cut surfaces is evaluated in two regions, i.e., smooth cutting zone (SCZ) and rough cutting zone (RCZ) as shown in **Figure 5** [46, 47]. Surface integrity of cut surfaces can be obtained by measuring surface roughness in both regions using either a contact-type or noncontact-type measuring device. Most of the researchers have used optical profiler for measuring surface roughness which is the noncontact type. Several researchers have used contact-type roughness measuring devices, which use a stylus tip to measure waviness of the surface.

In the SCZ, initially the surfaces are clear and smooth but affected by the formation of uniform wear tracks in the direction of the jet traverse at the bottom portion of the SCZ. Since this zone is shared by both micro cutting and deformation modes, surface roughness increases further down the surfaces. In RCZ the surface roughness is affected by striations caused by deflected water jet. **Figure 5** shows the presence of deviated wear tracks with waviness produced by a stream of the

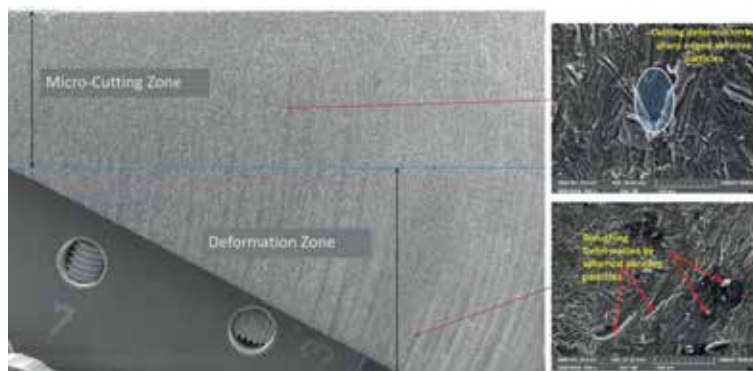


**Figure 4.**  
*Material removal mechanism.*

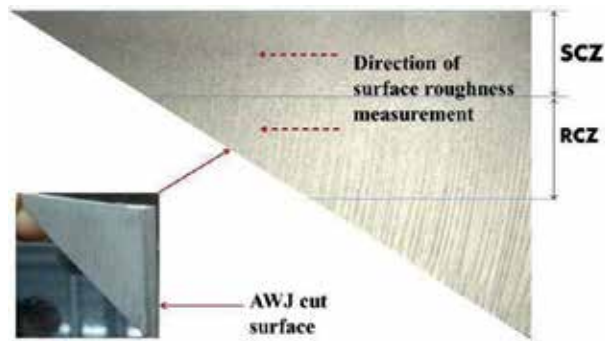


**Figure 5.**  
Regions of cut surfaces.

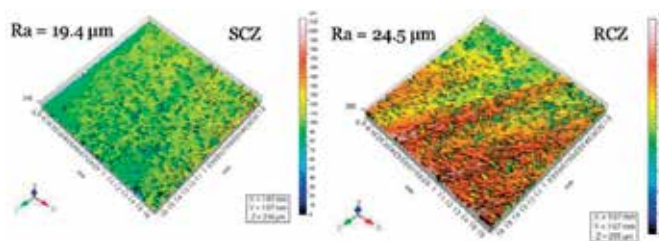


**Figure 6.**  
3-D images of SCZ and RCZ.

deflected water jet. In cutting AZ91 magnesium alloy, the embedment of spherical abrasive particles and pocket-like structures is observed at the shallow impact angles as shown in **Figure 4**. The surface roughness at RCZ zone is higher than SCZ zones. **Figure 6** shows the 3-D images of SCZ and RCZ generated in optical profiler.

The surface roughness of the AZ91 and nanocomposites in the SCZ zones is found between 5–20  $\mu\text{m}$  and 20–40  $\mu\text{m}$  in RCZ at lower traverse speeds. This is due to the increase in the impact of a number of abrasive particles and exposure time. Surface roughness is a function of water pressure because the kinetic energy of water jet increases the velocity of particles which in turn increases the surface quality, and also the influence of abrasive mass flow rate on surface roughness depends mainly on water pressure. However, at higher traverse speeds, an increase in water pressure increases the surface roughness. Hence traverse rate is the most significant parameter in deciding the quality of cut at two zones.

#### 4.2 AWJ drilling

Earlier studies have proven that AWJ technology is a viable tool for drilling different materials such as pure commercial aluminum, Al6061, brass, S1030 low-carbon steel, D-3 cold working tool steel, etc. AWJ drilling does not affect microhardness and mechanical properties of the material [48]. Burr-free surfaces can be obtained in AWJ drilling. Drilling at different angles is also quite convenient with AWJ. In AWJ technology drilling can be performed by tilting the cutting head up to 590. Though many types of research are carried out in drilling different materials, no work has been notably reported on drilling of Mg-based materials through AWJ technology. In the present section, experimental investigations are carried out to know the features of holes drilled by AWJ in Mg alloy. Surface roughness and taper of drilled holes are measured and compared with holes drilled by conventional drilling and jig boring.

Method	Hole dia	φ 3 mm	φ 5 mm	φ 10 mm	φ 15 mm	φ 20 mm
↓ Drilling conditions						
AWJM	P	300 MPa constant for all holes				
	M <sub>f</sub>	425 g/min constant for all holes				
	SOD	1.5 mm constant for all holes				
	Time in min	2.5	3.5	5.4	6	7.9
Conventional drilling	Speed	1200 rpm	1100 rpm	1000 rpm	900 rpm	800 rpm
	Feed	0.1 mm/rev: constant for all holes				
	Time in min	3	2.5	1.5	1.5	1.5
Jig boring	Speed	1200 rpm	1100 rpm	1000 rpm	900 rpm	800 rpm
	Feed	0.1 mm/rev: constant for all holes				
	Time in min	2.9	2.3	1	1	1

**Table 4.**  
 Conditions for drilling holes.

Five holes with diameter 3, 5, 10, 15, and 20 mm were drilled in 40 mm thick AZ91 Mg alloy block. Roundness and taper of drilled holes were obtained using profile projector. Drilling time of each hole was also determined and compared. The conditions at which the holes were drilled are given in **Table 4**.

**Table 5** gives actual dimensions of five holes drilled by different methods measured using a profile projector with taper percentage. Diameters of drilled holes were measured in both sides (top and bottom) to know the variations in drilled holes. It can be observed that compared to holes drilled by conventional methods, AWJ-drilled holes were affected by the taper. The taper was comparatively higher in drilling less than 5 mm hole. This is due to hit back of jet from the channel during the drilling process, and this trend will last until full penetration is achieved. Meanwhile, the base hole will be abraded by the perimeter of the jet and thus affects the shape (roundness) and diameter of the hole as shown in **Figure 7**. When compared to other methods, AWJ-created holes are slightly larger than the required size and require comparatively more time to drill holes.

**Figure 8** shows a cross section of holes drilled in AZ91 Mg block using three different methods. The surface roughness of drilled surfaces with diameter 10, 15, 20 mm were measured using contact-type Taylor and Hobson surface roughness measuring instrument by considering 5 mm cutoff length. Measurement was taken in three regions of the depth (top-middle-bottom) of drilled surfaces. The average of three readings in each zone is noted down. **Table 6** gives surface roughness (Ra) of drilled surfaces.

Desired $\Phi$	Conventional		Taper %	Jig boring		Taper %	AWJ		Taper %
	$\Phi$ at top	$\Phi$ at bottom		$\Phi$ at top	$\Phi$ at bottom		$\Phi$ at top	$\Phi$ at bottom	
2.5	2.384	2.451	0.17	2.375	2.435	0.15	3.526	2.321	3.012
5	5.129	4.955	0.44	4.930	5.071	0.35	5.841	5.263	1.445
10	9.960	9.981	0.05	10.013	10.069	0.13	10.555	10.161	0.985
15	14.796	15.133	0.84	14.790	15.196	1.09	15.375	15.021	0.885
20	19.549	20.211	1.66	19.867	20.207	0.85	20.355	20.100	0.637

**Table 5.**  
*Dimensions and taper percentage of drilled holes.*



**Figure 7.**  
*Roundness of holes produced by AWJ.*

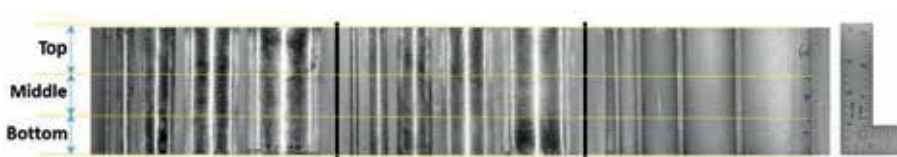


**Figure 8.**  
*Cross section of drilled holes.*

Measurement zone	Conventional	Jig boring	AWJ
Top (0–13 mm)	2.65 $\mu\text{m}$	0.93 $\mu\text{m}$	3.96 $\mu\text{m}$
Middle (14–26 mm)	3.99 $\mu\text{m}$	1.48 $\mu\text{m}$	4.47 $\mu\text{m}$
Bottom (26–40 mm)	4.30 $\mu\text{m}$	1.57 $\mu\text{m}$	5.09 $\mu\text{m}$

**Table 6.**  
*Ra of drilled surfaces measured in different depths.*



**Figure 9.**  
*Adhesion of material to the drill bit.*

From **Table 6**, it can be observed that the surface roughness of AWJ-drilled holes is more than the other two methods in all the regions. Surface roughness increases with increase in depth. This is due to loss of jet energy and a decrease in cutability of the abrasive particles at higher depths and thus deteriorates the surface quality. However comparable results can be achieved by AWJ technology when compared to conventional drilling. Despite few drawbacks, AWJ drilling offers several advantages over other methods. No burrs are observed in the AWJ-drilled surfaces, unlike conventional methods. Adhesion of the material to the drill bit, especially in drilling less than 5 mm diameter holes, is observed in both conventional methods as shown in **Figure 9**. Formation of FBU increases heat generation during drilling. This tendency of the Mg-based materials to adhere to the drill bits is a serious problem. Formation of FBU is completely absent in AWJ drilling since there is no direct contact between tool and work. Therefore risk-free drilling is possible through AWJ technology.

## 5. Other alternative operations with AWJ

The versatility of AWJ technology makes it suitable for cutting almost all engineering materials. Besides cutting and drilling of materials as discussed in the previous section, AWJ technology has been successfully implemented to perform some of the essential machining operations such as turning, milling, finishing, and piercing. Several investigations are carried out on these machining operations with promising results. Thus AWJ technology has become a potential machine tool for modern machining industries. This section highlights the suitability of AWJ in turning and milling operations based on past studies. Research possibilities in AWJ technology are also discussed.

### 5.1 AWJ turning

In AWJ turning, workpiece is rotated while the jet is traversed parallel to the axis of workpiece to produce the required shape. Research efforts on AWJT were started by Hashish during 1987; since then several experimental investigations on different machining operations were made to produce near net shape parts with faster material

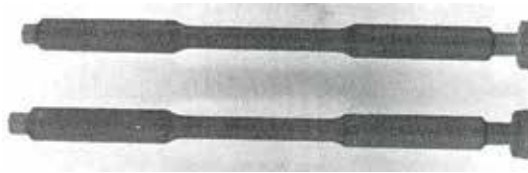


**Figure 10.**  
*Tensile specimens produced by AWJ in Mg-B<sub>4</sub>C MMC [49].*

removal rate [49]. Investigations on samples of Mg-boron carbide MMC, glass, and aluminum concluded suitability of AWJ for performing alternative machining operations.

Preliminary investigations on AWJT has revealed that AWJ turning is less sensitive to the type of material being machined unlike conventional machining, no microstructural changes were observed on AWJ machined surfaces, tensile properties of cylindrical specimens turned by AWJ remains unaffected, and relative insensitivity of AWJ to length-to-diameter ratio of work piece enables the process to turn long and small diameter components. **Figure 10** shows the tensile test Mg-B<sub>4</sub>C MMC specimens produced by AWJT. No appreciable microhardness changes were observed during turning of Mg-B<sub>4</sub>C MMC and aluminum. No ignition issues were observed during machining.

Investigations conducted by the University of Rhode Island [50, 51] have witnessed machining of screw threads on composite materials. Furthermore, it was revealed that a thread produced by AWJ has an excellent potential to provide sufficient joint strength when compared to adhesive bonded joints. Minimal structural damage on machined surfaces was observed during microstructural examinations. Still there are plenty of research opportunities which are open in AWJT field to expand the applications of AWJ in different areas. Detailed studies on AWJT economics, a wide range of machining parameters, and multi-objective optimization still need to be considered in order to make AWJT the most economical and alternative tool for machining.

## 5.2 AWJ milling

Milling is one of the important alternative machining operations that can be performed by AWJ. AWJ milling has been systematically utilized where conventional machining of material is insufficient to apply. The capability of AWJ in cutting complex shapes with controlled depth has witnessed the success of AWJ milling. Recent studies have proven AWJ technology as the best alternative for milling manufacturing standard flat tensile specimens [52]. In earlier days conventional milling was the only method which was accepted internationally for manufacturing of standard sheet-type tensile specimens. Drawbacks of conventional milling in manufacturing flat tensile specimens, such as difficulties in clamping of thin sheets, requirement of milling tool with same diameter as filler radii of the tensile specimen, contouring several times to obtain desired shapes etc., have created circumstances to choose alternative nontraditional methods [53].

Advantages such as lesser manufacturing time, reasonable material removal rate, and minimal deformation stress made AWJ milling a viable alternative for conventional milling. Feasibility of AWJ in milling was first proposed by Hashish in 1989 [54]. Investigations on volume removal rates and surface finish of different materials such as titanium, aluminum, and Inconel were made through linear cutting experiments. Cutting parameters such as traverse speed, number of passes, etc. were varied at different levels. Results were compared with other methods, and some of the critical observations noted from the results are listed below:





**Figure 11.** Profile of helical gear produced by AWJ (a) logo in AM60 Mg alloy, (b) spur gear profile in AM60 Mg alloy, and (c) cast iron helical gear profile.

- Waterjet nozzles that are used for slot cutting are sufficient to do milling operations.
- Reasonable material removal rates can be achieved by AWJ milling with relatively low power levels.
- AWJ machining is environmentally acceptable and safe.
- In terms of energy utilization for material removal, AWJ milling is the most efficient method over other methods.

**Figure 11** shows some of the complex shapes (a) and profiles of helical (b) and spur gear (c) produced by AWJ milling.

## 6. Conclusion

Present study gives comprehensive overview of abrasive water jet cutting technology for machining Mg-based materials and Mg-MMCs. Penetration capability of AZ91 and Mg nanocomposites was investigated through linear cutting experiments. Drilling of holes with different sizes in AZ91 was performed using conventional drilling and jig boring and compared with holes drilled by AWJ. These experimental investigations on machining operations such as linear cutting and drilling have revealed suitability and capability of AWJ. The present study also highlighted the application areas of AWJ in milling and turning of different materials including MMCs. However experimental investigations made in the present study was preliminary and requires detailed process economics, optimization, and comparative studies to extend and explore research possibilities. Performance, capability, and applications of AWJ in machining different grades of Mg and Mg-MMC can be further extended with the use of advanced modeling techniques.

Based on preliminary studies on linear cutting and drilling operations, the following conclusions can be made:

- Pressure remains dominant in deciding depth of cut in both AZ91 Mg alloy and nanocomposites. Traverse speed decides the quality of cut generated by water jets. The lower the traverse speed, the higher the surface quality, and surface quality deteriorates with increase in traverse speed. The abrasive mass flow rate has the least effect on both penetration and surface quality. Similar observations are obtained in machining different ductile materials with AWJ.
- Drilling of AZ91 Mg alloy also revealed acceptable results when compared to conventional drilling and jig boring. No fire ignition issues aroused during both machining operations. The use of profile projector is found to be the accurate and straightforward way of finding the depth of penetration in linear cutting operations and obtaining roundness of AWJ-drilled holes.
- Apart from linear cutting, AWJ can be successfully utilized for other machining operations such as milling and turning of Mg-based materials. Complex shapes and profiles of different types of gears can be easily produced by AWJ with lesser time compared to other NTM and conventional methods.
- AWJ machining of Mg-based materials is the less studied area. Primary results presented in the chapter contribute to the optimization of AWJ process in machining Mg-based materials.
- Overall it can be concluded that AWJM technology could be ideal for flexible and risk-free machining of Mg-based materials and Mg-MMCs.

## **Acknowledgements**

We would like to thank TEQIP-BMS College of Engineering, Bengaluru, for providing materials, research facilities to conduct experiments, and financial assistance in publishing this chapter. We want to express our sincere gratitude and appreciation to Mr. Venkatesh Ramamurthy, Deputy Manager, Robert Bosch India, Bengaluru; Mr. Vikarm Kumar S Jain, Research Scholar, Dept. of Metallurgical and Materials Engg. National Institute of Technology, Tiruchirappalli, Tamilnadu; and Ms. Madhuri P Rao Research Scholar, Dept. of Chemistry, BMS College of Engineering, Bengaluru, for their invaluable support in completing this project. We also wish to express heartfelt thanks to Gopalakrishna S S for the Photoshop works seen in this work.

## **Nomenclature**

ECAP	equal channel angular pressing
CAGR	compound annual growth rate
FBU	flank buildup
BUE	built-up edge
MMC	metal matrix composite
NTM	nontraditional machining
LBM	laser beam machining
LAM	laser-assisted machining

WEDM	wire electric discharge machining
EDM	electric discharge machining
AWJM	abrasive water jet machining
HAZ	heat-affected zone
SOD	standoff distance
AOI	angle of impact
DOP	depth of penetration
DOC	depth of cut
VMR	volume material removal
EDS	energy-dispersive spectroscopy
SCZ	smooth cutting zone
RCZ	rough cutting zone

## Symbols


$P_w$	water pressure
$t_s$	traverse speed
$m_f$	mass flow rate
$L$	length of cut
$h_t/d_p$	depth of penetration
$\theta$	wedge angle
$\phi$	diameter

## Author details

Niranjan Channagiri Anandathachar\*, S. Srinivas and M. Ramachandra  
Department of Mechanical Engineering, BMS College of Engineering, Bengaluru,  
Karnataka, India

\*Address all correspondence to: [niranjancaster@gmail.com](mailto:niranjancaster@gmail.com)

## IntechOpen

© 2019 The Author(s). Licensee IntechOpen. This chapter is distributed under the terms of the Creative Commons Attribution License (<http://creativecommons.org/licenses/by/3.0/>), which permits unrestricted use, distribution, and reproduction in any medium, provided the original work is properly cited. 

## References

- [1] <https://www.prnewswire.com/news-releases/global-magnesium-market-report-2018-market-to-grow-at-a-cagr-of-5-92-to-2022--300656511.html>
- [2] Weinert K, Inasaki I, Sutherland JW, Wakabayashi T. Manufacturing technology: Dry machining and minimum quantity lubrication. *CIRP Annals*. 2004;**53**(2):511-537. DOI: 10.1016/S0007-8506(07)60027-4
- [3] Denkena B, Witte F, Podolsky C, Lucas A. Degradable implants made of magnesium alloys. In: *Proceedings of 5th Euspen International Conference Montpellier France; May 2005*
- [4] Mebarki N, Kumar NVR, Blandin JJ, Suery M, Pelloux F, Khelifati G. Correlations between ignition and oxidation behaviours of AZ91 magnesium alloys. *Materials Science and Technology*. 2005;**21**(10):1145-1151. DOI: 10.1179/174328405X58904
- [5] Rao J, Li H. Oxidation and ignition behavior of a magnesium alloy containing rare earths elements. *International Journal of Advanced Manufacturing Technology*. 2010;**51**(1-4):225-231. DOI: 10.1007/s00170-010-2612-8
- [6] Kumar NVR, Blandin JJ, Suéry M, Grosjean E. Effect of alloying elements on the ignition resistance of magnesium alloys. *Scripta Materialia*. 2003;**49**(3):225-230. DOI: 10.1016/S1359-6462(03)00263
- [7] Tönshoff HK, Winkler J. The influence of tool coatings in machining of magnesium. *Surface and Coatings Technology*. 1997;**94-95**:610-616. DOI: 10.1016/S0257-8972(97)00505-7
- [8] Zhao N, Hou J, Chip SZ. Ignition in research on high-speed face milling AM50A magnesium alloy. In: *Second International Conference on Mechanic Automation and Control Engineering, Hohhot; 2011*. pp. 1102-1105. DOI: 10.1109/MACE.2011.5987127
- [9] Sreejith PS, Ngoi BKA. Dry machining: Machining of future. *Journal of Materials Processing Technology*. 2000;**101**(1-3):287-291. DOI: 10.1016/S0924-0136(00)00445-3
- [10] Carou D, Rubio EM, Lauro CH, et al. Experimental investigation on finish intermittent turning of UNS M11917 magnesium alloy under dry machining. *International Journal of Advanced Manufacturing Technology*. 2014;**75**:1417-1429. DOI: 10.1007/s00170-014-6215-7
- [11] Rubio EM, Villeta M, Carou D, et al. Comparative analysis of sustainable cooling systems in intermittent turning of magnesium pieces. *International Journal of Precision Engineering and Manufacturing*. 2014;**15**:929-940. DOI: 10.1007/s12541-014-0419-5
- [12] Bhowmick S, Lukitsch MJ, Alpas AT. Dry and minimum quantity lubrication drilling of cast magnesium alloy (AM60). *International Journal of Machine Tools and Manufacture*. 2010;**20**(5):444-457. DOI: 10.1016/j.ijmachtools.2010.02.001
- [13] Gariboldi E. Drilling a magnesium alloy using PVD coated twist drills. *Journal of Material Processing Technology*. 2003;**134**:287-295. DOI: 10.1016/S0924-0136(02)01111-1
- [14] Lapovok R, Molotnikov A, Levin Y, Bandaranayake A, Estrin Y. Machining of coarse grained and ultra-fine grained titanium. *Journal of Materials Science*. 2012;**47**:4589-4594. DOI: 10.1007/s10853-012-6320-7
- [15] Bains PS, Sidhu SS, Payal HS. Fabrication and machining of

metal matrix composites: A review. *Materials and Manufacturing Processes*. 2016;**31**(5):553-573. DOI: 10.1080/10426914.2015.1025976

[16] Li J, Liu J, Liu J, Ji Y, Xu C. Experimental investigation on the machinability of SiC nano-particles reinforced magnesium nano composites during micro-milling processes. *International Journal of Manufacturing Research*. 2003;**8**(1). DOI: 10.1504/IJMR.2013.051840

[17] Teng X, Huo D, Wong E, et al. Micro-machinability of nanoparticle-reinforced Mg-based MMCs: An experimental investigation. *International Journal of Advanced Manufacturing Technology*. 2016;**87**:2165. DOI: 10.1007/s00170-016-8611-7

[18] Rubio EM, Valencia JL, Carou D, Saá A. Inserts selection for intermittent turning of magnesium pieces. *Applied Mechanics and Materials*. 2012; **217-219**:1581-1591. DOI: 10.4028/www.scientific.net/AMM.217-219.1581

[19] Ho KH, Newman ST. State of the art electrical discharge machining (EDM). *International Journal of Machine Tools and Manufacture*. 2003;**43**(13):1287-1300. DOI: 10.1016/S0890-6955(03)00162-7

[20] Ponappa K, Aravindan S, Rao PV, et al. The effect of process parameters on machining of magnesium nano alumina composites through EDM. *International Journal of Advanced Manufacturing Technology*. 2010;**46**:1035. DOI: 10.1007/s00170-009-2158-9

[21] Dubey AK, Yadava V. Laser beam machining—A review. *International Journal of Machine Tools and Manufacture*. 2008;**48**(6):609-628. DOI: 10.1016/j.ijmachtools.2007.10.017

[22] Pramanik A. Developments in the non-traditional machining of particle reinforced metal matrix composites.

*International Journal of Machine Tools and Manufacture*. 2014;**86**:44-61. DOI: 10.1016/j.ijmachtools.2014.07.003

[23] Shanmugam D, Chen F, et al. Comparative study of jetting machining technologies over laser machining technology for cutting composite materials. *Composite Structures*. 2002;**57**(1):289-296. DOI: 10.1016/S0263-8223(02)00096-X

[24] <https://www.flowwaterjet.com/Learn/Benefits-of-Waterjet.aspx#accuracy>

[25] Kulekci MK. Processes and apparatus developments in industrial waterjet applications. *International Journal of Machine Tools and Manufacture*. 2002;**42**(12):1297-1306. DOI: 10.1016/S0890-6955(02)00069-X

[26] Ramulu M, Arola D. Waterjet and abrasive waterjet cutting of unidirectional graphite/epoxy composite. *Composites*. 1993;**24**(4):299-308. DOI: 10.1016/0010-4361(93)90040-F

[27] Kovačević R, Hashish M, Mohan R, Ramulu M, Kim TJ, Geskin ES. State of the Art of Research and Development in Abrasive Waterjet Machining. *Journal of Manufacturing Science and Engineering* 1997;**119**(4B):776-785. DOI: 10.1115/1.2836824

[28] Hashish M. Characteristics of surfaces machined with abrasive-waterjets. *Journal of Engineering Materials and Technology*. 1991;**113**(3):354-362. DOI: 10.1115/1.2903418

[29] Bimla Mardi K, Dixit AR, Mallick A, Pramanik A, Balloková B, Hvizdos P, et al. Surface integrity of Mg-based nanocomposite produced by abrasive water jet machining (AWJM). *Materials and Manufacturing Processes*. 2017;**32**(15):1707-1714. DOI: 10.1080/10426914.2017.1279306

- [30] Hashish M. Water jet machining of advanced composites. *Materials and Manufacturing Processes*. 1995;**10**(6):1129-1152. DOI: 10.1080/10426919508935098
- [31] Van Luttervelt CA. On the selection of manufacturing methods illustrated by an overview of separation techniques for sheet. *CIRP Annals*. 1989;**38**(2):587-607. DOI: 10.1016/S0007-8506(07)61127-5
- [32] Savrun E, Taya M. Surface characterization of SiC whisker/2124aluminium and Al<sub>2</sub>O<sub>3</sub> composites machined by abrasive water jet. *Journal of Materials Science*. 1998;**23**(4):1453-1458. DOI: 10.1007/BF01154616
- [33] Hashish M. Three-dimensional machining with abrasive-Waterjets. In: Lichtarowicz A, editor. *Jet Cutting Technology. Fluid Mechanics and its Applications*. Dordrecht: Springer; 1992. pp. 605-620. DOI: 10.1007/978-94-011-2678-6\_40
- [34] Mat Deris A, Mohd Zain A, Sallehuddin R. Hybrid GR-SVM for prediction of surface roughness in abrasive water jet machining. *Meccanica*. 2013;**48**:1937-1945. DOI: 10.1007/s11012-013-9710-2
- [35] Iqbal A, Dar NU, Hussain G. Optimization of abrasive water jet cutting of ductile materials. *Journal of Wuhan University of Technology*. 2011;**26**(1):88-92. DOI: 10.1007/s11595-011-0174-8
- [36] Akkurt A. *Journal of Materials Engineering and Performance*. 2010;**19**:599. DOI: 10.1007/s11665-009-9513-8
- [37] Niranjan CA, Srinivas S, Ramachandra M. Proceedings: An experimental study on depth of cut of AZ91 magnesium alloy in abrasive water jet cutting. *Materials Today*. 2018;**5**(1, 3):2884-2890. DOI: 10.1016/j.matpr.2018.01.082
- [38] Momber AW, Eusch I, Kovacevic R. *Journal of Materials Science*. 1996;**31**:6485. DOI: 10.1007/BF00356252
- [39] Chen WL, Geskin ES. *Jet Cutting Technology-Proceedings of the 10th International Conference*. Elsevier Science Publishers Ltd; 1990. pp. 23-36
- [40] Wallis GB. *One-Dimensional Two-Phase Flow*. New York NY: McGraw-Hill; 1969. p. 431
- [41] Himmelreich U, Rie W. *Laser-Velocimetry*. Vol. 1. St. Louis: Water Jet Technology Association; 1991. pp. 359-371
- [42] Finnie I. The mechanism of erosion of ductile metals. In: Haythomthwaite RM et al., editors. *1958 Proc. 3rd U.S. Nat. Congr. Appl. Mech*. New York: ASME. pp. 527-532
- [43] Neusen KF, Rohatgi PK, Vaidyanathan C, et al. Abrasive waterjet cutting of metal matrix composites. In: Hood M, Dornfeld D eds. *1987 Proc. 4th U.S. Water Jet*
- [44] Bitter JGA. A study of erosion phenomena—Part I. *Wear*. 1963;**6**:5-21. DOI: 10.1016/0043-1648(63)90003-6
- [45] Hutchings IM. Mechanical and metallurgical aspects of the erosion of metals. In: Levy AV, editor. *Proc. Corrosion/Erosion of Coal Conversion System Material*. Houston: Con, Nat Ass. Corr. Engrs.; 1979. pp. 393-428
- [46] Arola D, Ramulu M. Abrasive waterjet machining of titanium alloy. In: Labus TJ, editor. *Proceedings of 8th American Water Jet Conference*. St. Louis: Water Jet Technology Association; 1995. pp. 389-408
- [47] Hloch S, Valíček. Topographical anomaly on surfaces created by abrasive waterjet. *The International Journal of*

Advanced Manufacturing Technology.  
2012;**59**:593-604. DOI: 10.1007/  
s00170-011-3511-3

[48] Akkurt A. The effect of material type and plate thickness on drilling time of abrasive water jet drilling process. *Materials & Design*. 2009;**30-3**:810-815. DOI: 10.1016/j.matdes.2008.05.049

[49] Hashish M. Turning with abrasive-waterjets—A first investigation. *Journal of Engineering for Industry*. 1987;**109**(4):281-290. DOI: 10.1115/1.3187130

[50] Sheridan M, Taggart DG, Kim TJ. Screw thread machining of composite materials using abrasive waterjet cutting. *Manufacturing Science and Engineering*. 1994;**68-1**:421-432

[51] Sheridan M, Taggart DG, Kim TJ, Wen Y. Microstructural and mechanical characterization of threaded composite tubes machined using AWJ cutting. In: *Proc. 8th American Water Jet Conference*; Houston, TX; 26-29 August 1995; pp. 245-258

[52] Martinez Kraemer D, Polvorosa R, López LN, et al. Alternatives for specimen manufacturing in tensile testing of steel plates. *Experimental Techniques*. 2016;**40**:1555-1565. DOI: 10.1007/s40799-016-0134-5

[53] Martinez Kraemer D. El proceso de corte láser aplicado a la manufactura de probetas planas de tracción normalizadas obtenidas a partir de chapas finas de acero galvanizadas. *Congreso Conamet/ Sam Simposio Materia*, Santiago de Chile. 2002. pp 389-393

[54] Hashish M. An investigation of milling with abrasive-waterjets. *Journal of Engineering for Industry*. 1989;**111**(2):158-166. DOI: 10.1115/1.3188745





# Dissimilar Welding and Joining of Magnesium Alloys: Principles and Application

*Kavian O. Cooke, Abdulaziz Alhazaa and Anas M. Atieh*

## Abstract

The growing concerns regarding fuel consumption within the aerospace and transportation industries make the development of fuel-efficient systems a significant engineering challenge. Currently, materials are selected because of their abilities to satisfy engineering demands for good thermal conductivity, strength-to-weight ratio, and tensile strength. These properties make magnesium an excellent option for various industrial or biomedical applications, given that is the lightest structural metal available. The utilization of magnesium alloys, however, requires suitable welding and joining processes that minimizes microstructural changes while maintaining good joint/bond strength. Currently, magnesium are joined using; mechanical fastening, adhesive bonding, brazing, fusion welding processes or diffusion bonding process. Fusion welding is the conventional process used for joining similar metals. However, the application of any welding technique to join dissimilar metals presents additional difficulties, the principal one being; the reaction of the two metals at the joint interface can create intermetallic compounds that may have unfavorable properties and metallurgical disruptions which deteriorates the joint performance. This chapter investigates the welding and joining technologies that are currently used to join magnesium alloys with emphasis on the development of multi-material structures for applications in the biomedical industries. Multi-material structures often provide the most efficient design solution to engineering challenges.

**Keywords:** magnesium, solid-state diffusion bonding, friction stir welding, dissimilar joining, transient liquid phase

## 1. Introduction

The interest in the use of lightweight materials and alloys has significantly increased in recent years due to excellent mechanical and chemical characteristics; such as high specific strength, low weight, and corrosion resistance. Magnesium is a popular industrial metal and it is the lightest of all, estimated to be 33% lighter than aluminum and ~75% lighter than steel, with a density of  $1.74 \text{ g/m}^3$  [1]. Magnesium has a hexagonal closed pack (HCP) crystalline structure that resists the slip to parallel basal planes and therefore, magnesium cannot be plastically deformed at room temperature, because the work hardening rate is high, and ductility is low. Therefore, magnesium alloys are formed above  $226^\circ\text{C}$  with a range of  $343\text{--}510^\circ\text{C}$  as

the slip process becomes easier at elevated temperatures. Anisotropy during deformation is the other consequence of the HCP structure in cold-formed sheets.

The industrial and biomedical demand for components made from light-weight materials have only increased over the last decade [1]. In its pure state, magnesium is ductile and possesses low tensile strength in the range of 20 MPa. Engineering applications, however, require greater strength as such magnesium is frequently alloyed with elements such as Al, Mn, Zn, Li, Ag, Ca and Cu along with various minor alloying elements. The utilization of magnesium alloys has seen an increase at the rate of 15% and is predicted to go even higher over the next decade. Currently, magnesium is used widely as a structural material due to low density and favorable damping characteristics, low casting costs and machinability [2]. However, new magnesium alloys are being developed with enhanced corrosion resistance and enable these materials to operate satisfactorily inside the human body. The corrosion resistance of these materials has been shown to be inversely proportional to the volume of impurity (Fe, Ni, and Cu) present in the alloy. Currently, the high purity ZX50 Mg alloy and high purity Mg-Al alloys have shown the greatest degree of success.

A major challenge in using these materials is the unavailability of suitable welding technique capable of both similar and dissimilar welding of magnesium alloys [3]. Currently, magnesium alloys used in dissimilar welding processes are joined by resistance spot welding, laser welding, friction stir welding, and diffusion bonding. Extensive research has been devoted to the development of technologies capable of joining these alloys while preventing significant microstructural changes commonly observed during fusion welding of advanced composites. This chapter will investigate welding and joining technologies which are currently used to join magnesium alloys with emphasis on diffusion bonding as a technique for the development of multi-material structures for applications in the biomedical industries. Multi-material structures often provide the most efficient design solution to engineering challenges. The use of several metals in the construction of multi-material structures is limited by the ability of the available welding/joining technologies to join dissimilar materials together.

## **2. Welding metallurgy of magnesium alloys**

Fusion welding of magnesium alloys has been studied using several technologies which include; gas tungsten arc welding (TIG), gas metal arc welding (MIG), laser welding and ultrasonic welding. During TIG welding, an arc is produced between a non-consumable electrode and the workpiece, which melts the base metal to form a weld/joint as shown in **Figure 1**. The joint and surrounding areas can be divided into regions consisting of the weld pool (with a cast structure) and a heat affected zone (HAZ). The microstructural changes within these regions occur due to the temperature gradient from the weld pool to the base metal alloy as shown in **Figure 2**. Shielding flux either in solid or gaseous form is required to protect the weld pool from exposure to oxygen.

TIG welding is considered as the most preferred industrial welding method for reactive materials such as magnesium; this is attributed to better economy and applicability, which makes it an excellent choice for joining magnesium and its alloys. Previous work on joining Mg alloys showed that TIG welding may result in a joint strength of up to 94% of the shear strength of the Mg base metal alloy. However, grain size variation from 6 to 23  $\mu\text{m}$  occurred, across the weld pool, heat affected zone (HAZ) region, and Mg base metal alloy, when TIG welding is applied without a filler wire [4]. On the other hand, Peng et al. [5] showed that dissimilar joining of magnesium alloys AZ31 and AZ61 using TIG welding can

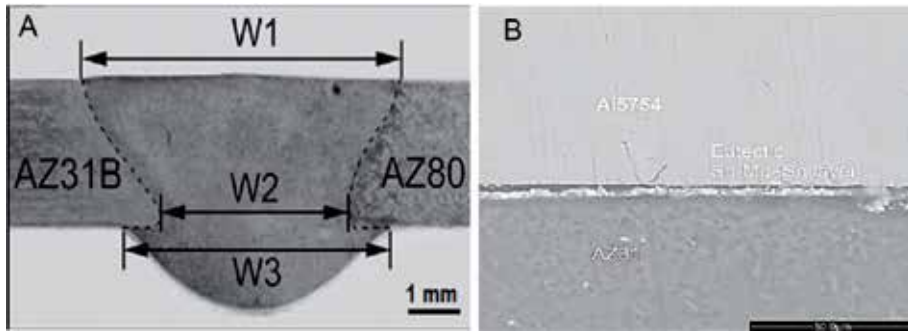


**Figure 1.** Micrographs showing the transverse section of joint welded by (a) TIG welding (b) ultrasonic welding [4].

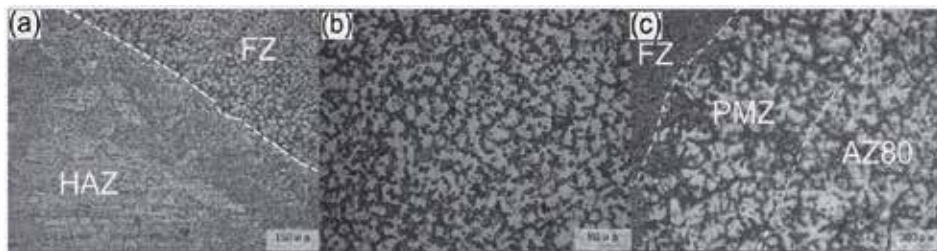


**Figure 2.** Microstructures of the welding joint produced by TIG welding (a) AZ31 side of the weld; (b) fusion zone; (c) AZ80 side of the weld [4].

achieve a bond strength of 84%. In their recent work, Song et al. [4] also showed that laser TIG welding produced good weldability and joint strength in Mg alloys when compared with hybrid welding. The hybrid welding approach resulted in a more flexible and reliable methodology for industrial application for magnesium alloys welding. The increased joint strength of Mg-AZ31 joints produced by hybrid TIG welding was attributed to the formation of a partially melted zone (PMZ) [4]. Several researchers successfully achieved dissimilar joining of magnesium alloys. The results of these studies demonstrated that while it is possible to join magnesium using TIG welding the heat input during welding results in significant changes in the HAZ that limits the strength of the joints produced. **Figure 2** shows an optical micrograph of fusion zone and the heat affected zone (HAZ) for two types of magnesium alloys joined using TIG welding, while the chemistry of the materials is different, the microstructural changes within the FZ and HAZ are similar in both alloys [4, 6].

Similarly, MIG welding has been shown by several researchers to be capable of joining magnesium alloys with greater speed when compared to TIG welding. Unique fast rigging proportions are normally required in the wire feeders since the magnesium terminal wire has a high melt-off rate. The typical wire feeder and power supply utilized for aluminum welding will be appropriate for welding magnesium. The heat input during MIG welding of magnesium alloys, however, results in the formation of a large HAZ containing a coarse grain structure which lowers the mechanical performance of the weld [7].

Recent studies in resistance spot welding (RSW) of magnesium alloys have demonstrated that dissimilar RSW of magnesium AZ31 to aluminum Al5754 coated with nanostructured electrodeposited coating prevented intermetallic formation while enhancing joint strength. RSW is the most common welding technique used in the

automotive industry because it is inexpensive, easily automated, and capable of producing high-quality welds [8]. The process is based on the contact resistance between the metals to be joined and the electrodes [9]. During the process, a weld nugget is formed by the melting of the materials as the temperature increases due to the materials' resistance. The heat generated during resistance spot welding (RSW) is based on Joule's law. However, the presence of surface oxides on magnesium alloys necessitates the use of high welding current because of the high contact resistance which also leads to rapid erosion of electrode tips used in the welding process. The scientific literature, however, shows that the heat input by RSW dissimilar joining of Al-Mg alloys leads to the formation of  $\text{Al}_{12}\text{Mg}_{17}$  and  $\text{Al}_3\text{Mg}_2$  intermetallic compounds within the weld nugget [10–12]. A recent study using Ni/ $\text{TiO}_2$  interlayer showed that the intermetallic formation during dissimilar resistance spot welding of magnesium to aluminum can be controlled with the inclusion of nanoparticles at the interface (see **Figure 3**) however, the addition of a coating step in the process extends the process time [13]. Despite the advancements that have been made regarding the impact of interlayers such as Zn as an interlayer between Al/Mg alloys, gold coated Ni interlayer [14, 15] and adhesive interlayers [16], to enhance the mechanical properties of the joints.

Laser welding, on the other hand, permits dissimilar joining of magnesium alloys while limiting the width of the HAZ, due to a smaller diameter beam and greater control of power input. However, the equipment used for laser welding is expensive and requires skilled operators. Furthermore, laser welding is usually applied to delicate and thin sheets due to the low penetration of laser beam into the materials. Ultrasonic spot welding (USW) have also been shown to eliminate some of the challenges encountered during RSW since the amount energy input into the material during welding is significantly lower, typically in the range of 0.5–1.2 kJ and requires a shorter welding time [17]. **Figure 1(B)** shows the microstructure of a bond made by ultrasonic welding. The formation of  $\text{Mg}_2\text{Sn}$  layer at the interface has been shown to limit the mechanical strength of the weld.

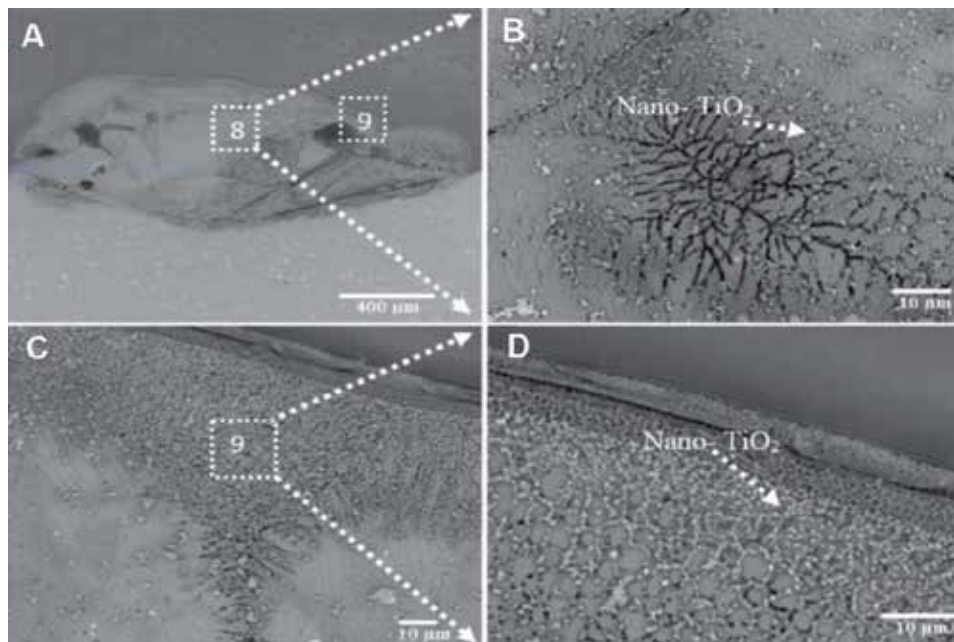


**Figure 3.** SEM micrograph showing: (A) Al/Ni- $\text{TiO}_2$ /Mg spot weld, (B) microstructure of point-8, (C) Al/weld nugget interface and (D) microstructure of point-9 [13].

A major challenge in welding magnesium alloys, however, is the presence of a surface oxide. Magnesium has a relatively low melting point, however, the surface oxide has a high melting point, as such removal of the surface oxide is required before welding of the metal. Additionally, several quality issues have been shown to arise during fusion welding of magnesium alloys. For example; large shrinkage during solidification and high chemical reactivity of Mg makes it very difficult to weld using traditional welding techniques [18], hence, Mg is usually alloyed with aluminum, zinc, and manganese for commercial usage [18]. A critical consideration is necessary for welding Mg alloys that may be affected by the properties of the alloying elements [19]. Any oxygen in contact with the weld pool, regardless of whether from the climate or the protecting gas, causes dross. Therefore, an adequate stream of idle protecting gases is essential, and welding in moving air ought to be avoided.

While fusion welding has been successfully used for similar metal joining of magnesium alloys, dissimilar welding of magnesium alloys to metals such as: steel [20], aluminum [21], and titanium has significant limitations due to the formation of intermetallic compounds within the joint region that minimize the joint strength and limits potential applications. The formation of various Mg-Al intermetallic compounds is detrimental to the mechanical performance of the materials. The formation of these compounds can be minimized with the use of interlayers between the materials to be joined. Given the potential for intermetallic formation, various joining techniques have been extensively studied with the objective being to minimize the formation of intermetallic compounds during joining while improving joint performance. Some of these techniques include friction stir welding, resistance spot welding, laser welding, ultrasonic welding, and diffusion bonding. These limitations have led to a preference for solid-state joining techniques to weld/join Mg and its alloys to other metals.

### 3. Friction stir welding

Friction stir welding (FSW) is a solid-state welding process that was developed at The Welding Institute (TWI) [22]. As explained by Mishra and Ma, the process is carried out by the use of a non-consumable rotating pin which travels along the joint to be welded [23]. The friction between the tool and the materials generates heat which softens the material [24]. **Figure 4** shows a schematic of the FSW

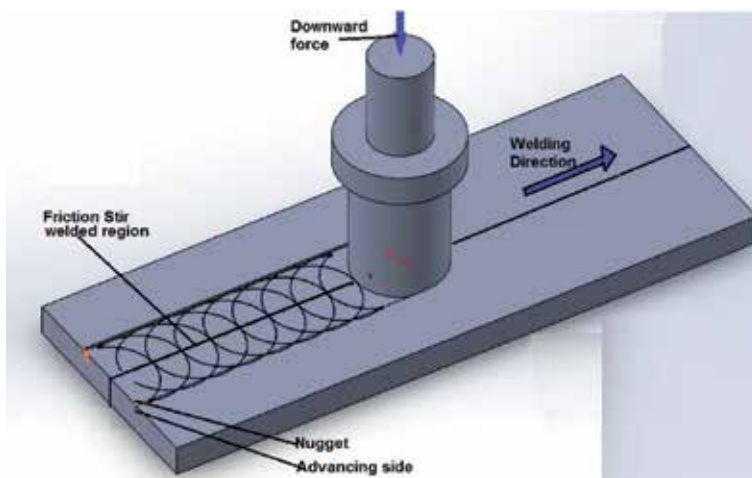


**Figure 4.**  
*Schematic of the friction stir welding process.*

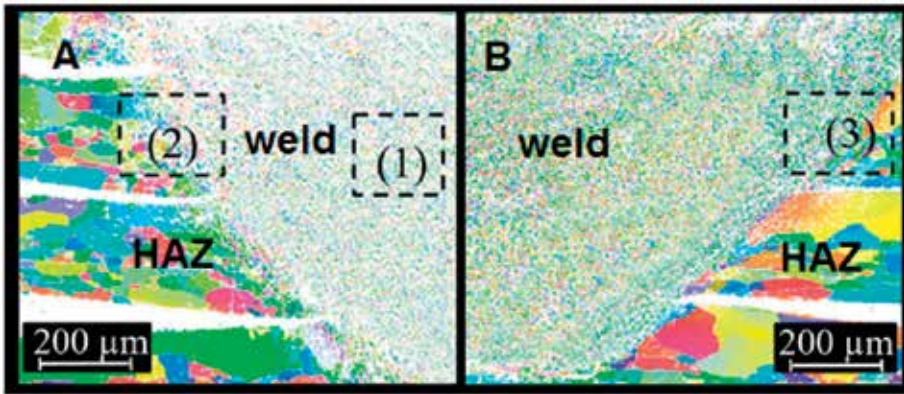


Figure 5. Weld produced by friction stir welding and the microstructure generated [26].

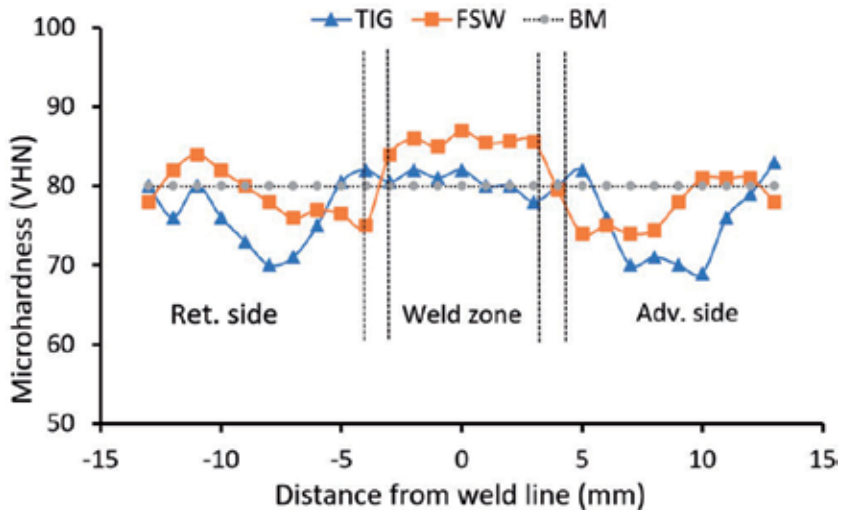


Figure 6. Hardness profiles across Mg-alloys welded using friction stir welding and TIG welding.

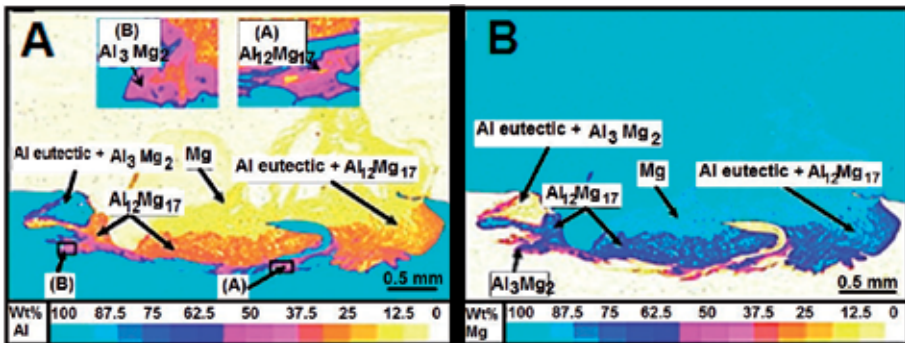


Figure 7. EPMA results of the FSW region of the sample welded by using a weld-pitch ratio of 1400/40 r/mm in the cross-section perpendicular to the tool transverse direction. Element distribution: (A) Al and (B) Mg [36].

process. The combination of tool rotation and localized softening of the material causes movement of the material leading to a weld. The process was first developed to weld aluminum alloys [22] previously described as non-weldable because of the adverse solidification microstructural formed in the fusion zone during fusion welding. Since its development, however, the technology has been applied to various metal and alloys. Zhang [25] demonstrated that friction stir welding is a viable technique for joining magnesium alloys.

Mg joints produced by FSW are characterized by high joint strength, high fatigue resistance, less distortion, since consumables are not required hence it is cheaper and no loss of alloying elements occurs during the process [27, 28].

The literature shows that weld quality is dependent on the optimization of the welding parameters; tool shape, jig rotational speed, tool speed, and joint configuration. In comparison to the traditional welding zones, the weld produced by FSW was characterized by four distinct zones as shown in **Figure 5** [26, 29]. These regions include; stirring zone (SZ), thermo-mechanical affected zone (TMAZ), heat affected zone (HAZ), and base metal (BM) [26, 30]. Singh et al. [23] demonstrated that FSW is capable of Mg weld with shear strength ranging from 66 to 410 MPa and the hardness from 50 to 110 HVN which represents 60–195% joint efficiency compared to the base metal alloy. **Figure 6** shows the hardness variation across the weld and confirms the hardness variations reported by Singh et al. The difference between the hardness recorded at the center of the weld and the base metal was attributed to the formation of IMCs with the weld during the FSW process. Similar findings were recorded by other researchers who studied different Mg alloys were welded using FSW such as; MgAZ31 [31, 32] and MgAZ31B [33], dissimilar joint of Al6061/MgAZ31B [34, 35]. Mohammadi et al. [36] demonstrated that while FSW can reduce the volume of intermetallic compounds formed during dissimilar welding, some IMCs will still form as shown in **Figure 7**.

## 4. Diffusion bonding

Diffusion bonding is a non-conventional solid-state welding process that can join a variety of materials in the solid state below the melting point of the base materials. The core mechanism involves the interdiffusion of atoms between the faying surfaces at the interface [37]. The process is frequently completed by one of two methods; firstly, solid-state diffusion bonding in which the base metals to be joined are heated to approximately 60% of the melting temperature of the metals under the influence of static load. Melting at the interface of the faying surfaces is prevented, however, interdiffusion of the diffusing species leads to the formation of solid-state bond. The second method is referred to as a transient liquid phase (TLP) diffusion bonding in which an interlayer is placed between the metals to be joined. Interdiffusion between the interlayer and the base metals facilitates the formation of a eutectic reaction which transitions from liquid to solid by isothermal solidification as the composition of the eutectic liquid changes due to diffusion. Each method will be further discussed below. A schematic of the diffusion bonding process is shown in **Figure 8**.

### 4.1 Solid-state diffusion bonding of magnesium alloys

Solid state diffusion bonding occurs due to the migration of atoms at the interface of the materials to be joined. The faying surfaces do not undergo any metallurgical discontinuity and as a result, the mechanical and microstructural property

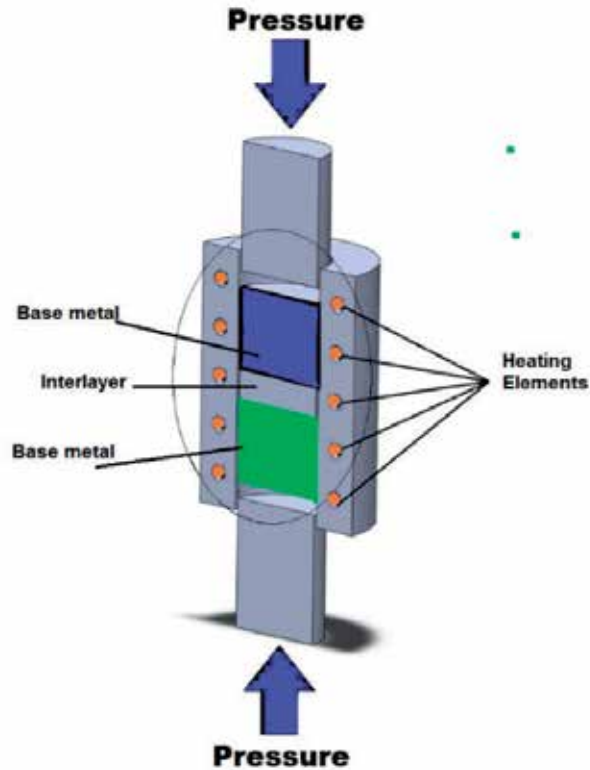


**Figure 8.**  
Schematic of the diffusion bonding process.

of the joint formed closely resembles those of the base materials [38]. Solid-state diffusion bonding goes through three distinct stages. The first stage includes; contact of the faying surfaces. In this stage, removal of surface roughness and irregularity play a significant role in ensuring good contact between the faying surfaces. Secondly, micro-plastic deformations at the interface, as the pressure inside the voids decreases and finally, grain boundary migration that fills the shrinkage and minimizes surface free energy. Surface preparation typically includes generation of a smooth surface and elimination of any oxides from the faying surfaces. Application of the pressure at the first stage ensures a good contact between the faying surfaces. Bonding pressure, temperature, and holding time are critical to achieving good bonds. Eq. (1) shows that the bonding temperature is proportional to the coefficient of the diffusing species. While the applied pressure ensures metal-metal contact and micro-plastic deformation of asperities at the interface of the faying surfaces.

$$D = D_0 e^{-\frac{Q}{RT}} \quad (1)$$

Where,  $D$  is the diffusion coefficient of the diffusing species,  $D_0$  is the pre-exponential term,  $R$  is gas constant and  $T$  is the bonding temperature. While bonding/hold time can be directly related to the volume of the diffusing species using Fick's second law of diffusion. Increasing the hold time is expected to enhance diffusion and strength the bond.

Diffusion bonding has been studied extensively as a method for both similar and dissimilar joining of magnesium alloys. The high temperature used in fusion welding process leads to the formation of intermetallic compounds, which have been shown to be detrimental to the mechanical performance of the joints when joining



magnesium alloys. Unfortunately, the dissimilar joining of magnesium alloys to other metals is significantly inhibited by the differences in the properties of the materials such as melting temperature, the coefficient of thermal expansion and thermal conductivity. Solid-state diffusion bonding limits intermetallic formations during dissimilar bonding and maximizes joint strength.

**Figure 9** shows the SEM micrograph of a solid-state diffusion bond formed between titanium (Ti-6Al-4V) and magnesium (AZ31) for 60 minutes. The width of the reaction layer at the interface appears to be in the form of dispersed particles approximately 20  $\mu\text{m}$  in length. EDS point analysis of the samples revealed the formation of several compounds at the bond interface. The results show that holding the sample at the bonding temperature, Al reacts with Ti and Mg leading to the precipitation of the  $\text{TiAl}_3$  and  $\text{Ti}_2\text{Mg}_3\text{Al}_{18}$  intermetallic compounds at the Ti interface. The  $\text{Mg}_{17}\text{Al}_{12}$  intermetallic compounds appear to have formed at the Mg grain boundaries. The  $\text{Mg}_{17}\text{Al}_{12}$  compound is believed to have been produced by a eutectic reaction between Al and Mg. The joint formation was attributed to metallurgical bonding driven leading to the formation of  $\text{TiAl}_3$  and  $\text{Ti}_2\text{Mg}_3\text{Al}_{18}$ . It is expected that the differences in the melting temperature of the two alloys at the bonding temperature of 500°C will cause the Mg sample to plastically deform ensuring complete contact with the Ti sample. Hidetoshi Somekawa [39] demonstrated that diffusion bonding of superplastic magnesium sheets is heavily dependent on the grain size of the material. For samples with grain size in the range of 11–15  $\mu\text{m}$  bond strength of approximately 92% of the base metal strength is possible. According to the Ti-Mg-Al ternary phase diagram the following phases;  $\text{Mg}_2\text{Al}_3$ ,  $\text{Mg}_{17}\text{Al}_{12}$ ,  $\text{TiAl}_3$  and  $\text{TiAl}_2$  are likely to form at the bonding temperature and pressure used in this study [6]. The Gibbs energy for the formation of  $\text{TiAl}_3$  is approximately 234 kJ/mol,  $\text{TiAl}_2$  is 237 kJ/mol [40]. The diffusion of Al to the bond interface from Ti-side to the Mg-side led to the formation of a compound having a stoichiometric composition of  $\text{Mg}_{17}\text{Al}_{12}$  where 43.95 wt.% of the compound is Al [41].

The  $\text{Mg}_{17}\text{Al}_{12}$  is an intermetallic compound with a Gibbs free energy of formation of  $-6$  kJ/mol at a temperature range of 700–1000 K. The Gibbs energy of formation increased to  $-3.9$  kJ/mol. From the Gibbs free energy data, the  $\text{Mg}_{17}\text{Al}_{12}$  intermetallic compound is most negative and therefore is expected to form first at the Mg-interface. The Gibbs energy for the formation of the ternary compound  $\text{Ti}_2\text{Mg}_3\text{Al}_{18}$  was found to be approximately  $-15$  kJ/mol [42]. The width of the reaction layer that forms at the interface is believed to be time dependent. As such, the layer thickness bears a direct relation with growth kinetics. The average thicknesses of the  $\text{TiAl}_3$  and  $\text{Ti}_2\text{Mg}_3\text{Al}_{18}$  layers and the total intermetallic layer was used to determine the kinetic parameters involved in the diffusion process.

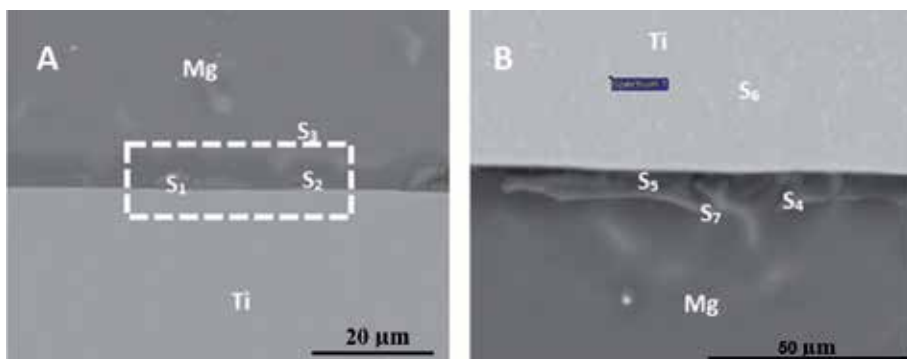


**Figure 9.** (A) Solid-state diffusion bonding of Ti and Mg for 60 minutes; (B) magnified region of the bond-line showing the reaction layer at the bond interface;

The data collected shows that as the bonding time increases the width of the reaction layer. The width also increased as predicted by the parabolic law shown in Eq. (2).

$$x = kt^n \quad (2)$$

Where  $k$  is the rate factor,  $t$  the diffusion time, and  $n$  the time exponent.

**Figure 10** shows the relationship between the bonding time and the thickness of the reaction layer formed at the interface and shows that as the bonding time increased the thickness of the reaction layer also increased. When the parabolic rate law is applied to the results, the rate coefficient  $k$  was calculated to be  $15.7 \times 10^{-7}$  m/s. The value for  $n$  was assumed to be 0.5 since the growth of the reaction layer was assumed to be controlled by inter-diffusion. When the calculated rate coefficient is substituted into the parabolic rate law shown in Eq. (1) the results show that the predicted thickness of the intermetallic layer was overestimated by the model.

The difference between the properties of the base metal and the bonded zone was highlighted by the micro-hardness measurements plotted in **Figure 11** as a function of bonding time. The micro-hardness values were measured across the joint starting at 500  $\mu\text{m}$  from the joint center. The figure shows that the hardness of the Ti sample fluctuated between 390 VHN and 420 VHN up to 100  $\mu\text{m}$  from the joint center as the bonding time was increased from 10 to 60 minutes. The hardness within the joint center was observed to decrease to between 190VHN at 10 minutes bonding time and 250 VHN at 60 minutes bonding time. The hardness of the Mg sample was found to be significantly lower than that of the Ti sample with a hardness ranging from 60 VHN at 10 minutes bonding time to 65 VHN. The variation of the hardness number across the interface was attributed to the differences between the properties of Ti and Mg. The hardness at the center of the bond is believed to have been caused by the formation of the reaction layer at the joint interface [43]. The reaction layer was shown to be made-up of  $\text{TiAl}_3$  and  $\text{Ti}_2\text{Mg}_3\text{Al}_{18}$  intermetallic compounds dispersed within the joint region.

#### 4.2 Transient liquid phase diffusion bonding

The transient liquid phase diffusion bonding process occurs due to the formation of a eutectic liquid at the interface between the faying surfaces. The eutectic reaction may form due to interdiffusion between the base metals or an interlayer and base metals which leads to the formation of a eutectic composition. Alternatively, a

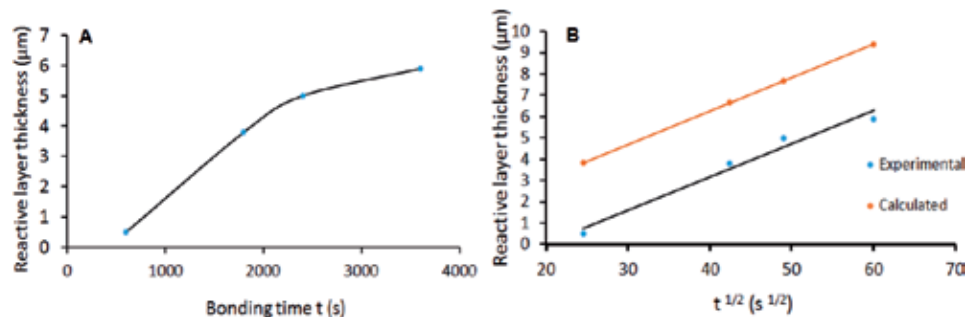


**Figure 10.** (A) Shows the relationship between the thickness of the reaction layer and the bonding time; (B) shows the predicted relationship between the thickness of the reaction layer and the bonding time according to the parabolic rate law.

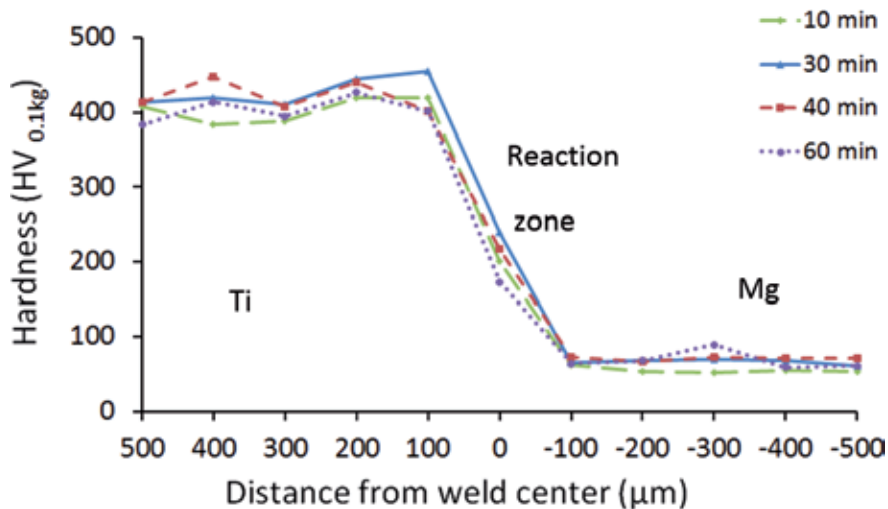


**Figure 11.** Micro-hardness measurements across the joint region as a function of bonding time.

thin interlayer having a eutectic composition and melts at the bonding temperature. The formation of the liquid displaces the surface oxides at the bond interface and reduces the bonding pressure requirement normally used to achieve surface contact during solid-state diffusion bonding. The advantage of the process is the potential for minimizing microstructural changes and intermetallic formations within the bond region and achieving joints with higher strength. However, TLP bonding can be a lengthy process that required four distinct stages (heating, dissolution and widen, isothermal solidification and homogenization) for completion [44]. Important parameters studied in TLP bonding include; interlayer composition and thickness, bonding temperature and bonding time [45].

#### 4.2.1 Interlayer thickness and composition

During TLP bonding the thickness and composition of the interlayer used are critical to the volume of liquid formed during bonding and invariably affects the quality of the bonds produced [46]. The scientific literature shows that suitable interlayers must allow eutectic melting while limiting the volume of the liquid that forms in order to control the width of the interface and shorten the homogenization stage of bonding [3]. Additionally, the wettability of the base metals by the molten interlayer is critical to displacing surface oxides in order to form a joint [2]. When suitable interlayers are used, the formation of intermetallic compounds (IMC) can be prevented or significantly reduced. The interlayers can be used in the form of; thin foils, fine powder, compact powder or paste, electroplated and vapor deposited coatings [47].

Selection of the interlayer composition depends on the base materials being joined. The literature shows that materials such as Sn, Ag, Al, Cu, Ni, Cr, V, and Zn are frequently used as interlayers during diffusion bonding. Most commonly used interlayers when joining magnesium alloys include Al, Cu, and Ni since these materials' leads to a eutectic reaction with magnesium which lowers the bonding temperature and catalyzes diffusion. When Al interlayer was used by Sun et al. [3] to bond Mg alloy MgAZ31, brittle IMC,  $CuMg_2$  was formed at the joint interface. However, increasing bonding temperature slightly increased the strength of the bond, as a result of microstructure homogenization for short bonding time. When the bonding time was increased beyond 60 minutes grain coarsening occurred which resulted in a reduction in joint strength.

In another study, Jin and Khan [48] studied the use of Ni, as an interlayer while joining the same Mg alloy, and found that the hardness of the joint increased as the bonding time increased as a result of the formation of Mg-Ni IMCs. Research results presented by Alhazaa et al. [49] showed that an optimum bonding time of 20 minutes was attained when bonding Mg AZ31 using Sn coatings. As shown in **Figure 12**, as the bonding time increased the bond line completely disappears, which is an indication of the homogenization of the bond region. The EPMA map shown in **Figure 13**, confirms the diffusion of Sn away from the interface and the homogenization of the composition within the joint region. Nevertheless, the formation of IMC at the joint consequently reduced the bond strength (see **Figure 15**). In contrast, Sun et al. [3] used Cu interlayer and suggested a bonding time of 30 minutes was optimal. The study also showed that the volume of intermetallic compounds formed was inversely proportional to hold time.

The potential for the dissimilar joining of Mg alloys to other metals is significantly greater with TLP bonding. Zhang et al. [50] demonstrated that Ni-coating can be used as an interlayer to join Mg to Al however suitable optimization of the bonding parameters are required to prevent the formation of a  $Mg_2Ni$  IMCs reaction layer between the metals. Alhazaa et al. [51] observed that the application of Cu coatings and Sn interlayers while bonding Mg AZ31 to the Ti-6Al-4V alloy. Increasing the bonding time also decreased the thickness of the IMC  $Mg_2Cu$  compounds and better bonds were formed between these dissimilar metal alloys (see **Figure 14**). The use of nanoparticle-reinforced composite interlayer during TLP process has also gained interest recently as they reduce grain size within the bond region and increase joint strength [52]. Similarly, Atieh and Khan [53], showed that when Ti-6Al-4V and Mg-AZ31 alloys were bonded using Ni and Cu nanoparticles, the joint formation was enhanced by increasing the rate of isothermal solidification during the TLP bonding process. **Figure 15** shows a TLP bond that was made between

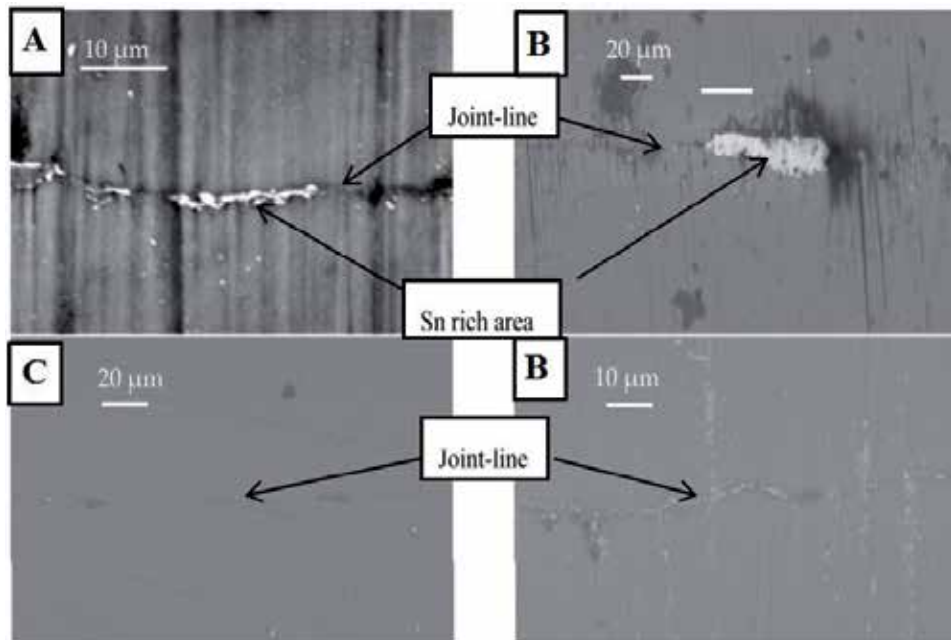


**Figure 12.** SEM micrograph of region bonded using Cu-coating and Sn-foil combination as interlayers for (A) 10 minutes; (B) 20 minutes; (C) 30 minutes; and (D) 50 minutes [2].

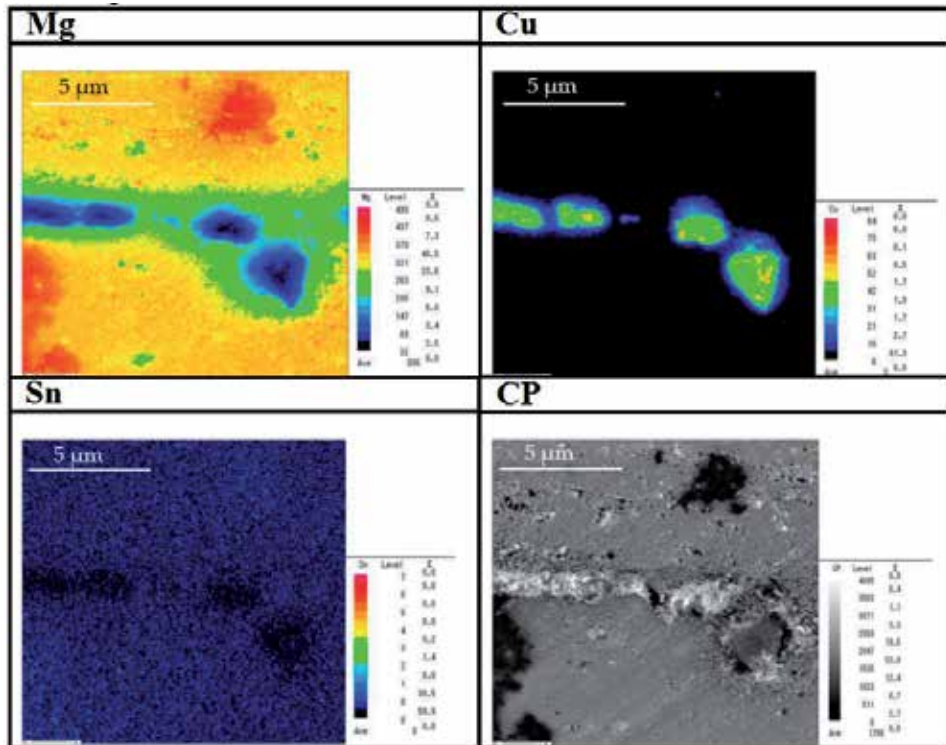


**Figure 13.** Electron probe micro-analysis (EPMA) micrographs of Mg, Cu, and Sn for bonds made using Cu coating and Sn-foil interlayer at 20 minutes [2].

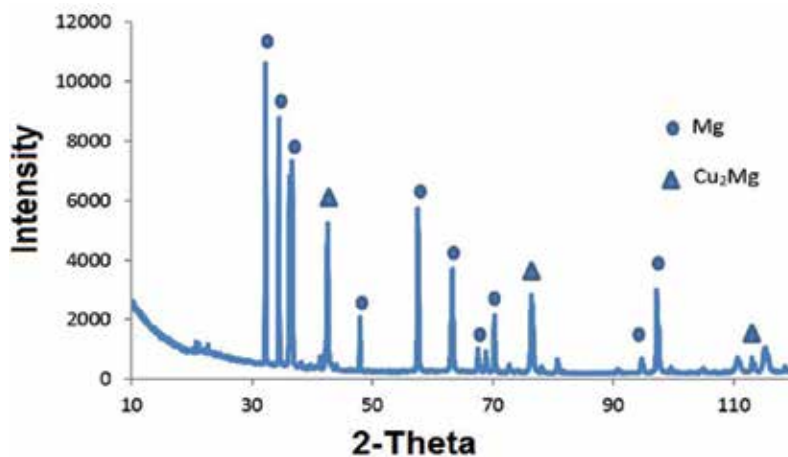


**Figure 14.** XRD spectrum of the compounds formed at the interface for joint made during similar TLP bonding of Mg (AZ31) with Sn interlayer and bonded for 30 minutes.

Mg and Al using Cu/Al<sub>2</sub>O<sub>3</sub> interlayer and confirms that the addition of nanoparticles can prevent the formation of a continuous IMC layer at the joint interface which leads to an increase in strength. The composition of the joint region was evaluated using EDS and is shown in **Figure 15(B)**. A summary of recent interlayers studied and the impact of composition on the mechanical performance of the bonds is presented in **Table 1**. The strength coefficient for each bond was estimated using Eq. (3).

$$m = \frac{\tau_{bond}}{\tau_b} \quad (3)$$

Where  $m$  represents the strength coefficient of the bond,  $\tau_{bond}$  is the strength of the bond and  $\tau_b$  is the strength of the base metal.

#### 4.2.2 Bonding time and temperature

TLP diffusion bonding is a heavily time-dependent process with the duration of each stage contributing to the length of time required to achieve bond strength. Several models have been developed based on Fick's second law that seeks to predict the duration of each stage of the TLP bonding process. The most notable of these models was proposed by Zhou et al. [54]. Experimental research on TLP bonding of

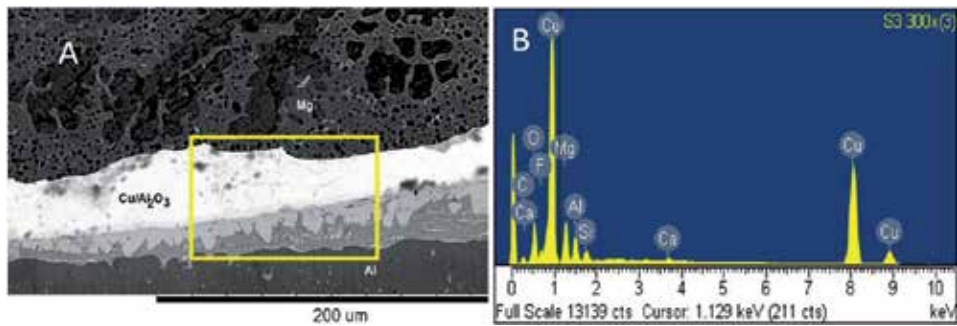


**Figure 15.** (A) TLP bonding of Mg-AZ31 and Al-1100 using a Cu coating containing nano-Al<sub>2</sub>O<sub>3</sub> particles and bonding condition 10 minutes at 500°C and 0.2 MPa (B) EDS analysis of the highlighted region.

Bonding system	Interlayer	Temperature (C)	Pressure (MPa)	Time (minutes)	Shear strength (MPa)	$m$	Reference
Mg-AZ31 similar bonding	Ni coatings	520	8.0	20	46.2	0.557	[49]
Mg-AZ31 similar bonding	Cu coatings	520	0.5	30	41.0	0.482	[2]
Mg-AZ31 similar bonding	Cu coatings with Sn foil	520	0.5	30	64.0	0.771	[51]
Mg AZ31	Cu foil	530	2.0	30	70.2	0.852	[3]
Mg-AZ31 and Ti-6Al-4V	Cu coatings with Sn foil	580	1.0	15	78.0	0.934	[51]
Mg-AZ31 and Ti-6Al-4V	Ni coating	540	0.2	20	50	0.602	[46]
Mg-AZ31 and Al100	Cu/Al <sub>2</sub> O <sub>3</sub>	500	0.2	10	20.4	0.36	Current work

**Table 1.** Shear strength of diffusion bonded joints.

magnesium alloys suggests that this model is still an important tool for predicting the duration of each stage of the bonding process.

Similarly, temperature serves as an important parameter in order to produce a successful joint in the diffusion bonding as it significantly changes the kinetics of the atomic movement at the interface. Given that the interlayer melts and then solidifies at the bonding temperature and therefore, the bonding temperature should reach the melting temperature of the interlayer. The temperature used should be controlled and remain constant throughout the bonding process in order to enhance diffusion, but not cause metallurgical changes or cause excess melting of the joint region. Light metals, such as magnesium, need to be bonded at an optimal temperature so that micro-deformation is avoided.

Bonding time is a variable closely related to temperature. Increasing the bonding temperature require a shorter hold time. It is seen that increasing pressure, time and temperature produces strong joint up to a point after which the parameters become redundant. The process of diffusion bonding uses a wide range of bonding time, from seconds to hours, for different joining surfaces.

Long bonding times enhances atomic diffusion along the bond line but may increase the likelihood of IMCs forming at the interface, which are detrimental to mechanical properties. Research by Sun et al. [3] proved the influence of bonding temperature on shear and bonding strengths of the bonded joints followed by the pressure applied, holding time and surface roughness. Azizi and Alimardan [55] confirmed a direct proportion relationship existed between the increase in the width of the interface as the bonding temperature and hold time increases.

## 5. General remarks

The properties of magnesium alloys allow them to be used in the various structural applications including biomedical applications such as implants. Given that that magnesium is non-toxic, biocompatible and biodegradable, these materials can be used to serve as implants or replacements of body tissues. The current use of titanium implants for bone treatment and implants in the tissues may be replaced by Mg alloys since titanium alloys are not biodegradable therefore another operation/surgery is needed in most cases after the healing of the affected tissues. One direction is to develop new Mg alloys with various alloying elements such as Zn, Al, Zr, and others, in order to reach the desired degradation rate suitable for the human body. Another challenge in using Mg alloy for bone fixation is the low mechanical strength of Mg when compared to Ti.

A significant challenge, however, is identifying suitable joining technologies capable of welding/joining magnesium to other metals such as Ti and prevents IMC formations. While conventional fusion welding is also capable of a selective dissimilar joining of Mg alloys the product of these processes is not suitable for biomedical applications. On the other hand, solid-state diffusion bonding, TLP diffusion bonding process and friction stir welding have demonstrated greatest potential for the dissimilar joining of Mg alloys.

## **Author details**

Kavian O. Cooke<sup>1,2\*</sup>, Abdulaziz Alhazaa<sup>3</sup> and Anas M. Atieh<sup>4</sup>

1 School of Engineering and Informatics, University of Bradford, Bradford, UK

2 Mechanical Engineering Department, University of Technology, Jamaica WI


3 Physics and Astronomy Department, College of Science, King Saudi University, Riyadh, Saudi Arabia

4 Industrial Engineering Department, School of Applied Technical Sciences, German Jordanian University (GJU), Amman, Jordan

\*Address all correspondence to: [kavian\\_cooke@yahoo.com](mailto:kavian_cooke@yahoo.com)

## **IntechOpen**

---

© 2019 The Author(s). Licensee IntechOpen. This chapter is distributed under the terms of the Creative Commons Attribution License (<http://creativecommons.org/licenses/by/3.0>), which permits unrestricted use, distribution, and reproduction in any medium, provided the original work is properly cited. 



## References

- [1] Li N, Zheng Y. Novel magnesium alloys developed for biomedical application: A review. *Journal of Materials Science and Technology*. 2013;**29**(6):489-502
- [2] Alhazaa A, Shar M, Atieh A, Nishikawa H. Transient liquid phase bonding of magnesium alloy AZ31 using Cu coatings and Cu coatings with Sn interlayers. *Metals*. 2018
- [3] Sun DQ, Liu WH, Gu XY. Transient liquid phase bonding of magnesium alloy (Mg-3Al-1Zn) using copper interlayer. *Materials Science and Technology*. 2004;**20**(12):1595-1598. DOI: 10.1179/174328413X13789824293506
- [4] Song G, Diao Z, Lv X, Liu L. TIG and laser-TIG hybrid filler wire welding of casting and wrought dissimilar magnesium alloy. *Journal of Manufacturing Processes*. 2018;**34**:204-214
- [5] Peng J, Zhou C, Tao J-Q, Pan F-S. Gas tungsten arc welding of dissimilar magnesium alloys as AZ31 with AZ61. *Cailiao Gongcheng/Journal of Materials Engineering*. 2011;**1**(2):46-51
- [6] Kurt HI, Guzelbey IH, Salman S, Asmatulu R, Dere M. Investigating the relationships between structures and properties of Al alloys incorporated with Ti and Mg inclusions. *Journal of Engineering Materials and Technology*. 2016;**138**(3):031006-031006-6. DOI: 10.1115/1.4032849.
- [7] Liu L, Ren D. A novel weld-bonding hybrid process for joining Mg alloy and Al alloy. *Materials and Design*. 2011;**32**(7):3730-3735
- [8] Thakur AG, Nandedkar V. Optimization of the resistance spot welding process of galvanized steel sheet using the Taguchi method. *Arabian Journal for Science and Engineering*. 2014;**39**(2):1171-1176
- [9] Kim YG, Kim IJ, Kim JS, Il Chung Y, Choi DY. Evaluation of surface crack in resistance spot welds of Zn-coated steel. *Materials Transactions*. 2014;**55**(1):171-175
- [10] Patel VK, Bhole SD, Chen DL. Improving weld strength of magnesium to aluminium dissimilar joints via tin interlayer during ultrasonic spot welding. *Science and Technology of Welding and Joining*. 2012;**17**(5):342-347. DOI: 10.1179/1362171812Y.0000000013
- [11] Choi DH, Ahn BW, Lee CY, Yeon YM, Song K, Jung SB. Formation of intermetallic compounds in Al and Mg alloy interface during friction stir spot welding. *Intermetallics*. 2011;**19**(2):125-130
- [12] Sato YS, Shiota A, Kokawa H, Okamoto K, Yang Q, Kim C. Effect of interfacial microstructure on lap shear strength of friction stir spot weld of aluminium alloy to magnesium alloy. *Science and Technology of Welding and Joining*. 2010;**15**(4):319-324. DOI: 10.1179/136217109X12568132624208
- [13] Cooke KO, Khan TI. Resistance spot welding aluminium to magnesium using nanoparticle reinforced eutectic forming interlayers. *Science and Technology of Welding and Joining*. 2017;**23**(4):271-278. DOI: 10.1080/13621718.2017.1373481
- [14] Penner P, Liu L, Gerlich A, Zhou Y. Feasibility study of resistance spot welding of dissimilar Al/Mg combinations with Ni based interlayers. *Science and Technology of Welding and Joining*. 2013;**18**(7):541-550. DOI: 10.1179/1362171813Y.0000000129
- [15] Penner P, Liu L, Gerlich A, Zhou Y. Dissimilar resistance spot welding of aluminum to magnesium with Zn-coated steel interlayers. *Welding Journal*. 2014;**93**:225-231

- [16] Xu W, Chen DL, Liu L, Mori H, Zhou Y. Microstructure and mechanical properties of weld-bonded and resistance spot welded magnesium-to-steel dissimilar joints. *Materials Science and Engineering A*. 2012;**537**(1):11-24
- [17] Bakavos D, Prangnell PB. Mechanisms of joint and microstructure formation in high power ultrasonic spot welding 6111 aluminium automotive sheet. *Materials Science and Engineering A*. 2010;**527**(23):6320-6334
- [18] Mordike BL, Ebert T. Magnesium properties-applications-potential. *Materials Science and Engineering A*. 2001;**302**(1):37-45
- [19] Pareek JE, Polar M, Rumiche A, Indacochea F. Metallurgical evaluation of AZ31B-H24 magnesium alloy friction stir welds. *Journal of Materials Engineering and Performance*. 2007;**16**(5):655-662
- [20] Feng Y, Li Y, Luo Z, Ling Z, Wang Z. Resistance spot welding of Mg to electro-galvanized steel with hot-dip galvanized steel interlayer. *Journal of Materials Processing Technology*. 2016;**236**:114-122
- [21] Shah LH, Othman NH, Gerlich A. Review of research progress on aluminium-magnesium dissimilar friction stir welding. *Science and Technology of Welding and Joining*. 2018;**23**(3):256-270. DOI: 10.1080/13621718.2017.1370193
- [22] Thomas WM, Nicholas ED, Needham JC, Murch MG, Temple-Smith P, Dawes CJ. Improvements Relating to Friction Welding. International Patent. December 1991. Application No. PCT/GB92/02203. Publication No. WO19930109935 A1, 6
- [23] Singh K, Singh G, Singh H. Review on friction stir welding of magnesium alloys. *Journal of Magnesium and Alloys*. 2018;**0**:1-18
- [24] Mishra RS, Ma ZY. Friction stir welding and processing\_PAP\_pges4-7+70. *Materials Science and Engineering R*. 2005;**50**(1-2):1-78
- [25] Zhang H. Friction stir welding of magnesium alloys. In: *Welding and Joining of Magnesium Alloys*. Woodhead Publishing Series in Welding and Other Joining Technologies. Sawston, UK: Cambridge. 2010;274-305
- [26] Wang K, Khan HA, Li Z, Lyu S, Li J. Micro friction stir welding of multilayer aluminum alloy sheets. *Journal of Materials Processing Technology*. 2018;**260**:137-145
- [27] Mishra RS, Ma ZY. Friction stir welding and processing. *Materials Science and Engineering R*. 2005;**50**(1-2):1-78
- [28] Singh G, Singh H, Singh K. Friction stir welding of magnesium alloys: A review. *Asian Review of Mechanical Engineering*. 2016;**5**(1):5-8
- [29] Carlone P, Astarita A, Rubino F, Pasquino N. Microstructural aspects in FSW and TIG welding of cast ZE41A magnesium alloy. *Metallurgical and Materials Transactions B: Process Metallurgy and Materials Processing Science*. 2016;**47**(2):1340-1346
- [30] Radj BM, Senthivelan T. Analysis of mechanical properties on friction stir welded magnesium alloy by applying Taguchi Grey based approach. *Materials Today: Proceedings*. 2018;**5**:8025-8032
- [31] Mironov S, Onuma T, Sato YS, Yoneyama S, Kokawa H. Microstructural changes during tension of friction-stir welded AZ31 magnesium alloy. *Materials Characterization*. 2017;**130**:1-8
- [32] Mironov S, Onuma T, Sato YS, Yoneyama S, Kokawa H. Tensile behavior of friction-stir welded AZ31 magnesium alloy S. *Materials Science and Engineering A*. 2017;**679**:272-281

- [33] Woo W, Choo H, Prime MB, Feng Z, Clausen B. Microstructure, texture and residual stress in a friction-stir-processed AZ31B magnesium alloy. *Acta Materialia*. 2008;**56**(8):1701-1711
- [34] Yang CL, Wu CS, Lv XQ. Numerical analysis of mass transfer and material mixing in friction stir welding of aluminum/magnesium alloys. *Journal of Manufacturing Processes*. 2018;**32**:380-394
- [35] Abdollahzadeh A, Shokuhfar A, Cabrera JM, Zhilyaev AP, Omidvar H. In-situ nanocomposite in friction stir welding of 6061-T6 aluminum alloy to AZ31 magnesium alloy. *Journal of Materials Processing Technology*. 2019;**263**:296-307
- [36] Mohammadi J, Behnamian Y, Mostafaei A, Izadi H, Saeid T, Kokabi AH, et al. Friction stir welding joint of dissimilar materials between AZ31B magnesium and 6061 aluminum alloys: Microstructure studies and mechanical characterizations. *Materials Characterization*. 2015;**101**:189-207
- [37] Wilden J, Jahn S, Beck W. Some examples of current diffusion bonding applications. In: *Material-wissenschaft und Werkstofftechnik*. 2008;**39**(4-5):349-352
- [38] Maharana HS, Ashok A, Pal S, Basu A. Surface-mechanical properties of electrodeposited Cu-Al<sub>2</sub>O<sub>3</sub> composite coating and effects of processing parameters. *Metallurgical and Materials Transactions A, Physical Metallurgy and Materials Science*. 2016;**47**(1):388-399
- [39] Somekawa H, Hosokawa H, Watanabe H, Higashi K. Diffusion bonding in superplastic magnesium alloys. *Materials Science and Engineering A*. 2003;**339**(1-2):328-333
- [40] Khoshhal R, Soltanieh M, Mirjalili M. Formation and growth of titanium aluminide layer at the surface of titanium sheets immersed in molten aluminum. *Iranian Journal of Materials Science and Engineering*. 2010;**7**(1):24-31
- [41] Czerwinski F, editor. Precipitates of gamma-Mg<sub>17</sub>Al<sub>12</sub> phase in Mg-Al alloys. In: *Magnesium Alloys—Design, Processing and Properties*. Rijeka, Croatia: Intech; 2011
- [42] I. S. Effenberg G. Part 3. Landolt-Börnstein-group IV physical chemistry (numerical data and functional relationships in science and technology). In: Effenberg G, editor. *Light Metal Systems Materials Science International Team MSIT<sup>®</sup> Al-Mg-Ti (Aluminium-Magnesium-Titanium)*. Vol 11A3, I. S. Berlin, Heidelberg: Springer; 2011
- [43] Alhazaa TIK, Haq I. Transient liquid phase (TLP) bonding of Al7075 to Ti-6Al-4V alloy. *Materials Characterization*. 2010;**61**:312-317
- [44] Cooke KO, Khan TI, Oliver GD. Transient liquid phase diffusion bonding Al-6061 using nano-dispersed Ni coatings. *Materials and Design*. 2012;**33**(1)
- [45] Cooke K. Spectroscopic Analyses of Nano-Dispersion Strengthened Transient Liquid Phase Bonds: In *Advance aspects of Spectroscopy*, Rijeka, Croatia: Intech. 2012:309-340
- [46] Atieh AM, Khan TI. Effect of interlayer thickness on joint formation between Ti-6Al-4V and Mg-AZ31 alloys. *Journal of Materials Engineering and Performance*. 2014;**23**(11):4042-4054
- [47] Cooke K, Oliver G, Buchanan V, Palmer N. Optimisation of the electric wire arc-spraying process for improved wear resistance of sugar mill roller shells. *Surface and Coatings Technology*. 2007;**202**(1):185-188
- [48] Jin YJ, Khan TI. Effect of bonding time on microstructure and mechanical

properties of transient liquid phase bonded magnesium AZ31 alloy. *Materials and Design*. 2012;**38**:32-37

[49] Alhazaa AN, Khalil KA, Shar MA. Transient liquid phase bonding of magnesium alloys AZ31 using nickel coatings and high frequency induction heat sintering. *Journal of King Saud University - Science*. 2016;**28**(2):152-159

[50] Zhang J, Luo G, Wang Y, Shen Q, Zhang L. An investigation on diffusion bonding of aluminum and magnesium using a Ni interlayer. *Materials Letters*. 2012;**83**(15):189-191

[51] Alhazaa AN, AlGharbi SH, Nishikawa H. Effect of bonding temperature on the joining of Ti-6Al-4V alloy using Cu coatings and Sn interlayers. *Journal of Materials Engineering and Performance*. 2017;**26**(1):407-417

[52] Cooke KO. A study of the effect of nanosized particles on transient liquid phase diffusion bonding al6061 metal-matrix composite (MMC) using Ni/Al<sub>2</sub>O<sub>3</sub> Nanocomposite interlayer. *Metallurgical and Materials Transactions B: Process Metallurgy and Materials Processing Science*. 2012;**43**(3):627-634

[53] Atieh AM, Khan TI. Application of Ni and Cu nanoparticles in transient liquid phase (TLP) bonding of Ti-6Al-4V and Mg-AZ31 alloys. *Journal of Materials Science*. 2014;**49**(22):7648-7658

[54] Zhou Y, Gale WF, North TH. Modelling of transient liquid phase bonding. *International Materials Review*. 1995;**40**(5):181-196. DOI: 10.1179/imr.1995.40.5.181

[55] Azizi A, Alimardan H. Effect of welding temperature and duration on properties of 7075 Al to AZ31B Mg diffusion bonded joint. *Transactions of Nonferrous Metals Society of China*. 2016;**26**(1):85-92

# Magnesium-Based Materials for Hydrogen Storage: Microstructural Properties

*Ryota Kondo and Takeshita T. Hiroyuki*

## Abstract

Magnesium (Mg) is hydrogenated as core-shell-type hydride. Therefore, increase of absorption capacity to the theoretical hydrogen capacity is still one of the most important issues for the hydrogen storage materials. In this study, the procedure of the core-shell structure as well as effect of Al concentration in Mg on the growth MgH<sub>2</sub> in Mg were investigated. MgH<sub>2</sub> was formed on the surface as well as inside of unreacted Mg core. The inside MgH<sub>2</sub> was formed in a granular form on Mg grain boundary and its size increased by applying plastic deformation. Thickness of the surface MgH<sub>2</sub> and size of the internal MgH<sub>2</sub> increased with an increase in hydrogenation time until the hydride surface was completely covered with MgH<sub>2</sub>. However, the growth of the surface and internal MgH<sub>2</sub> came to a halt after the surface was covered with MgH<sub>2</sub>. From these results, supplying H from metal side was dominantly contributed for growth of the surface and internal MgH<sub>2</sub> because diffusion rate of H in Mg was much higher than that in MgH<sub>2</sub>. In addition, the growth of internal MgH<sub>2</sub> as well as control of surface MgH<sub>2</sub> can contribute to the promotion of the complete hydrogenation of Mg-based hydrogen storage materials.

**Keywords:** magnesium, hydride, internal, three-dimension, surface, microstructure, distribution, grain boundary

## 1. Introduction

Magnesium (Mg) can store 7.6 mass% of hydrogen after formation of magnesium hydride (MgH<sub>2</sub>), which has attractive features for hydrogen storage material such as low cost, abundant resource and light weight [1]. However, dehydrogenation temperature is very high (560 K at 0.1 MPaH<sub>2</sub>) because MgH<sub>2</sub> is thermodynamically stable ( $\Delta_r H = -72.8 \pm 4.2 \text{ kJ mol}^{-1}$ ,  $\Delta_r S = -142 \pm 3 \text{ J K}^{-1} \text{ mol}^{-1}$ ) [2]. In addition, their hydrogenation/dehydrogenation kinetics is also lower, then the conditions of hydrogenation and dehydrogenation are severe and core-shell-type hydride is formed. In order to obtain MgH<sub>2</sub> completely from Mg and effectiveness of hydrogenation/dehydrogenation process, it is necessary to finely pulverize, severe plastic deformation, heat treatment for a long time, and addition of catalyst [3–10].

Mg is a metal and when it reacts with H<sub>2</sub>, MgH<sub>2</sub> forms an ionic bond and a weak covalent bond between Mg-H and the valence number of the ion is indicated as Mg<sup>1.91+</sup> and H<sup>0.26-</sup> [11]. The diffusion coefficient of H in MgH<sub>2</sub> is several order of magnitude lower when compared to that in Mg:  $D_H^{\text{Mg}} = 7 \times 10^{-11} \text{ m}^2 \text{ s}^{-1}$

(300 K) in Mg and  $D_{\text{H}}^{\text{MgH}_2} = 1.1 \times 10^{-20} \text{ m}^2 \text{ s}^{-1}$  (305 K) in MgH<sub>2</sub> [12, 13]. Based on these characteristics, powder Mg forms core-shell-type structure hydride, MgH<sub>2</sub> as a shell and unreacted Mg remains in the core [14, 15] making progress of completely hydrogenation difficult. On the other hand, the hydrogen partial pressure has a great influence on the progress of the hydrogenation. When the hydrogen partial pressure is high, since MgH<sub>2</sub> quickly covers the Mg powder surface, hydrogenation halts and the amount of hydride concentration decreases markedly, whereas when the hydrogen partial pressure is low, the time until MgH<sub>2</sub> covers the Mg surface extends, then the hydride concentration increases [16]. Therefore, to accomplish the efficient hydrogenation, the process of hydrogenation should be revealed.

As a result of investigation aiming at efficient hydrogenation, some curious microstructural characteristics were obtained, that is shell of MgH<sub>2</sub> and core Mg in addition to MgH<sub>2</sub> in the core Mg. In the following, MgH<sub>2</sub> on the surface layer named as MgH<sub>2</sub>(sur) and that in Mg core named as MgH<sub>2</sub>(int). MgH<sub>2</sub>(int) formed in the Mg core is distinguished from MgH<sub>2</sub>(sur). The particle size of MgH<sub>2</sub>(int) in Mg<sup>-6</sup> mass%, Al-1 mass%, Zn alloy was larger than that in pure Mg. This result shows the grain size of MgH<sub>2</sub>(int) would be in correlation with Al concentration. Therefore, in this study, the influence of Al concentration in Mg on formation of MgH<sub>2</sub>(int) is clarified. To reveal the mechanism of MgH<sub>2</sub>(int) formation, coarse-type Mg-based hydrogen storage materials will be developed. Bulky hydrogen storage materials are attractive for handling, safety, and applying large module.

## 2. Materials and methods

Pure Mg manufactured by Rare Metallic Co., Ltd. and Mg- (3, 6, 9) mass%, Al-1 mass%, Zn alloy (hereinafter referred to as AZ31, AZ61, AZ91) manufactured by Sankyo Aluminum Co., Ltd. were used as samples. **Table 1** shows the composition of the samples.

As pretreatment, these samples were cut into prismatic shapes (8 mm in width, 5 mm in length, 3 mm in thickness) and then annealed, evacuated to  $2 \times 10^{-4}$  Pa in a stainless steel container, and replacing it with Ar gas (nominal purity 99.9999 vol%) was repeated several times and then heated under an Ar atmosphere of 3 kPa at a temperature of 723 K and a treatment time for 32.4 ks. For AZ61, annealed material (annealed) and 10% cold-rolled sample (cold-rolled) were subjected to hydrogenation (129.6 ks), respectively. An observation of the cross-sectional structure was carried out using an optical microscope (OM). Mg alloys are known to produce MgH<sub>2</sub> at low temperature by applying severe plastic deformation [17]. **Table 2** shows the crystal grain sizes of annealed Mg and AZ31, AZ61, and AZ91 alloys.

Material	Composition (mass%)							
	Al	Zn	Mn	Si	Fe	Cu	Ni	Ca
Mg	0.0013	0.0024	0.012	0.022	0.0016	0.0031	0.0003	0.01
AZ31	2.80	0.80	0.32	0.022	0.003	0.003	<0.002	
AZ61	6.26	0.63	0.26	0.015	0.005	0.001	0.0007	
AZ91	8.70	0.82	0.22	0.007	0.005	<0.002	0.002	

**Table 1.**  
Composition of Mg and AZ31, AZ61, AZ91 alloys.

Material	Grain size, $d/\mu\text{m}$ (standard deviation)
Mg	250 (70)
AZ31	34 (3.4)
AZ61	36 (4.8)
AZ91	40 (3.5)

**Table 2.**  
Grain size of annealed Mg and AZ31, AZ61, and AZ91 alloys.

For hydrogenation of Mg alloys, these samples after annealing was dry-polished with SiC abrasive paper (# 320) in Ar gas circulation-type glove box (dew point  $-55$  to  $-70^\circ\text{C}$ , oxygen concentration 1 ppm or less), dry polished and immediately sealed in a stainless steel reaction vessel with a gasket made of stainless steel with Ag plating. In this reaction vessel, a sheath-type thermocouple was installed inside the container and the temperature in the vicinity of the samples was set. In order to generate  $\text{MgH}_2$ , hydrogenation was carried out at a hydrogen pressure of 3.61 MPa and a temperature of 673 K using a Siebert's type apparatus, and the nominal purity of the hydrogen gas used was 99.99999 vol%. The time was maintained in the range of 0–259.2 ks, and it is shown in parentheses here after.

The X-ray diffraction (XRD) instrument was used for the identification of  $\text{MgH}_2(\text{sur})$ . X-ray source of  $\text{CuK}\alpha$  with the tube voltage of 40 kV and the tube current of 15 mA was used. Microstructure of  $\text{MgH}_2$  was judged with presence or absence of charge up by using of scanning electron microscope (SEM). Crystal structure of  $\text{MgH}_2(\text{int})$  was investigated using an electron beam backscatter diffraction (EBSD) analyzer.

Samples for microstructural observation and analysis were cut at a position of 4 mm which is half in the width direction and roughly polished using SiC polishing paper (# 320  $\rightarrow$  # 800  $\rightarrow$  # 1000) followed by an  $\text{Al}_2\text{O}_3$  suspension ( $0.05\ \mu\text{m}$ ) or  $\text{SiO}_2$  suspension ( $0.04\ \mu\text{m}$ ). Dehydrated methanol was used as the extension liquid. The sample after polishing was promptly washed with an ultrasonic washing machine in dehydrated methanol. After washing, the sample was dried using pure nitrogen gas (99.99%).

Three-dimensional analysis of  $\text{MgH}_2(\text{sur})$  and  $\text{MgH}_2(\text{int})$  was carried out based on data constructed by a continuous serial sectional method, and an optical microscope (OM) was used for microstructural observation. Information at the position and observation depth was obtained by driving a pyramidal indentation into the sample using a Vickers hardness instrument. ImageJ was used for geometrical analysis and the construction of the three-dimension image [18, 19].

**Figure 1** described quantitative analysis method for obtaining information on the thickness of the  $\text{MgH}_2(\text{sur})$  layer. In the analysis, five or more images are selected and the  $\text{MgH}_2$  was observed as a dark area. The mean thickness ( $d_{\text{av}}$ ) of  $\text{MgH}_2(\text{sur})$  was calculated by dividing the area of each observed  $\text{MgH}_2(\text{sur})$  by the length of  $\text{MgH}_2(\text{sur})$  on the surface. Next, the shape of the surface is extracted. The surface line was translated in the direction of the inside. The maximum thickness of  $\text{MgH}_2(\text{sur})$  was evaluated as the translated length at point of the surface line parted from  $\text{MgH}_2(\text{sur})$  particle. The minimum thickness ( $d_{\text{min}}$ ) was evaluated at the first point of intersection between the shape line and Mg. The average particle size of  $\text{MgH}_2(\text{int})$  is calculated by calculating the area of  $\text{MgH}_2(\text{int})$ , and the value of the diameter calculated when assuming  $\text{MgH}_2(\text{int})$  as a spherical calculation on average.

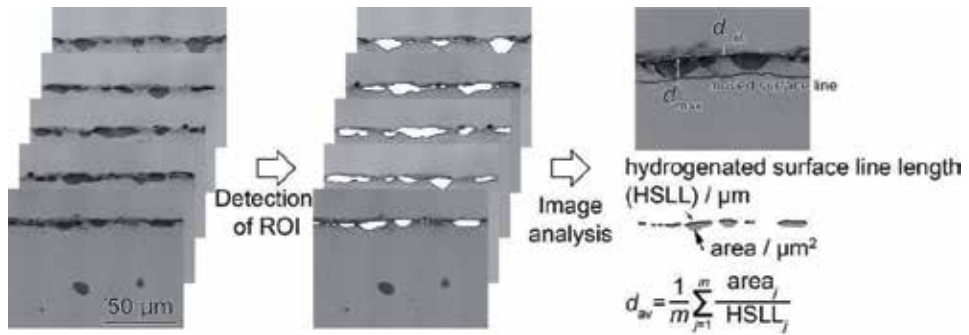


**Figure 1.** Method of quantitative analysis for average ( $d_{av}$ ), maximum ( $d_{max}$ ) and minimum ( $d_{min}$ ) thickness values of  $MgH_2(sur)$  from SEM-BSE images.

### 3. Results

**Figure 2** shows the XRD pattern of hydrogenated Mg, AZ31, AZ61, AZ91 alloys for 1.8 ks. In all the samples, formation of  $MgH_2$  was observed. These samples were not polished, therefore the information from XRD was mainly from  $MgH_2(sur)$ . The peaks from Mg were shifted to higher angle side with Al concentration due to substitutional solid solution formation. On the other hand, in the peak pattern of  $MgH_2$ , obvious peak shifts were not observed with increase of Al concentration.

**Figure 3** shows cross-sectional OM images of annealed and cold rolled AZ61 alloy. The annealed and cold rolled AZ61 exhibited both  $MgH_2(sur)$  (white arrow) and  $MgH_2(int)$  (black arrow). There were no difference on  $MgH_2(sur)$  between annealed and cold rolled AZ61 alloy as  $d_{av}$  was  $9 \mu m$  ( $d_{max}$ :  $22 \mu m$ ,  $d_{min}$ :  $2 \mu m$ ) in annealed and  $d_{av}$  was  $8 \mu m$  ( $d_{max}$ :  $22 \mu m$ ,  $d_{min}$ :  $2 \mu m$ ) in cold rolled condition. However, particle size of  $MgH_2(int)$  was larger in cold rolled condition than in

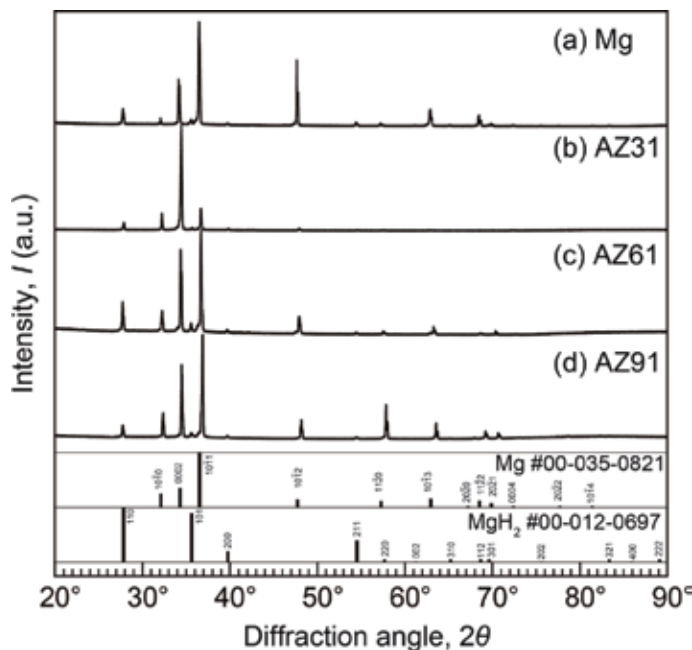


**Figure 2.** XRD profiles of hydrogenated Mg, AZ31, AZ61 and AZ91 alloys at 673 K in 3.61 MPa  $H_2$  for 1.8 ks.



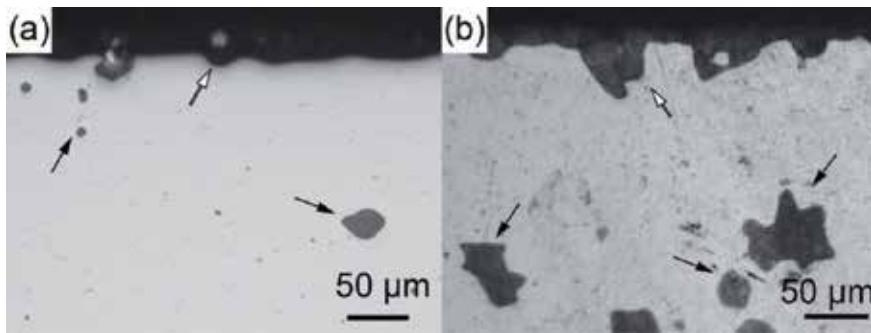


**Figure 3.** Cross-sectional optical micrographs of hydrogenated AZ61 in 3.61 MPa  $H_2$  at 673 K for 129.6 ks (a) annealed and (b) cold-rolled samples. Open and solid arrows point out  $MgH_2(sur)$  and  $MgH_2(int)$ , respectively.

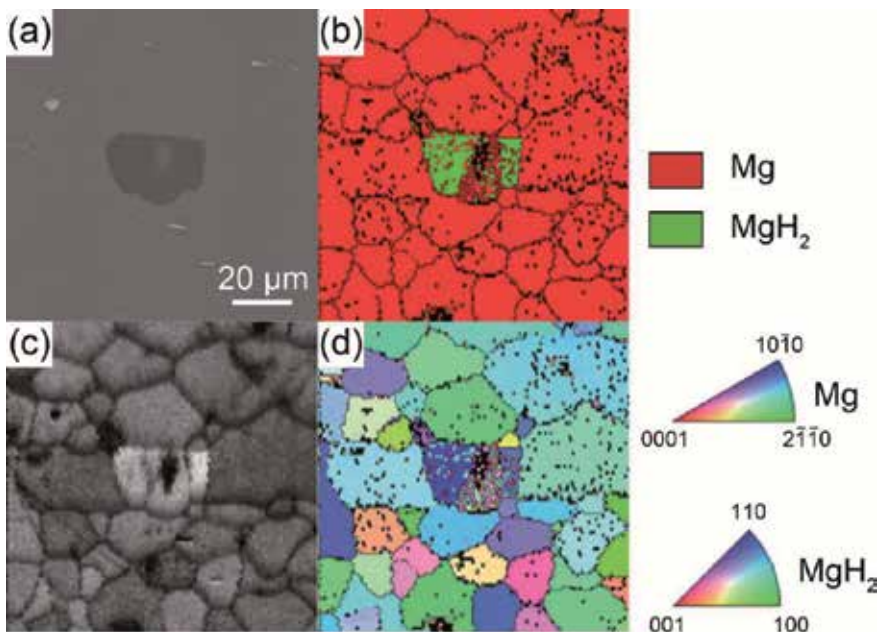


**Figure 4.** SEM-EBSD analyzed images of AZ31 hydrogenated at 673 K in 3.61 MPa  $H_2$  for 64.8 ks. (a) SEM-BSE image, (b) phase map, (c) IQ map, and (d) IPF.

annealed condition as mean diameter was 15  $\mu m$  (maximum: 38  $\mu m$ , minimum: 3  $\mu m$ ) in annealed condition and mean diameter was 53  $\mu m$  (maximum: 125  $\mu m$ , minimum: 14  $\mu m$ ) in cold rolled condition.

**Figure 4** shows the SEM image and results of EBSD analysis of hydrogenated AZ31. **Figure 4** (a) shows the backscattered electron image (BSE), (b) shows the phase map in the same area with (a), (c) is image quality (IQ) map, and (d) is an inverse pole figure (IPF). In phase map (b), Mg was shown in red and  $MgH_2$  was shown in green color. Comparing (a) and (b), dark area in BSE (a) corresponds to  $MgH_2$  area in phase map (b). As focused on IQ map (c), image quality of  $MgH_2$  area was lower than that of Mg area. The decrease of quality at  $MgH_2$  was due to high volume change between Mg to  $MgH_2$  about 32% as the result of residual strain and/or nonconducting material;  $MgH_2$  tends to charge up.

The  $MgH_2(int)$  observed in **Figures 3** and **4** was surrounded with metallic Mg, and the  $MgH_2(int)$  has not interface with hydrogen gas at glance. Therefore,

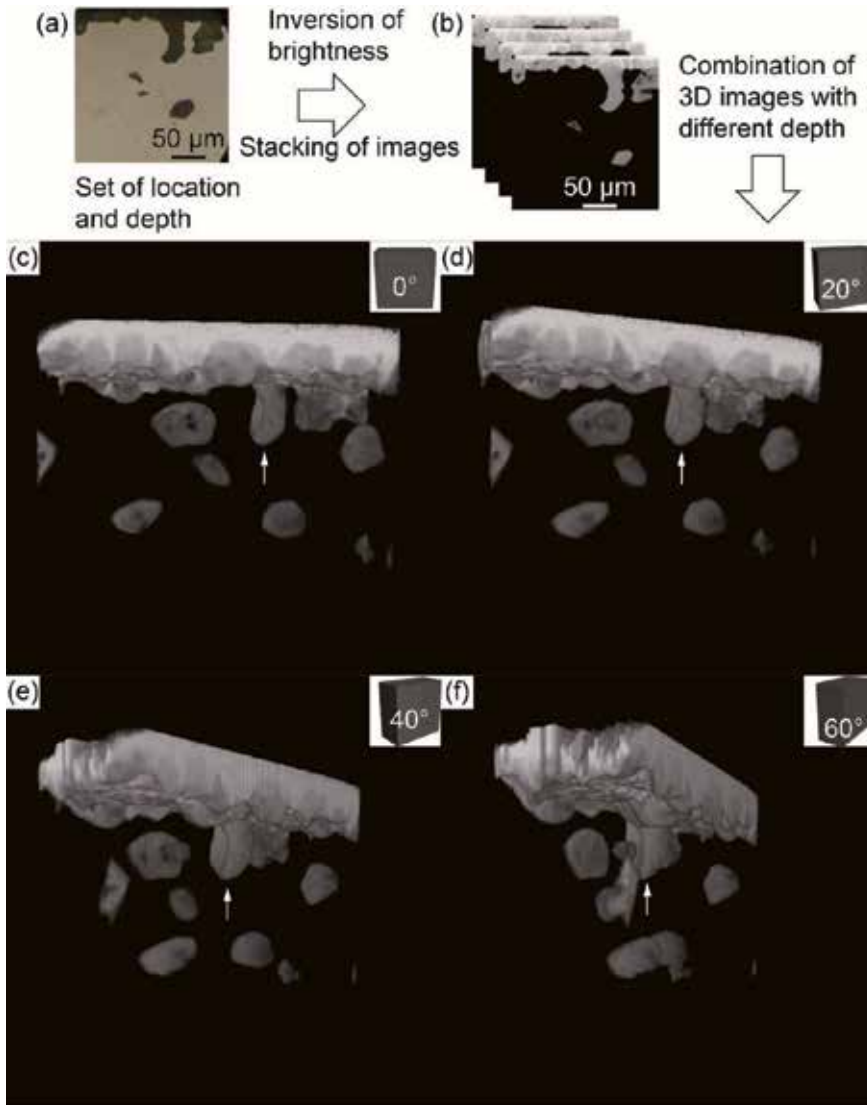


**Figure 5.** Three-dimensional microscopic images obtained from optical micrographs of cold rolled and hydrogenated AZ61 for 129.6 ks (a) a sample of optical micrograph, (b) samples of inverted black and white micrographs, and three-dimensional images (c) 0°, (d) 20°, (e) 40°, and (f) 60°.

three-dimensional analysis was conducted at the area shown in **Figure 5**. **Figure 5** taken from cold rolled and hydrogenated AZ61 sample show (a) part of OM micrograph, (b) MgH<sub>2</sub>(sur) and MgH<sub>2</sub>(int) extracted as ROI area contrast inverted, and construction of three-dimensional image rotated from 0 to 60° ((c) 0°, (d) 20°, (e) 40°, and (f) 60°). From **Figure 5c–f**, the MgH<sub>2</sub>(int) was not in contact with hydrogen gas and MgH<sub>2</sub>(sur).

Focusing on MgH<sub>2</sub>(sur), homogeneous hydride layer does not growth from surface and structure with variations in thickness was spread out in a planar manner with respect to the surface. The white arrow point of MgH<sub>2</sub>(sur) was grown abnormally like as heteroepitaxially, however size of the part of MgH<sub>2</sub>(sur) was same size with surrounding MgH<sub>2</sub>(int), since the part of MgH<sub>2</sub>(sur) would be formed by collision between MgH<sub>2</sub>(sur) and MgH<sub>2</sub>(int) at near surface.

**Figure 6** shows an OM micrograph of hydrogenated Mg and a schematic image. Focusing on  $\text{MgH}_2(\text{int})$ , the shape of  $\text{MgH}_2(\text{int})$  was granular and precipitated on the Mg grain boundary. In addition, two types of  $\text{MgH}_2(\text{int})$  were observed as growth to two adjacent Mg grains (at pointed two grains) and on only one side of Mg grain. They were indicated in the inset image.

**Figure 7** shows the SEM-BSE images of the  $\text{MgH}_2(\text{sur})$  of hydrogenated Mg, AZ31, AZ61, and AZ91 alloys for 1.8–259.2 ks. Focusing on images of hydrogenated in relatively short time, for example at 1.8 ks,  $\text{MgH}_2(\text{sur})$  formed with granular and dotted and that was not formed uniformly like a layer at the time when the entire surface was not covered with hydride. With increase of hydrogenation time, the granular hydride,  $\text{MgH}_2(\text{sur})$ , grew in the direction parallel to the surface and formed a rough layer. For images of samples exposed to relatively long hydrogenation time, the thickness of  $\text{MgH}_2(\text{sur})$  decreased with an increase in Al concentration. **Figure 8** shows the thickness of  $\text{MgH}_2(\text{sur})$  of Mg, AZ31, AZ61, and AZ91

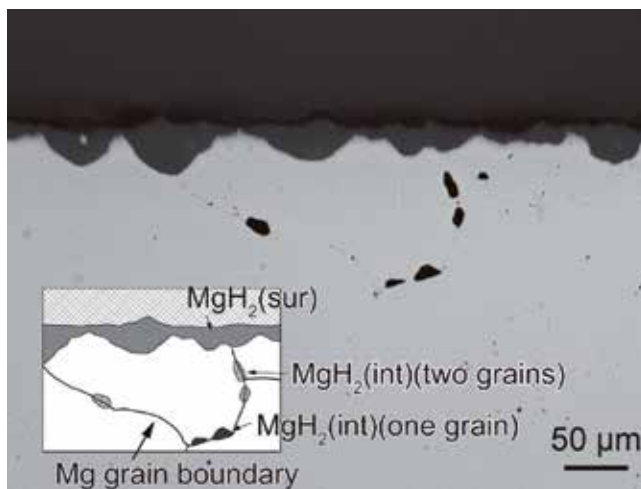


**Figure 6.**  
SEM-BSE image of Mg hydrogenated at 673 K in 3.61 MPa  $\text{H}_2$  for 129.6 ks.

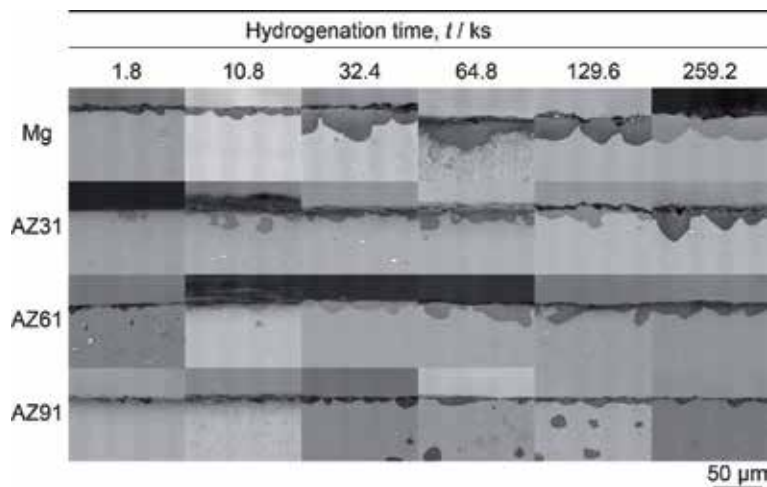


**Figure 7.**  
SEM-BSE images at  $\text{MgH}_2(\text{sur})$  of Mg, AZ31, AZ61 and AZ91 after hydrogenation at 673 K in 3.61 MPa  $\text{H}_2$  for 0–259.2 ks.

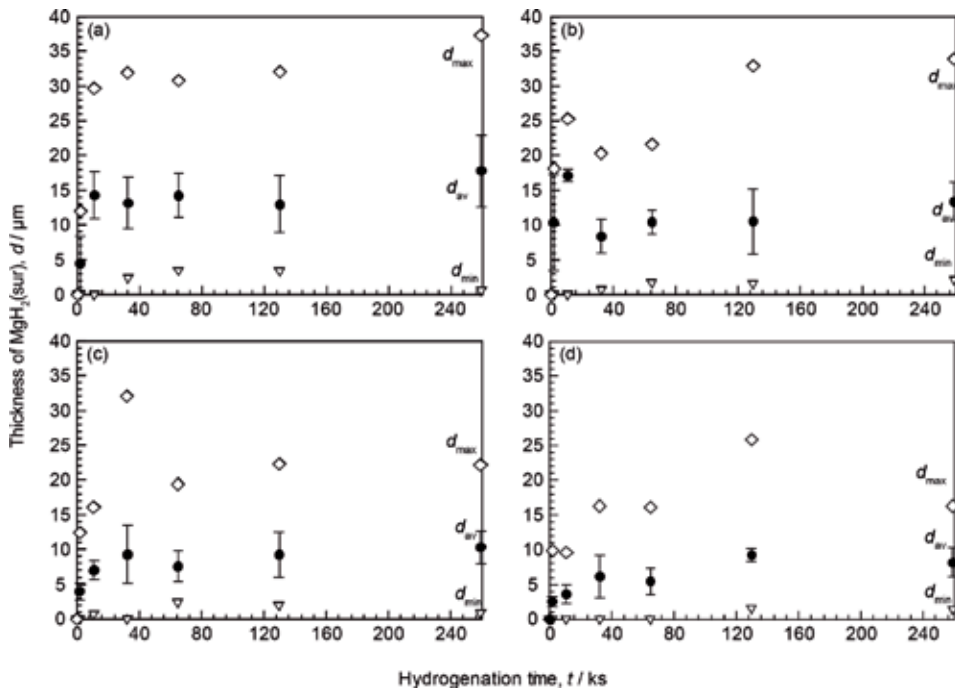


**Figure 8.** Relation between thickness of  $MgH_2(surf)$  and hydrogenation time of (a) Mg, (b) AZ31, (c) AZ61, and (d) AZ91.

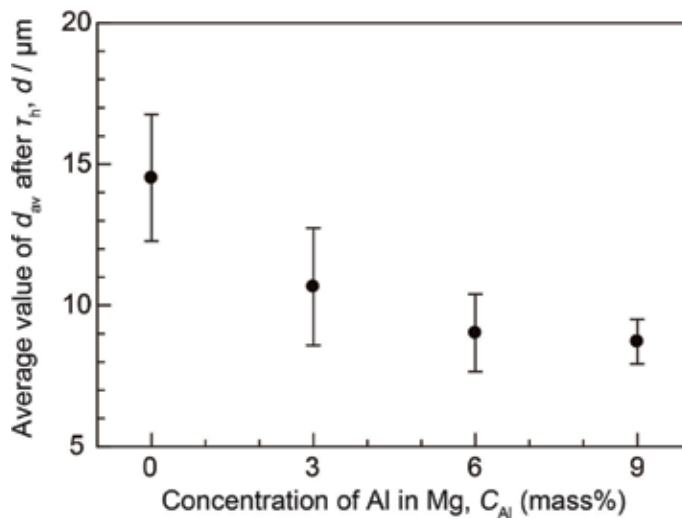


**Figure 9.** Relation between average value of  $d_{av}$  and concentration of Al in Mg after  $\tau_h$ .

alloys with hydrogenation time. The white rhombi and the reverse triangles are shown as  $d_{max}$  and  $d_{min}$ , respectively. The black circles are shown as  $d_{av}$  and the vertical lines are expressed as standard deviation. Focusing on  $d_{min}$ ,  $d_{min} = 0$  means that the surface was not completely covered with  $MgH_2(surf)$ . Therefore, paying attention to the value of  $d_{min}$ , it is possible to estimate the time when entire surface is covered with  $MgH_2(surf)$ , and the time describes as time of halt ( $\tau_h$ ).  $\tau_h$  was 32.4 ks for Mg and AZ31, 64.8 ks for AZ61, 129.6 ks for AZ91, and  $\tau_h$  increased with increasing Al concentration. Next, looking at  $d_{av}$ , it was found that  $d_{av}$  grew greatly

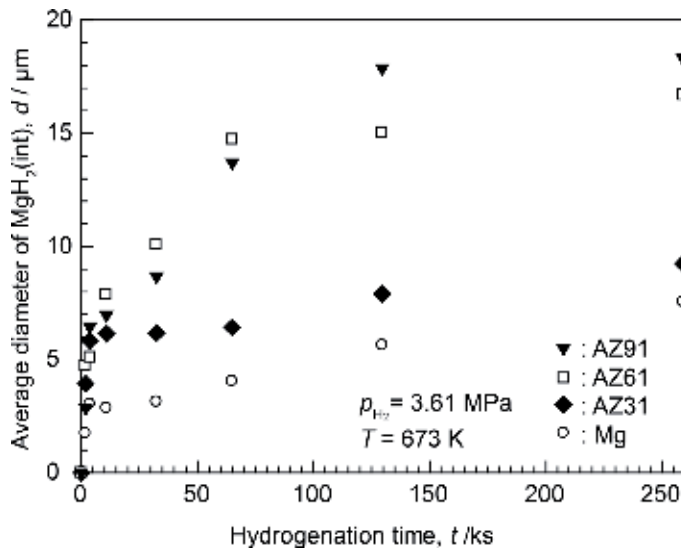


**Figure 10.** Relation between average diameter of  $\text{MgH}_2(\text{int})$  and hydrogenation time of Mg, AZ31, AZ61 and AZ91.

with increasing hydrogenation time before  $\tau_h$ , whereas the growth rate drastically decreased after the time of  $\tau_h$ . These results indicate that the growth of  $\text{MgH}_2(\text{sur})$  halted when sample surface was covered with  $\text{MgH}_2(\text{sur})$ .

To reveal the influence of Al concentration on thickness of  $\text{MgH}_2(\text{sur})$ , the relationship between average of  $d_{\text{av}}$  after  $\tau_h$  and Al concentration is shown in **Figure 9**. As shown in **Figure 9**, it was found that the thickness of  $\text{MgH}_2(\text{sur})$  decreased with the increase of Al concentration, and the decrease ratio is remarkable from 0 to 3 mass% Al than from 6 to 9 mass% Al.

Changes in the growth rate of  $\text{MgH}_2(\text{int})$  are described as follows. **Figure 10** shows the average particle size of  $\text{MgH}_2(\text{int})$  of Mg, AZ31, AZ61, and AZ91 alloys with hydrogenation time. As with the changes of  $\text{MgH}_2(\text{sur})$ , the growth rate of  $\text{MgH}_2(\text{int})$  was high over short time and low on longer hydrogenation time side. The time of infection point was almost correlated with  $\tau_h$  as 3.6 ks for Mg and AZ31, 64.8 ks for AZ61, 129.6 ks for AZ91. **Figure 10** shows the relationship between the average particle size of  $\text{MgH}_2(\text{int})$  after  $\tau_h$  and Al concentration. The average particle size of  $\text{MgH}_2(\text{int})$  increased with increase of Al concentration, contrary to the change of thickness of  $\text{MgH}_2(\text{sur})$ .

## 4. Discussion

### 4.1 Formation of $\text{MgH}_2$ in Mg core

After hydrogenating Mg and AZ alloys, two types of  $\text{MgH}_2$  were formed: on the surface,  $\text{MgH}_2(\text{sur})$  and in the unreacted Mg core,  $\text{MgH}_2(\text{int})$ .  $\text{MgH}_2(\text{int})$  formed only along Mg grain boundary, and did not form in Mg crystal grain. It is known that the diffusion of H atoms in Mg made the grain boundary a preferential route [20]. Therefore, the reason why  $\text{MgH}_2(\text{int})$  preferentially formed on grain boundary would be one factor of the fast diffusion of H atoms at Mg grain boundary. In addition,  $\text{MgH}_2$  preferentially formed with existence of defect as nanocrystallize Mg showed fast hydrogenation and dehydrogenation [3]. This observation also supports the reason why  $\text{MgH}_2(\text{int})$  formed on Mg grain boundary.

As shown in **Figure 6**,  $\text{MgH}_2(\text{int})$  grew for adjacent Mg crystal grain or only on one crystal grain. In addition, some Mg grain boundaries did not form  $\text{MgH}_2(\text{int})$ . Some orientation relationship between Mg and  $\text{MgH}_2$  was reported as  $(0001)_{\text{Mg}}// (001)_{\text{MgH}_2}$ ,  $[-1-120]_{\text{Mg}}//[001]_{\text{MgH}_2}$  [21] and  $(-2110)_{\text{Mg}}// (12-1)_{\text{MgH}_2}$ ,  $[0001]_{\text{Mg}}// [101]_{\text{MgH}_2}$  [22]. Because interface energy between new phase and mother phase was low in orientation relationship, solid-solid transformation easily proceeded in orientation relationship with a small lattice mismatch. On the other hand, hydrogenation rate of Mg increased with formation of (0002) crystal texture [23, 24]. From above results, nucleation and growth of  $\text{MgH}_2(\text{int})$  would also depend on adjacent Mg crystal orientation. However, influence of Mg crystal texture for  $\text{MgH}_2$  formation had other formation of MgO factor [24], and particle shape of  $\text{MgH}_2(\text{int})$  was ellipsoidal. Therefore, consideration with complex effects for formation of  $\text{MgH}_2(\text{int})$  should be needed such as orientation relationship, precipitates on Mg grain boundary, interface energy with adjacent Mg grains, and flux of H atom and so on.

#### 4.2 Relationships between particle size of $\text{MgH}_2(\text{int})$ and Al concentration

Before  $\tau_h$ ,  $\text{MgH}_2(\text{sur})$  formed in granular form and spread and the growth rate of average thickness was larger than that after  $\tau_h$ . After  $\tau_h$ , the growth of  $\text{MgH}_2(\text{sur})$  apparently halted. These growth rate change was same in  $\text{MgH}_2(\text{int})$ . These results be attributed to extremely low diffusion rate of H in  $\text{MgH}_2$  when compared to that in Mg [12, 13]. When the whole surface was covered with  $\text{MgH}_2(\text{sur})$ , the supply rate of H to unreacted internal metallic Mg or AZ significantly decreased, halting the growth of  $\text{MgH}_2(\text{sur})$  and  $\text{MgH}_2(\text{int})$ .

Some studies have reported that the amount of  $\text{MgH}_2$  formed depends on Gibbs free energy ( $\Delta_r G$ ) of  $\text{MgH}_2$  from Mg and  $\text{H}_2$  gas [16, 25, 26]. The microstructure of  $\text{MgH}_2(\text{sur})$  at initial state was formed as granular and scattered. Concerning this result, the nucleation rate of  $\text{MgH}_2(\text{sur})$  was low and the nucleation rate would depend on absolute value of  $\Delta_r G$ . Applying low value of  $\Delta_r G$ , growth of  $\text{MgH}_2(\text{int})$  proceeded because nucleation rate of  $\text{MgH}_2(\text{sur})$  was low and  $\tau_h$  is shift to longer time. However, when high value of  $\Delta_r G$  was applied, the nucleation rate of  $\text{MgH}_2(\text{sur})$  increased and immediately the surface covered with thin  $\text{MgH}_2(\text{sur})$  rapidly and the particle size of  $\text{MgH}_2(\text{int})$  was explained to be small size.

The average particle size of  $\text{MgH}_2(\text{int})$  increased with increasing Al concentration. As shown in **Figure 10**, the growth rate of  $\text{MgH}_2(\text{int})$  decreased when the surface was covered with  $\text{MgH}_2(\text{sur})$ . The thickness of  $\text{MgH}_2(\text{sur})$  decreased with increasing Al concentration. From these results, the reasons why the particle size of  $\text{MgH}_2(\text{int})$  decreased with increasing Al concentration would be shifting of long time  $\tau_h$  and small diffusion distance of H in  $\text{MgH}_2$  at high Al content. Therefore, the amount of supplying H increased and large size of  $\text{MgH}_2(\text{int})$  formed with increasing Al concentration.

## 5. Conclusion

In this study, focusing on the formation of  $\text{MgH}_2$  in the Mg core, the effects of Al concentration in Mg for microstructure of hydrogenated Mg and Mg-Al-Zn alloys were investigated.  $\text{MgH}_2(\text{int})$  formed at Mg grain boundary and the growth rate of  $\text{MgH}_2(\text{int})$  was investigated including plastic deformed condition. From three-dimensional analysis, it was found that the  $\text{MgH}_2(\text{int})$  was surrounded by metallic Mg or Mg-Al-Zn alloys and they had not interfaced with  $\text{H}_2$  gas and  $\text{MgH}_2$  on the surface area ( $\text{sur}$ ). The time when the surface covered with  $\text{MgH}_2(\text{sur})$  was described as time of halt,  $\tau_h$ . Comparing growth rate of  $\text{MgH}_2(\text{sur})$  and  $\text{MgH}_2(\text{int})$

before and after  $\tau_h$ , the growth rate of both  $\text{MgH}_2$  were higher before  $\tau_h$  than after  $\tau_h$ . The growth of  $\text{MgH}_2(\text{sur})$  and  $\text{MgH}_2(\text{int})$  were observed to stop after  $\tau_h$  because H supply route change from in Mg to  $\text{MgH}_2$ . After  $\tau_h$ , the thickness of  $\text{MgH}_2(\text{sur})$  decreased and particle size of  $\text{MgH}_2(\text{int})$  increased with increasing Al concentration. This result could be explained by increase of supplied H amount to  $\text{MgH}_2(\text{int})$  due to the shifting  $\tau_h$  to longer time and small diffusion distance of  $\text{MgH}_2(\text{sur})$  which had low value of diffusion coefficient.

Findings from this research point out in following:

- Hydrogenated Mg plate formed  $\text{MgH}_2$  on surface(sur) and in internal area(int).
- The thickness of  $\text{MgH}_2(\text{sur})$  decreased with increase of Al concentrations in Mg.
- The particle size of  $\text{MgH}_2(\text{int})$  increased with increase of Al concentrations in Mg.

## Acknowledgements


This is a product of research which was financially supported by JSPS KAKENHI Grant Number 19K15278, and the Environment Research and Technology Development Fund (2RF-1801) of the Environmental Restoration and Conservation Agency of Japan.

## Author details

Ryota Kondo\* and Takeshita T. Hiroyuki  
Department of Chemistry and Materials Engineering, Faculty of Chemistry,  
Materials and Bioengineering, Kansai University Suita, Osaka, Japan

\*Address all correspondence to: [rkondo@kansai-u.ac.jp](mailto:rkondo@kansai-u.ac.jp)

## IntechOpen

© 2019 The Author(s). Licensee IntechOpen. This chapter is distributed under the terms of the Creative Commons Attribution License (<http://creativecommons.org/licenses/by/3.0>), which permits unrestricted use, distribution, and reproduction in any medium, provided the original work is properly cited. 

## References

- [1] Jehan M, Fruchart D. McPhy-Energy's proposal for solid state hydrogen storage materials and systems. *Journal of Alloys and Compounds*. 2013;**580**:S343-S348
- [2] Schlapbach L, Züttel A. Hydrogen-storage materials for mobile applications. *Nature*. 2001;**414**:353-358
- [3] Zaluska A, Zaluski L, Ström-Olsen JO. Nanocrystalline magnesium for hydrogen storage. *Journal of Alloys and Compounds*. 1999;**288**:217-225
- [4] Varin RA, Czujko T, Chiu C, Wronski Z. Particle size effects on the desorption properties of nanostructured magnesium dihydride (MgH<sub>2</sub>) synthesized by controlled reactive mechanical milling (CRMM). *Journal of Alloys and Compounds*. 2006;**424**:356-364
- [5] Oelerich W, Klassen T, Bormann R. Hydrogen sorption of nanocrystalline Mg at reduced temperatures by metal-oxide catalysts. *Advanced Engineering Materials*. 2001;**3**:487-490
- [6] Barkhordarian G, Klassen T, Bormann R. Fast hydrogen sorption kinetics of nanocrystalline Mg using Nb<sub>2</sub>O<sub>5</sub> as catalyst. *Scripta Materialia*. 2003;**49**:213-217
- [7] Shibata K, Tanaka K, Kurumatani K, Nishida Y, Kondo R, Takeshita HT. Formation of MgCu<sub>2</sub> from MgH<sub>2</sub> and Cu in pressurized hydrogen atmosphere. *Materials Transactions*. 2015;**56**:785-789
- [8] Tanaka K, Takeshita HT, Kurumatani K, Miyamura H, Kikuchi S. The effect of initial structures of Mg/Cu super-laminates on hydrogen absorption/desorption properties. *Journal of Alloys and Compounds*. 2013;**580**:S222-S225
- [9] Tanaka K, Takeshita HT, Shin H, Kurumatani K, Kiyobayashi T, Takeichi N, et al. Micro/nano-structural transition and hydrogen absorption mechanism in Mg/Cu super-laminate composites. *Materials Transactions*. 2014;**55**:1122-1128
- [10] Tanaka K, Shibata K, Kurumatani K, Ikeuchi S, Kikuchi S, Kondo R, et al. Formation mechanism of micro/nano-structures through competitive reactions in Mg/Cu super-laminate composites during initial hydrogenation. *Journal of Alloys and Compounds*. 2015;**645**:S72-S75
- [11] Noritake T, Towata S, Aoki M, Seno Y, Hirose Y, Nishibori E, et al. Charge density measurement in MgH<sub>2</sub> by synchrotron X-ray diffraction. *Journal of Alloys and Compounds*. 2003;**356-357**:84-86
- [12] Uchida HT, Wagner S, Hamm M, Kürschner J, Kirchheim R, Hjärvarsson B, et al. Absorption kinetics and hydride formation in magnesium films: Effect of driving force revisited. *Acta Materialia*. 2015;**85**:279-289
- [13] Yang B, He Y-P, Zhao Y-P. Hydrogenation of magnesium nanoblades: The effect of concentration dependent hydrogen diffusion. *Applied Physics Letters*. 2011;**98**:081905
- [14] Shrinivasan S, Tien H-Y, Tanniru M, Ebrahimi F, Tatiparti SSV. Transition from interfacial to diffusional growth during hydrogenation of Mg. *Materials Letters*. 2015;**161**:271-274
- [15] Friedlmeier G, Groll M. Experimental analysis and modelling of the hydriding kinetics of Ni-doped and pure Mg. *Journal of Alloys and Compounds*. 1997;**253-254**:550-555
- [16] Tien H-Y, Tanniru M, Wu C-Y, Ebrahimi F. Effect of hydride nucleation rate on the hydrogen capacity of Mg. *International Journal of Hydrogen Energy*. 2009;**34**:6343-6349



- [17] Ueda TT, Tsukahara M, Kamiya Y, Kikuchi S. Preparation and hydrogen storage properties of Mg–Ni–Mg<sub>2</sub>Ni laminate composites. *Journal of Alloys and Compounds*. 2005;**386**:253-257
- [18] Abràmoff MD, Magalhães PJ, Ram SJ. Image processing with ImageJ. *Biophotonics International*. 2004;**11**:36-42
- [19] Schneider CA, Rasband WS, Eliceiri KW. NIH Image to ImageJ: 25 years of image analysis. *Nature Methods*. 2012;**9**:671-675
- [20] Uchida HT, Kirchheim R, Pundt A. Influence of hydrogen loading conditions on the blocking effect of nanocrystalline Mg films. *Scripta Materialia*. 2011;**64**:935-937
- [21] Schober T. The magnesium-hydrogen system: Transmission electron microscopy. *Metallurgical Transactions A*. 1981;**12**:951-957
- [22] Nogita K, Tran XQ, Yamamoto T, Tanaka E, McDonald SD, Gourlay CM, et al. Evidence of the hydrogen release mechanism in bulk MgH<sub>2</sub>. *Scientific Reports*. 2015;**5**:8450
- [23] Jorge AM Jr, Prokofiev E, Ferreira de Lima G, Rauch E, Veron M, Botta WJ, et al. An investigation of hydrogen storage in a magnesium-based alloy processed by equal-channel angular pressing. *International Journal of Hydrogen Energy*. 2013;**38**:8306-8312
- [24] Jorge AM, de Lima GF, Triques MRM, Botta WJ, Kiminami CS, Nogueira RP, et al. Correlation between hydrogen storage properties and textures induced in magnesium through ECAP and cold rolling. *International Journal of Hydrogen Energy*. 2014;**39**:3810-3821
- [25] Mooij L, Dam B. Nucleation and growth mechanisms of nano magnesium hydride from the hydrogen sorption kinetics. *Physical Chemistry Chemical Physics*. 2013;**15**:11501-11510
- [26] Mooij L, Dam B. Hysteresis and the role of nucleation and growth in the hydrogenation of Mg nanolayers. *Physical Chemistry Chemical Physics*. 2013;**15**:2782-2792

*Edited by Manoj Gupta*

Magnesium-based materials are rapidly emerging in recent years to primarily assist in mitigating global warming and for health benefits. They are seen as materials of the future due to their lightweight, nutritional characteristics and abundance on Earth. Their applications are in a wide array of engineering and biomedical sectors, promising a multi-billion-dollar market in the very near future. The applicability of magnesium-based materials also suits the current emphasis on sustainability and a greener earth. This book was thus conceptualized and highlights important areas of current research and future directions including fundamental and applied principles related to primary and secondary processing types, microstructural evolution, machining, joining, and the past and current application scenario of magnesium-based materials.

Published in London, UK

© 2020 IntechOpen  
© Anna Usova / iStock

**IntechOpen**

